Dynamics of small repetitive eruptions at Stromboli volcano as inferred from seismic and acoustic analyses

博士論文

Dynamics of small repetitive eruptions at Stromboli volcano as inferred from seismic and acoustic analyses

（地震・空振の解析から推定されるストロンボリ火山の小規模繰り返し噴火のダイナミクス）

杉村 俊輔

令和元年

Doctoral thesis

Dynamics of small repetitive eruptions at Stromboli volcano as inferred from seismic and acoustic analyses

（地震・空振の解析から推定されるストロンボリ火山の小規模繰り返し噴火のダイナミクス）

Shunsuke Sugimura
（杉村　俊輔）

Department of Geophysics
Graduate School of Science
Tohoku University

Thesis Commit Members

Professor Takeshi Nishimura (Chair, Supervisor)
Professor Toru Matsuzawa
Professor Maurizio Ripepe (University of Florence)
Associate Professor Tomofumi Kozono
Associate Professor Emanuele Marchetti (University of Florence)
Assistant Professor Giorgio Lacanna (University of Florence)

2019

Acknowledgement

Foremost, I would like to express my gratitude to my advisor Prof. Takeshi Nishimura for the continuous guidance and advices throughout my Ph.D study. I could not accomplish the present study without his support and encouragement. I am very thankful for his patience, motivation, and enthusiasm. I also would like to express my sincere appreciation to Prof. Maurizio Ripepe for his continuous support and valuable advices. I could not conduct my study in Florence for one year without his help.

I am very thankful to Prof. Toru Matsuzawa for his invaluable comments on this study. I would like to thank Associate Prof. Hisashi Nakahara, Associate Prof. Tomofumi Kozono, Assistant Prof. Kentaro Emoto, and Assistant Prof. Masayuki Kano, for their valuable advices on my study and for their help. My sincere thanks also go to Associate Prof. Emanuele Marchetti, Assistant Prof. Giorgio Lacanna for their useful discussions in Florence, and for their invaluable comments on this study. Also, I express my gratitude to all members in University of Florence for their variable advice to develop my study and their help related to my stay in Florence for one year. I would like to especially thank Dr. Denis Legrand and Dr. Sébastien Valade for providing the observation data. The main part of this thesis is based on the analyses of these valuable data. I also would like to appreciate Associate Prof. Hiroshi Aoyama, Dr. Eisuke Fujita, Dr. Takahiro Miwa, Dr. Ryohei Kawaguchi, and Dr. Taishi Yamada for their cooperation on the temporary observation at Stromboli volcano in June 2015, and their valuable advices and discussions on my study.

I express my gratitude to all the professors of the Research Center for Prediction of Earthquakes and Volcanic Eruptions for their comments and discussions in the weekly seminar. Many thanks to all members of Solid Earth Physics Laboratory and the Research Center for Prediction of Earthquakes and Volcanic Eruptions. I spent precious time with them. I am also grateful to Ms. Chika Kamada and Ms. Naoko Mizuta for all their help.

I am very thankful to the International Joint Graduate Program in Earth and Environmental Sciences (GP-EES) in Tohoku University. This work and my stay in Florence were supported by this international program. I would like to thank Ms. Shinobu Okuyama, and Assistant Prof. Shin Ozawa for their continuous supports. I am also grateful to the Consortium for Human Resource Development in Volcanology for giving opportunities of field study and volcanology seminars.

For numerical simulations of waveform propagation, we used computer resources of the Earthquake Information Center system of the Earthquake Research Institute at the University of

Tokyo.

Finally, I would like to express my deep and sincere gratitude to my family for their continuous supports and encouragements.

Abstract

Seismic and acoustic waves associated with Strombolian or Vulcanian eruptions, which repeatedly occur at several volcanoes, often show common characteristics on the dynamics of explosions. The analyses of these data are fundamental and important for understanding volcanic eruptions. The dynamics of explosions at Stromboli volcano, which is a representative volcano of Strombolian eruption and one of the most active volcanoes around the world, have been investigated by geophysical observation data. Seismic analyses (moment tensor inversion, particle motions, and initial motions) revealed source locations and source mechanisms of earthquakes associated with summit explosions. Especially very-long-period (VLP) earthquakes with a dominant period of about 10 s are intensively studied because such long-period waves include a lot of source information. Acoustic signals excited with explosions and puffing of gas bubble bursts on the magma surface are analyzed to identify eruptive craters and estimate the eruptive energy. These seismic and acoustic data analyses have been conducted, but detailed examination of the accuracies of source locations or mechanisms are not well studied, which are necessary to discuss the details of magma/gas motions in a small scale from a few hundred meters depths to the craters before and during explosions. The objectives of this study are, therefore, to correctly determine the source locations and mechanisms of eruption earthquakes that are generated at the time of summit explosions (so called Strombolian eruption), and to clarify underground magma/gas motions before and during explosions. We analyze seismic and acoustic data recorded at stations that are very close to the craters with a good coverage and apply several methods for determining source locations and mechanisms.

In Chapter 1, we first summarize previous studies on seismic and acoustic data analyses associated with volcanic explosions at active volcanoes. Subsequently, we present previously obtained results on Stromboli volcano which are based on geophysical observations, laboratory experiments, and numerical simulations. Here, we point out a discrepancy in quantifying magma/gas motions between observations and experiments/simulations. Then, we present the objectives of this study.

In Chapter 2, we introduce a temporary seismic and acoustic observation conducted for the period from 24 to 28 September 2016. The University of Florence deployed four seismo-acoustic stations and one seismic station at Stromboli volcano. These stations were set at only 100-300 m away from the main craters. Also, the stations azimuthally surrounded the craters as much as possible. The data

recorded at such a very-near-field observation network show clear VLP (2-20 s, 0.05-0.5 Hz) seismic signals whose onset is about 5 s before the occurrence of an explosion. Seismic signals above 1 Hz and acoustic signals (0.1-20 Hz) associated with bubble bursts are also observed with high signal-to-noise ratios. Characteristics of these seismic and acoustic signals are summarized.

In Chapter 3, we estimate source locations and mechanisms of eruption earthquakes based on a moment tensor inversion method in which topographic effects and tilt motions on seismic waves are taken into account. We analyze the seismic data at 0.05-0.2 Hz, 0.2-0.5 Hz, and 0.5-1.0 Hz. The source locations of seismic signals at the lower frequency part of the VLP band (0.05-0.2 Hz) are located at about 200 m away from the eruptive crater at 600 m or 650 m a.s.l. (depths of 170 m or 120 m). The VLP waveforms of the events located at these two source clusters show slightly different spatial distributions of amplitudes after the onset of acoustic waves. The difference in the source locations may indicate the difference in the source mechanisms during the explosions. Most of the source locations of seismic signals at the higher frequency part of the VLP band (0.2-0.5 Hz) are located at the region of 100 m east of the seismic sources at 0.05-0.2 Hz with an elevation of 600 m a.s.l. (a depth of 170 m). Most of the source locations of long-period (LP) seismic signals at 0.5-1.0 Hz are located almost below the eruptive crater at 700 m a.s.l. (a depth of 70 m). The source mechanisms of the VLP and LP signals are dominated by the diagonal moment tensor components, which suggest volumetric changes at the source regions. The model resolution matrices show that the source mechanisms may not be well resolved. We are not able to discuss the source mechanisms more in detail from analyses of the very-near-field observation data. We further examine the utility and issues of the very-near-field network for estimating the source locations and mechanisms by conducting inversion for synthetic data consisting of a different network configuration and finite source modelling. The results show that the very-near-field network contributes to exactly determine the source locations compared with a distant seismic network with a large number of seismic stations. Synthetic tests using finite source modelling show that the source locations are well recovered but it is difficult to constrain the source mechanisms from the very-near-field observation data.

In Chapter 4, we determine the source locations of the VLP signals at 0.05-0.2 Hz by applying a master event method with a deconvolution technique. We investigate how the repetitive earthquakes are distributed around a master event, which is determined by the moment tensor inversion, based on changes in waveform correlation and source time function. The deconvolution technique enables us to correctly measure the arrival time difference between two seismic events. The relative VLP

sources are located around the master event within about 50 m in horizontal and about 80 m in vertical directions. About 80 % of the relative source locations for all the events are determined with an error of less than ± 25 m.

In Chapter 5, we estimate the explosion source depth which represents the surface level of magma in the reservoir or conduit, and the propagation velocity of magma/gas in the conduit by measuring the arrival times of seismic and acoustic signals. By applying an automatically picking method and using the data recorded at the very-near-field network, the onsets of seismic and acoustic signals are systematically measured. As a result, the explosion source depth is estimated to be 72.9 m in average. The propagation velocity of magma/gas, which is derived from the occurrence times and depths of the VLP source (120-170 m) to the explosion source (73 m), is estimated to be 14.4-30.6 m/s. This velocity is much faster than the theoretical values predicted from a gas slug ascent model in a vertical conduit. Since such high-speed magma/gas motions are estimated from analyses of the data at a different station, a gas slug ascent model that has been often used to explain Strombolian eruptions may be necessary to be modified or reconstructed.

In Chapter 6, we firstly analyze the data at a different observations period (in June 2015) to compare the results of source locations and conduit parameters obtained from the September 2016 data. The explosion source depths estimated from the 2015 data are almost same as those estimated from the 2016 data. The result of the relative hypocenter determination shows that the source locations of VLP (0.2-0.5 Hz) signals systematically distribute below two main craters. Subsequently, on the basis of the results obtained from 2015 and 2016 observation data and analyses of a preceding VLP (0.05-0.2 Hz) seismic phase detected 10-20 s before the onset of explosions, we discuss the dynamics of Strombolian eruptions. The eastward migration of the VLP source toward an explosion and westward migration during the explosion are indicated. We infer that these migrations are caused by pressure disturbances associated with a fluid flow and/or pressure waves in the top of the magma reservoir, a reaction force and withdrawal of magma by the explosion, and/or a recovery process of magma in the shallow magma reservoir.

In this thesis, we have investigated the source locations and mechanisms of eruption earthquakes to understand the dynamics of volcanic explosions. Our results highlight usefulness and importance of very-near-field observations at active volcanoes for not only determining the source locations but also detecting temporal changes in the seismic sources before, during and after the explosions. Detailed data analyses of such very-near-field observation enabled us to newly capture lateral

magma/gas motions in the magma reservoir that occur for several tens of seconds before and during the explosions at Stromboli volcano.

Contents

Chapter 1

Introduction

1.1 Seismic and acoustic analyses of volcanic eruptions at active volcanoes

Seismic signals are often observed when volcanic eruptions occur. Seismic waves associated with eruptions are generated by motions of volcanic fluid such as magma and gas in the conduit and/or chamber. Hence, spaito-temporal changes of their hypocenters and generation processes enable us to understand the dynamics of eruptions.

Source locations and mechanisms of eruption earthquakes, which are the earthquakes associated with Vulcanian or Strombolian eruptions, have long been investigated by seismic waveform analyses such as initial motions, amplitudes, comparison between observed and synthetic waveforms. For example, the explosion earthquakes at Sakurajima volcano in Japan are located at depths of 1-3 km beneath the summit crater by hypocenter determination using P-wave arrival times (Kamo, 1978; Ishihara, 1990; Iguchi, 1994). The hypocentral zone is considered to present a cylindrical conduit. Ishihara (1985) investigated the time sequence of the explosion earthquake and surface phenomena such as visible shock waves, eruption cloud and volcanic blocks accompanying an explosive eruption at Sakurajima volcano. Time lag between the origin time of explosion earthquake and that of the shock waves at the crater bottom indicates that the triggering of explosion earthquakes located at depths of 1-3 km clearly precedes the explosion at the crater bottom. Tameguri et al. (2002) further investigated the initial motion of explosion earthquakes at Sakurajima volcano. They have revealed that the explosion earthquake at Sakurajima volcano is initiated by an isotropic expansion followed by a cylindrical contraction at a depth of 2 km from the crater, and instantaneous volume increase of the gas pocket followed by contraction at 0.25-0.5 km depth just beneath the crater which generates the air-shock. The migration velocity estimated from the time difference between the initial expansion and the air shock generation is 1.4-1.9 km/s. Since the velocity is so high, the pressure wave generated at the depths propagates in the conduit to cause the explosion. Kumagai et al. (2011) applied a source location method using high frequency (5-10 Hz) seismic amplitudes to an explosion event of February 11, 2010 at Tungurahua volcano, Ecuador. The result indicates that the seismic waves were triggered at a depth of 6 km below the summit, and

the seismic source ascended toward the summit with a speed of about 1600 m/s which was estimated by the locations in three different time periods. Ascending of seismic source observed before an eruption is similar to the source migration at Sakurajima presented in Tameguri et al. (2002). Such amplitude source location method has been applied to analyze volcanic explosion events (Zobin et al., 2015; Arámbula-Mendoza et al., 2018).

The accurate hypocenter determination is very important to correctly interpret the parameters such as the speeds of the ascending sources that are interpreted to be caused by pressure waves travelling in magma (Tameguri et al., 2002; Kumagai et al., 2011). Such speeds of pressure waves depend on physical properties of the magma in the conduit such as viscosity, vesicularity, and temperature (e.g., Kieffer, 1977; Chouet, 1986), which are indispensable to understand magma dynamics from geophysical as well as geochemical or petrological approaches. Hypocenter determination using P-wave arrivals is a simple method, but P- or S-waves of explosion earthquakes often have unclear onsets, which may disable us to exactly determine their hypocenters (Ferrucci, 1995; Zobin, 2012). The amplitude source location method is a simple method effective to the events in which arrival times of P- or S-waves are difficult or impossible to measure. This method assumes an isotropic radiation but the correction of radiation patterns depending on focal mechanisms should be considered. In addition, some parameters such as amplitude (absolute, root-mean-square, or median), wave property (P-wave, S-wave, or surface wave), and quality factor of attenuation are also needed, and these greatly change the accuracy of determination (Kumagai et al., 2010; Taisne et al., 2011).

From 1990s, the development of broadband seismic observation/monitoring systems enables us to analyze seismic signals with various frequency bands (e.g., Chouet and Matoza, 2013). Long-period (LP, 0.2-2 s) and very-long-period (VLP, 2-100 s) seismic signals have been observed associated with volcanic explosions. Especially, VLP and LP seismic signals have been observed several to several tens of seconds before and/or during the Vulcanian or Strombolian eruptions (e.g., Rowe et al., 1998; Ripepe et al., 2001; Tameguri et al., 2002; Iguchi et al., 2008; Aster et al., 2008; Zobin et al., 2009). These waves are useful for understanding the magma motions in the conduit just before or during the eruptions. Since these signals have very long wavelengths in the range of tens to hundreds of kilometers, analysis of these signals suffers little path distortion and little inaccuracy of velocity structures. This facilitates the analysis of LP and VLP signals. For example, Rowe et al. (1998) analyzed very-long-period seismic signals associated with Strombolian explosions at Mount Erebus volcano, Ross Island, Antarctica. Explosions at the summit lava lake

occur and associated high-frequency (1-6 Hz) signals begin ~1.5 s after the VLP onset. Particle motions of VLP seismic signals suggest that an initial depth of the VLP source is 0.3 to 0.8 km below the summit, and the VLP source migrates deeper (1 to 1.5 km below the summit) in the course of ~15 s. The authors interpret these VLP oscillations observed following Strombolian explosions as a nondestructive lossy resonance or nonlinear fluid-flow excitation within the shallow magmatic system. In the last decades, moment tensor inversion of VLP earthquakes associated with Strombolian or Vulcanian eruptions has been widely applied to estimate the optimal source location and mechanism. This method solves time histories of the amplitudes of moment tensor or single force components at the source. The volumetric change in the volcanic edifice or spatio-temporal change of forces at the source have been interpreted based on the estimated source time functions. Moment tensor solutions have given us images of the magma chambers underground such as sill/dike cracks (Ohminato et al., 1998; Chouet et al., 2003, 2008; Waite et al., 2008; Lyons and Waite, 2011; Haney et al., 2012), ellipsoidal cavity (Kim et al., 2014), or expansion/contraction of a gas pocket in the conduit (Tameguri et al., 2002; Yamada et al., 2016). The vertical single force component has often been interpreted as a reaction force by ejection of magma or gas (Nishimura and Hamaguchi, 1993; Ohminato et al., 2006; Kim et al., 2014). However, the single force components that are solved at the same time as the moment tensor are sometimes interpreted as spurious ones due to a mislocated source location, mismodeling of velocity structures, or low signal-to-noise ratio of signals (Davi et al., 2010; De Barros et al., 2013; Lanza and Waite, 2018). These inversion results are usually evaluated by a grid search that selects where waveform residual or Akaike Information Criterion (AIC) value, which is to estimate how well the solution is resolved depending on the number of free model parameters, are minimum. The resolution of source location depends on the grid size but the location error ranges have been seldomly defined in moment tensor inversion analysis. Lanza and Waite (2018) have conducted synthetic tests of moment tensor inversion of LP (0.5-4 Hz) signals with a nonlinear approach. They assumed source models, synthetic networks with as many as 40 stations, variable distance and azimuthal distributions, a known velocity model, and the topography of Pacaya volcano, a Stratovolcano in Guatemala. The synthetic tests illustrated that distant stations from a source, the number of stations less than eight and the coverage gap of seismic stations greater than 130° generally increase uncertainty in inversion results. They also showed that sources are still recoverable when as few as four stations with fairly good azimuth coverage are used. However, only a few volcanoes have the seismic networks that satisfy such conditions to correctly determine the source location and mechanism

results because of limited topographic conditions and manpower. Especially, slight errors in the source will have a significant effect on the magma ascent model in Strombolian and Vulcanian eruptions where shallow dynamics are considered to be important. Therefore, undefined source errors and poor observation conditions should be resolved.

Acoustic waves associated with explosions have also been energetically analyzed for understanding the explosion dynamics. Volcanic explosions sometimes generate shock waves that travel from the crater to the atmosphere. The shock waves attenuate as propagating away from the crater and turn to sound waves. The energy of an explosion are estimated from acoustic wave amplitude and propagating distance from the source (e.g., Firstov and Kravchenko, 1996; Johnson et al., 2003; Vergniolle et al., 2004). Johnson and Aster (2005) estimated amplitude ratios of acoustic and seismic amplitudes during Strombolian eruptions at Karymsky and Erebus volcanoes. The relative partitioning of acoustic and seismic energy during Strombolian eruptions suggests that magma properties, conduit obstruction, and/or fragmentation depths affect the amplitude ratios. This quantity has been applied for monitoring and improving understanding of key aspects of eruption dynamics (Richardson et al., 2014; Jolly et al., 2016). Hasib (2019) calculated spectral ratios of acoustic waves between large amplitude events and small amplitude events at Sakurajima volcano and Shinmoe-dake volcano, Japan. The results show that the amplitude ratios are almost flat at all frequency range. They interpreted that the constant pulse width may be controlled by the geometry of the crater. The propagation speed of acoustic waves is slower than seismic wave velocities. The travel time and path differences enable us to constrain the geometry such as the conduit length and magma surface location (Ripepe et al., 2001; Harris and Ripepe, 2007; Ishii et al., 2019).

1.2 Geophysical observation and analyses of eruptions at Stromboli volcano

Stromboli volcano (924 m a.s.l.) is one of the most active volcanoes in the world. It is located at the northern end of the Aeolian island arc in the Tyrrhenian sea in Italy. Three main craters are located within a 300 m long by 140 m wide terrace in the northern peak of the volcano (Neri and Lanzafame, 2009). Small explosions typically occur at a rate of 3-10 events per hour from these craters, and swarm-like eruptive activity occasionally reaches 20-30 events per hour (Ripepe et al., 2008). Ash-dominated or bomb-dominated eruptions have been mainly observed at both of NE and SW craters, while these eruption types sometimes change with time (e.g., Ripepe et al., 1993; Patrick et al, 2007;

Delle Donne et al., 2016; Gaudin et al., 2017).

These “Strombolian” eruptions have been monitored in real time by using a geophysical monitoring system. Seismometers, infrasonic sensors, tilt sensors, and thermal cameras have been deployed near the craters (~ 1 km away) by the University of Florence (Ripepe et al., 2004; Valade et al., 2016), the Istituto Nazionale di Geofisica e Vulcanologia (INGV) (e.g., Martini et al., 2007; Burton et al., 2009). Analyses of observation data recorded by these permanent monitoring systems or other temporary observation networks enabled us to understand the dynamics of eruptions at Stromboli volcano. For example, the seismic sources excited by explosions are determined at depths shallower than 200 m beneath the summit crater from analyses of data recorded by small-apertures seismic arrays deployed on the north flank of the volcano (Chouet et al., 1997). The VLP seismic source is located at ~500 m a.s.l., from moment tensor inversion analysis (Chouet et al., 2003, 2008; Auger et al., 2006, Giudicepietro et al., 2009) or polarization analysis (Marchetti and Ripepe, 2005, Martini et al., 2007). The centroid of the VLP source located outside the crater rim along the Sciara del Fuoco slope has been interpreted as a pressure source of opening/closing crack embedded in the volcanic medium. The VLP seismic source had been considered to be stable in space and time, but the recent studies found significant spatio-temporal changes in VLP seismic source before and after the flank effusive eruption that occurred on 27 February 2007 (Giudicepietro et al., 2009; Ripepe et al., 2015) and on 7 August 2014 (Valade et al., 2016) by a polarization analysis. Such spatio-temporal changes in VLP seismic source have been rarely reported at other volcanoes so that further analyses of VLP earthquakes are needed to understand Strombolian eruptions. The LP seismic signal at Stromboli volcano in the dominant frequency band of 0.5-2.5 Hz has been interpreted as an oscillatory response of the shallowest segment of the fluid-filled conduit associated with rapid expansion and ejection of a gas slug (Chouet et al., 1997). This previous study illustrates that the particle motions of near-field stations and far-field seismic array and the arrival time of seismic body wave phases and acoustic waves in the near-field stations are consistent with a gas-piston mechanism operating on a shallow part (< 200 m deep) of the conduit.

The processes including generation, ascent and bursting of a large gas slug at the magma free surface, which are presented by Blackburn et al. (1976), have been used as plausible origins of seismic, acoustic and thermal signals associated with Strombolian eruptions. This large gas slug model is imagined from the gas bubble bursts visually observed on the lava surface (e.g., Blackburn et al., 1976, Vergniolle and Brandeis, 1996). Such large slug ascent is also examined by numerical simulations and laboratory experiments (e.g., Vergniolle and Jaupart, 1990; Vergniolle, 1998;

Seyfried and Freundt, 2000; James et al., 2008, 2009). Vergniolle (1998) numerically investigated the gas slug ascent process in the conduit using the equations of motion of liquid magma and equations of state of gas in the slug. James et al. (2008) modified the model of Vergniolle (1998) by including the motion of magma surrounding the gas slug. Gas slug ascent velocity and associated pressure changes measured in several laboratory experiments (e.g., Vergniolle and Jaupart, 1990; Seyfried and Freundt, 2000; James et al., 2006; Llewellin et al., 2011) are well matched with the model presented by James et al. (2008). The results of the numerical simulations and laboratory experiments are used to relate observed data such as the amount of gas ejection and the magnitude of infrasound associated with explosions. A laboratory experiment examined generations of acoustic signals during gas growth, flow and burst in a liquid inside and outside the water in the tube (Ripepe et al., 2001). A sensor set outside the water in the tube recorded a low-frequency signal as soon as the slug started to rise, which is followed by a high-frequency signal when the bubble is broken at the water surface. Such temporal evolution of the slug ascent and generation of acoustic signal are used to quantitatively interpret the conduit process of Stromboli volcano. From arrival time difference between low-frequency seismic signals and infrasound recorded at a station 300 m away from the crater, the slug ascent velocity was estimated to 10-70 m/s (Harris and Ripepe, 2007). Such velocities of slug ascent were also observed for a different observation period at Stromboli volcano (13-25 m/s, Gurioli et al. 2014) and for Strombolian eruptions at Aso volcano (1-160 m/s, Ishii et al., 2019). These estimated velocities are much larger than that theoretically predicted from the slug motions in the tube entirely filled with liquid magma: the slug ascent velocity is 1.5 and 3.4 m/s for the conduit radius of 1 and 5 m, respectively (Batchelor, 1967). Kawaguchi and Nishimura (2015) numerically investigated spatio-temporal changes in volcanic deformation due to gas slug ascent in an open conduit, using a gas slug ascent model of James et al. (2008). However, not only the spatio-temporal characteristics but also amplitudes of tilt motion observed at Stromboli could not be reproduced by the numerical examination, suggesting modification of the gas slug ascent model or introduction of other mechanisms of the Strombolian eruptions. These discrepancies should be necessary to be resolved for quantitative understanding of volcanic eruptions.

1.3 Objectives of this study

Strombolian or Vulcanian eruptions repeatedly occur at several volcanoes around the world. The accumulation of the data associated with these repetitive eruptions is quite important because these data often show common characteristics about the eruption dynamics such as amplitude, spectral

peak, duration, and so on. The analyses of these data are the most fundamental in understanding volcanic eruptions. The information obtained by the fundamental analyses also enables us to discuss the temporal changes in volcanic activities. For example, basic analyses of seismic signals, deformation and infrasound in many years contributed to construct the model of the explosive eruption at Sakurajima volcano (Tameguri et al., 2002; Iguchi et al., 2008). This study focuses on seismic and acoustic data associated with very frequent explosions at Stromboli volcano to understand the mechanism of Strombolian eruptions by conducting source mechanism analysis, hypocenter determination of eruption earthquakes and infrasound and verification of these methods.

As described so far, the dynamics of Strombolian eruptions have been investigated by observation, laboratory experiments, and numerical simulations. These studies clarified that fluid motions of the complex gas-liquid flows occur in the shallow part of the volcano from surface to only a few hundred meter in depth before and during the eruptions. Several models to explain Strombolian eruptions have been proposed, but there is no completely established model. For example, the formation processes of a large gas bubble such as a slug have been understood either by coalescence of smaller bubbles at geometrical discontinuities in the conduit (Vergniolle and Jaupart, 1986; Jaupart and Vergniolle, 1988; Ripepe et al., 2001) or by differential ascent rate of the bubbles with respect to the magma column (Parfitt and Wilson, 1995). Therefore, the geometrical information that can be obtained by geophysical analyses such as seismic, infrasonic, and deformation approaches are quite important to explain such fluid dynamics. As mentioned in section 1.2, seismic and acoustic wave analyses in the previous studies have estimated the locations of explosion source and VLP pressure source and the mechanism of the pressure source. It is necessary to determine these sources with high accuracy for quantitively explaining the dynamics at only a few hundred meters in depth at the “relatively” small island. However, it has been difficult to accurately determine these source locations and mechanisms because Stromboli volcano suffers topographical constraints such as the Sciara del Fuoco slope. The seismic networks in the previous studies did not necessarily satisfy the condition for better constraint of the source location and mechanism results explored by Lanza and Waite (2018). Therefore, it is necessary to reconsider the geometry of the shallow magma system estimated by geophysical observation as well as the better network configuration.

The University of Florence deployed four seismo-acoustic and one seismic station at Stromboli volcano and conducted a temporary observation in the end of September 2016. The stations were deployed close to the active craters as much as possible. As a result, the stations were located at

only 100-300 m away from the main craters, surrounding the craters. Such normally difficult observation enables us to analyze high quality data with high signal-to-noise ratios, making accurate measurement of arrival times of seismic and acoustic signals possible. By using these data, this study conducts the analyses of source locations and mechanisms of eruption earthquakes. Using a moment tensor inversion method, we estimate the source location and mechanism of VLP earthquakes associated with the volcanic eruptions to clarify the pressure source related to the gas or fluid motions. We also apply a source location method using waveform correlations to obtain detailed relative locations of many VLP seismic events. In order to determine the location of the explosion source which excites high-frequency seismic waves and infrasound after VLP seismic signals are observed, we use travel times of these two waves. Based on the time lag between the origin time of the VLP earthquake and that of the explosion and the difference of the source locations, we quantitively clarify the geometry of the shallow magma system and the gas or fluid ascent in the conduit/reservoir before/during the volcanic eruptions. These information will enable us to construct an improved model of the repetitive eruptions at Stromboli volcano.

As mentioned in Section 1.1, in case of Vulcanian eruptions, the migration of seismic sources preceding or during the eruptions has been reported at several volcanoes. However, only a few studies have detected the migration of seismic sources for Strombolian eruptions (Rowe et al., 1998). Especially, the source locations and mechanism of VLP or LP earthquakes are generally evaluated as the kinematics of the centroids. Therefore, it is necessary to carefully analyze the waveforms with lapse times to discuss the gas and fluid flows below the craters and to understand the dynamics of small repetitive eruptions. This study firstly examines the centroids of VLP or LP earthquakes and then discusses the source locations of the seismic waves at different time sections.

In Chapter 2, we introduce the temporary observation conducted in September 2016. We show the characteristics of seismic and acoustic data recorded at a very-near-field condition. In Chapter 3, we perform moment tensor inversion including tilt responses (Maeda et al., 2011) by using the temporary and permanent network data to determine the source mechanisms and locations of VLP and LP earthquakes associated with small repetitive eruptions. This is the first case to conduct the moment tensor inversion by using very-near-field data. We also verify the sensitivity of the inversion results inferred from the very-near-field network and the utility or issues of the network for estimating the source locations and mechanisms by conducting synthetic tests of inversion and comparing with the network configuration which resembles to previous studies. In Chapter 4, we apply a precise relative hypocenter determination method presented by Sugimura et al. (2015) to

the VLP earthquakes for evaluating the variation of the source around the centroid. In Chapter 5, we conduct hypocenter determination of eruption earthquakes that excite high frequency seismic waves and infrasound by using the travel time difference between these two waves. Based on the spatio-temporal distribution of VLP source and explosion source, we measure the propagation velocity of magma or gas bubbles after VLP seismic waves are excited. We discuss magma/gas motions inside the conduit and/or reservoir by assuming the different conduit geometries and model parameters. In Chapter 6, We discuss the dynamics of the eruptions at Stromboli volcano. We examine the migration of VLP seismic source before or during/after the explosions. We also discuss the consistency and validity of the results of source locations and conduit parameters by comparing the results obtained from different observation data. In Chapter 7, we conclude this study.

Chapter 2

Observation and data: A temporary very-near-field observation network in September 2016

2.1 Observation network

The volcanic activities at Stromboli volcano have been continuously monitored by an integrated geophysical observation network of the University of Florence. The permanent seismic network (Figure 2.1) consists of four broadband stations (ROC, PZZ, STR, and SCI). These stations are equipped with broadband seismometers (Güralp CMG-40 T, 800 V/m/s with an eigenperiod of 30 s). One 5-element infrasonic array (EAR) has been deployed to monitor which crater excites infrasound signals accompanied by explosions. This array has an L-shape geometry with an internal spacing of ~100 m to record coherent infrasonic waves at 1–10 Hz frequency band (Ripepe et al., 2004). The acoustic data of the array are recorded by a 16 bits acquisition system with a sampling rate of 54.2 Hz. Two tiltmeter stations (LFS and OHO) located within 1 km from the active craters are equipped with Pinnacle 5000T electrolytic borehole sensors. The tilt motions are recorded with a nominal resolution of ±1 nrad and a low-pass cut-off frequency of ~0.02 Hz at −3 dB at 1 Hz sampling rate (Genco and Ripepe, 2010). These seismic, acoustic and tilt data are radio-transmitted to the monitoring center of the Department of the Civil Protection (COA) on the island and these are collected, processed, and published in real time on the Web (Valade et al., 2016).

In the end of September 2016, a temporary seismic and acoustic observation was conducted (Figure 2.1). The temporary seismic network consisted of five broadband stations (ST1, ST2, ST3, ST4 and ST5). These stations were equipped with Güralp CMG-40T broadband seismometers and the data were recorded by 24 bits Güralp CMG24 digitizers with a sampling rate of 100 Hz. The network had been deployed in order to have a better azimuthal coverage of and as close as possible to the active area, only 100-300 m away from each crater. The acoustic signals were also recorded by infrasound microphones at ST1, ST2, ST3 and ST4. These seismo-acoustic stations started to record the signals from about 16:30, 24 September,. The stations except ST4 were withdrawn on 29 September in UTC. The station ST4 is still operating as a permanent station, which is renamed as SDK.

2.2 Data

We analyze the seismic data at eight broadband stations except for SCI. We also use acoustic data at ST1, and seismic signals recorded at two tiltmeter stations from 17:00, 24 September to the end of 28 September. We show an example of seismic and acoustic signals associated with a small explosion recorded at ST1, which is the closest station to the active craters (Figure 2.2). The waveform converted from velocity (Figure 2.2 (a)) to displacement (Figure 2.2 (b)) illustrates that the onset of the VLP signal is followed by the onsets of the high frequency seismic and acoustic signals (Figure 2.2 (c)). The Fourier amplitude spectrum of raw seismogram at ST1 in Figure 2.2 (d) indicates that there are two dominant spectral peaks at around 0.1 Hz and 10 Hz. However, the second spectral peak around 10 Hz is not consistent with the previous study indicating that the frequency content of the seismic signals between 0.8 and 5 Hz is dominated (Ripepe, 1996). The Fourier spectrum of the seismogram at STR (Figure 2.2 (d)) shows that the frequency content is dominant around 0.1 Hz and 2-5 Hz. Such characteristic is seen at the other broadband seismic stations. Also, the spectral amplitude around 2 Hz is slightly large at ST1 so that the dominant spectral peak around 10 Hz may be attributed to site effects. The acoustic signal at ST1 (Figure 2.2 (d)) shows a dominant spectral peak at about 2 Hz.

The time series of seismogram and infrasound at ST1 are illustrated in Figure 2.3. The seismic and acoustic amplitudes indicate that the magnitude gradually increased until September 26, and the activity rapidly decreased from the September 27. The EAR infrasonic array monitoring system of the University of Florence (Ripepe et al., 2004) detected that the eruptive activity during the observation period mainly concentrated at NE crater and the magnitude of the activity had changed before and after 26 September (Figure 2.4). However, since this study focuses on the dynamics of small repetitive eruptions, the temporal evolution of the activity is not discussed in this thesis.

We mainly analyze VLP seismic signals which are accompanied with high frequency seismic and acoustic signals in this study. In order to analyze as many events as and as high signal to noise ratios as possible, we set thresholds for the selection of seismic and acoustic amplitudes at ST1: 5 μm/s for seismogram (UD component, 0.05-0.2 Hz) and 10 Pa for infrasound (0.1-20 Hz). We detect 154 events during the period. However, there was a temporary missing record at PZZ between 20h32m07s, 25 September and 07h05m08s, 26 September. In addition, the records at five temporal broadband stations was temporarily not available several times, which are shown by gray shades in Figure 2.3. Finally, 103 events are selected to analyze seismic signals recorded at all seismic and tilt stations.

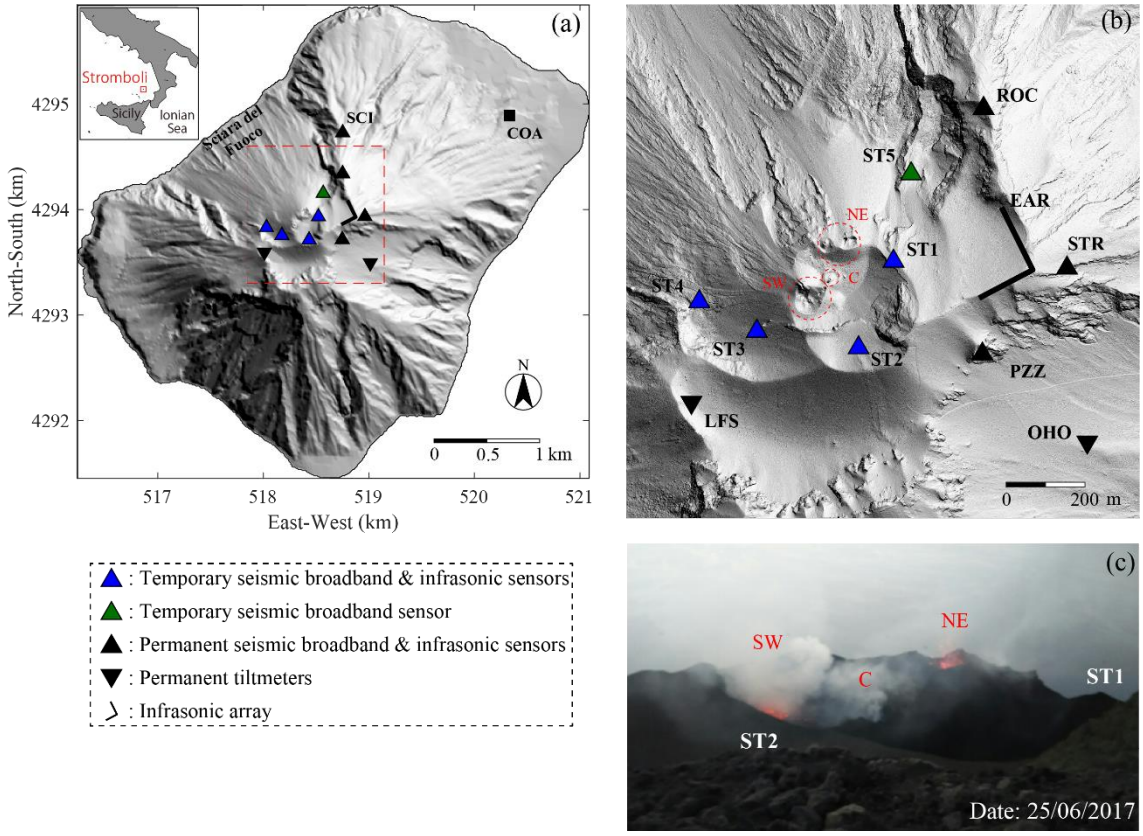

Figure 2.1 (a) Shaded relief map and locations of the geophysical sensors at Stromboli volcano, Italy. The signals are digitally transmitted and processed in real time at the operations center (COA) of Department of Civil Defense shown by the black square. (b) Locations of the geophysical sensors used in this study. (c) Photo of the craters taken from the summit. The location of ST1 and ST2 are written in white letters.

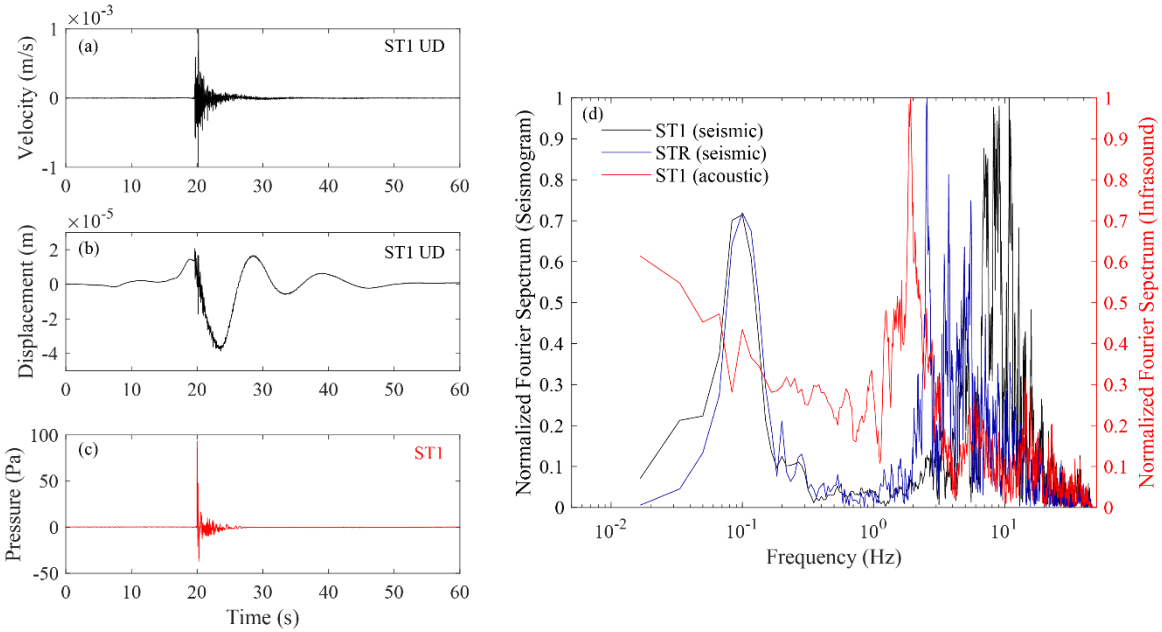

Figure 2.2 (a) Raw velocity seismogram of UD component at ST1 associated with an explosion at NE crater. (b) A record integrated into displacement from the velocity seismogram in Figure 2.2 (a). (c) Infrasound at ST1 recorded at the explosion. (d) Fourier spectra of the seismogram at ST1 (black), seismogram at STR (blue) and infrasound at ST1 (red). These Fourier spectra are normalized by their maximum amplitudes.

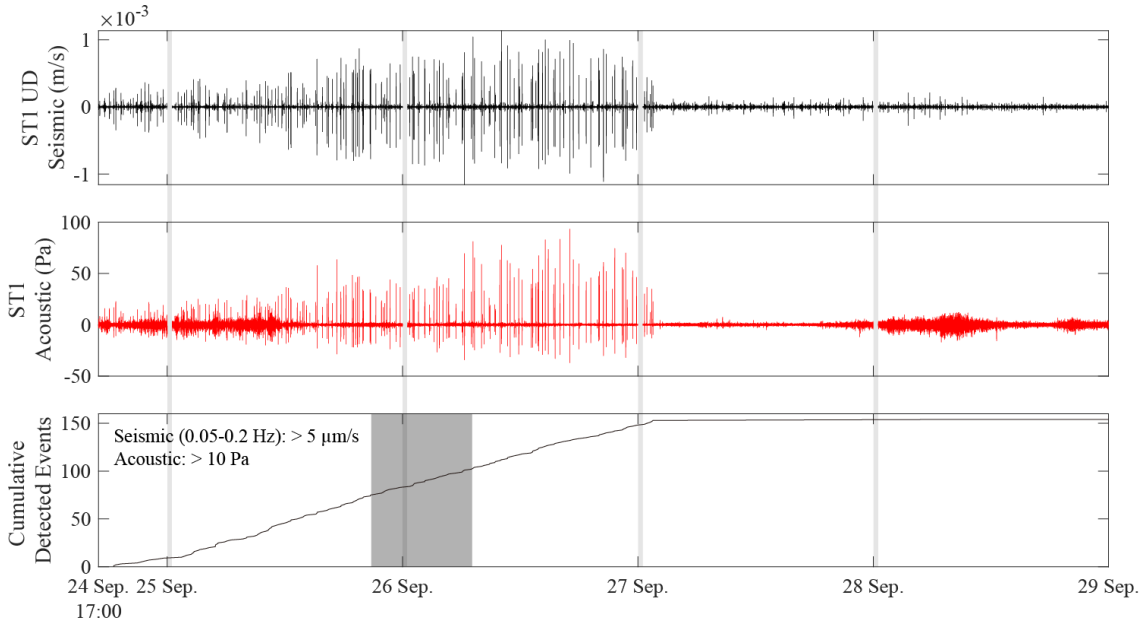

Figure 2.3 Time series of raw seismogram at UD component of ST1, raw infrasound at ST1, and the cumulative detected events. The gray shaded areas indicate the temporary missing of data at ST1, ST2, ST3, ST4 and ST5 in the beginning of each day and at PZZ from 20h32m07s, 25 September and 07h05m08s, 26 September. The events are detected by the thresholds of amplitude of seismic (0.05-0.2 Hz) and acoustic signals.

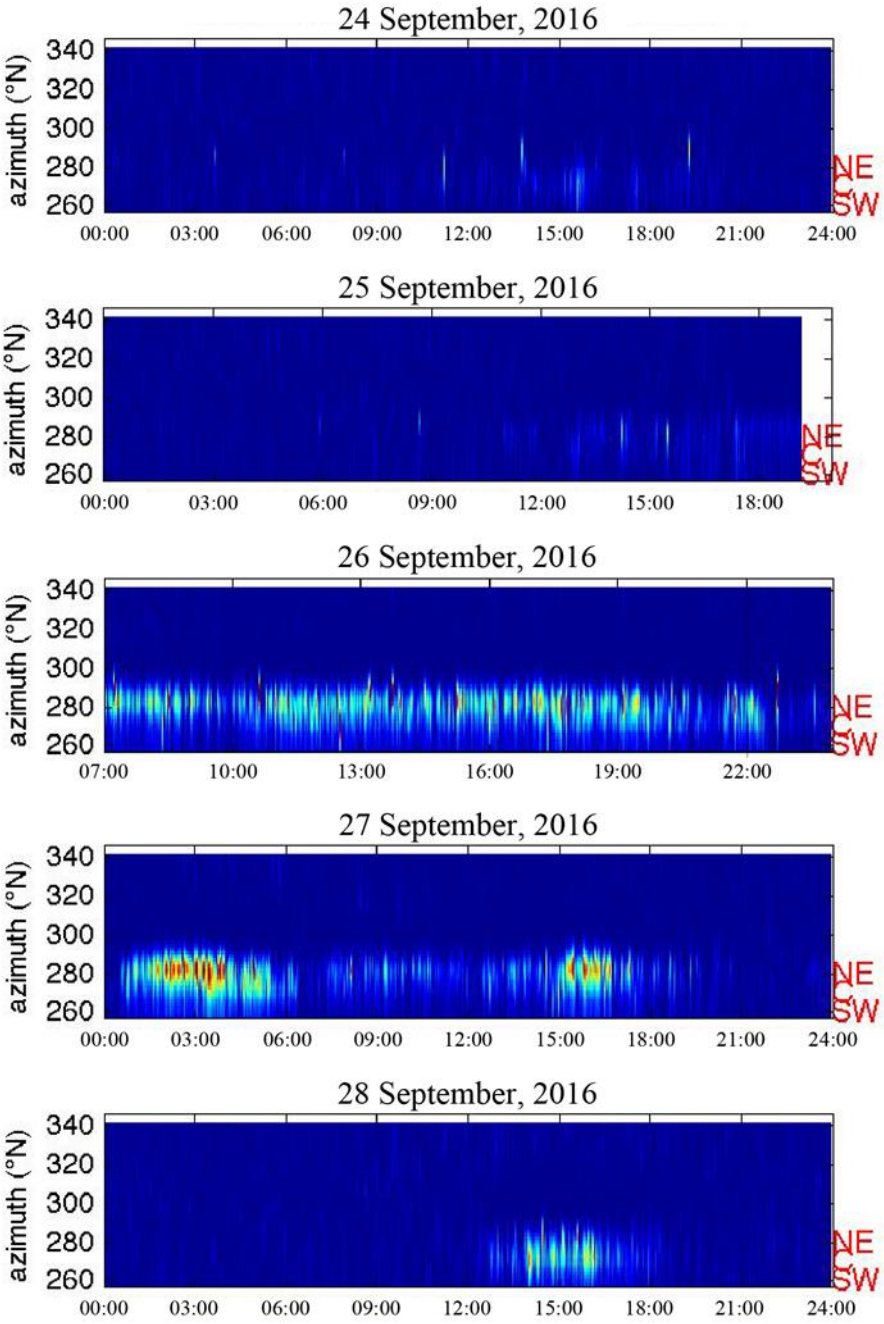

Figure 2.4 Samples of back azimuth analysis of the infrasonic array from 24 September to 28 September 2016. Hot colors represent higher values of semblance which indicate the position of eruptive craters. During the observation period, the Strombolian activity was mainly observed at NE crater and observed a little at C crater. This figure is courtesy of the University of Florence.

Chapter 3

Moment tensor inversion of eruption earthquakes

In this chapter, we examine source mechanism and location of the earthquakes associated with small repetitive eruptions at Stromboli volcano by applying a moment tensor inversion method. We first introduce the method of moment tensor inversion considering tilt responses to deal with seismograms contaminated by both translational and tilt motions. We then apply the method to the seismic data at 0.05-0.2 Hz, 0.2-0.5 Hz and 0.5-1.0 Hz. The frequency band of 0.05-0.2 Hz is the lower frequency part of the VLP band that includes the dominant frequency content in the seismograms (Figure 2.2 (d)). The frequency band of 0.2-0.5 Hz is the higher frequency part of the VLP band that represents another small spectral peak. To determine source location and mechanism of long-period (LP) seismic signals, we select the frequency band at 0.5-1.0 Hz at which seismic scattering effects are small. This is the first time to perform moment tensor inversion by using a very-near-field seismic network, so we examine the resolution of the inversion results based on model resolution matrices and synthetic tests of network performance and finite source modelling.

3.1 Method

We apply a moment tensor inversion method of Maeda et al. (2011) to VLP and LP seismic signals associated with small explosions. This method is developed to deal with horizontal seismograms strongly contaminated by tilt motions. The observed seismogram generated by a moment-tensor is described in the time domain as

$$U_n^{\mathrm{obs}}(t) = M_{pq}(t) * G_{np,q}(t), \qquad p,q = x,y,z, \tag{3.1}$$

where $U_n^{\mathrm{obs}}(t)$ is the seismogram in n-th component at a receiver at time t, $M_{pq}(t)$ is the moment tensor where p is the direction of the force and q is the direction of the arm of the moment, $G_{np,q}(t)$ is the Green's function in n-th component excited by a unit impulse source acting to the p-th direction, the notation q indicates spatial differentiation, and the symbol * indicates convolution. The Fourier transform of equation (3.1) can be represented as

$$U_n^{\mathrm{obs}}(\omega) = M_{pq}(\omega) G_{np,q}(\omega), \tag{3.2}$$

where ω is the angular frequency. Here, we indicate the contribution of both translational and tilt responses in the observed seismogram:

$$U_n^{\mathrm{obs}}(\omega) = M_{pq}(\omega)\left[G_{np,q}^{\mathrm{trans}}(\omega) I_n^{\mathrm{trans}}(\omega) + G_{np,q}^{\mathrm{tilt}}(\omega) I_n^{\mathrm{tilt}}(\omega)\right], \tag{3.3}$$

where $G_{np,q}^{\mathrm{trans}}(\omega)$ and $G_{np,q}^{\mathrm{tilt}}(\omega)$ are the Fourier spectra of n-th component of Green's functions for translational and tilt motions, respectively, and $I_n^{\mathrm{trans}}(\omega)$ and $I_n^{\mathrm{tilt}}(\omega)$ are the n-th component of seismometer's responses to translational and tilt motions, respectively. The response of horizontal seismometer to ground displacement can be obtained from the poles and zeros of the seismometer (e.g., Aoyama and Oshima, 2008; Genco and Ripepe, 2010):

$$I_n^{\mathrm{trans}}(\omega) = \frac{\omega^2}{\sqrt{\left(\omega_0^2 - \omega^2\right)^2 + (2D\omega_0\omega)^2}}, \tag{3.4}$$

where ω_0 is the natural period of the seismometer and D is the damping constant. The response function of horizontal seismometer to ground tilt can be expressed as

$$I_n^{\mathrm{tilt}}(\omega) = \frac{-g}{\sqrt{\left(\omega_0^2 - \omega^2\right)^2 + (2D\omega_0\omega)^2}}, \tag{3.5}$$

where g is the gravitational acceleration. Therefore, the tilt response on the horizontal seismometer can be written as

$$I_n^{\mathrm{tilt}}(\omega) = -\frac{g}{\omega^2} I_n^{\mathrm{trans}}(\omega). \tag{3.6}$$

For a vertical seismometer, the tilt response function $I_n^{\mathrm{tilt}}(\omega)$ can be regarded to be almost exactly zero (e.g. Graizer 2006; Aoyama 2008; Maeda et al., 2011).

The matrix form of equation (3.3) incorporating equations (3.4), (3.5) and (3.6) can be written as

$$\mathbf{d} = \mathbf{Gm}, \tag{3.7}$$

where $\mathbf{G}$ is the matrix of Green's functions including both translational and tilt motions and these two response functions, $\mathbf{d}$ is the seismic data vector and $\mathbf{m}$ represents the source mechanism vector that consists of six moment tensors. The least squares solution of the source mechanism is written as

$$\mathbf{m}^{\mathrm{S}} = [\mathbf{G}^{\mathrm{H}}\mathbf{G}]^{-1}\mathbf{G}^{\mathrm{H}}\mathbf{d}, \tag{3.8}$$

where the symbol $^{\mathrm{H}}$ indicates the conjugate transpose (Hermitian). The synthetic seismograms are obtained by the inverse Fourier transform of the product of the Green's functions $\mathbf{G}$ and the solution $\mathbf{m}^{\mathrm{S}}$. In this method, the tilt effect is included in the Green's function term, although the decomposition of the observed seismogram into translational and tilt contributions is not required.

We compute the Green's functions by a software package of Open-source Seismic Wave Propagation Code (OpenSWPC, Maeda et al., 2017). This numerical simulation of seismic wave propagation is based on the staggered-grid finite difference method with the fourth-order accuracy in space and second-order accuracy in time (Levander, 1988). The Green's functions are convolved with a cosine function to stabilize the inversion:

$$S(t) = \frac{1}{2}\left[1 - \cos\left(\frac{2\pi t}{t_r}\right)\right], \quad 0 \le t < t_r$$

$$0, \qquad\qquad t \ge t_r \tag{3.9}$$

where t_r is the rising time of the source time function.

Our computational domain is centered at the summit and it consists of a grid with 401×401×201 nodes in the north-south (NS), east-west (EW) and up-down (UD) directions equispaced by 10 m for a total length of 4×4×2 km. We note that positive x and y directions are set to be north and east, respectively, and z direction is vertical one with downward positive UD. This Cartesian coordinate is based on the computational one in OpenSWPC. However, the vertical component of the output waveform is changed to be positive upward in this software. We assume P wave velocity V_p of 3.5 km/s, S wave velocity V_s of 2.0 km/s, and the medium density ρ of 2650 kg/m^3 (Chouet et al., 1998, 2003). The quality factors of P and S waves, Q_p and Q_s are set to be 50. The node spacing of the point sources is 50 m with 9 × 9 × 8 in 3-D mesh. Considering the topographic

condition of the volcano, we distribute 543 point sources (Figure 3.1). Firstly, the Green's functions for translational motion $G_{np,q}^{\mathrm{trans}}(\omega)$ are yielded at the eight broadband seismic stations by convolving the cosine function in equation (3.9) for $t_r = 0.5$ s. We calculate the Green's functions in velocity response and apply the data vector $\boldsymbol{d}$ as velocity seismograms. This is because the displacement Green's functions are strongly affected by permanent displacements, which may lead to phase reversal in the time function of $\boldsymbol{m}^{\mathrm{s}}$ due to the cyclic convolution. Then, the Green's functions for tilt motion $G_{np,q}^{\mathrm{tilt}}(\omega)$ are obtained by computing the vertical displacement at the grids around the stations with 10 m interval, taking the difference of the vertical displacement in the east-west and north-south directions, and converting to the velocity responses.

We determine the best fit source location and source mechanism which show the minimum misfit between the observed and synthetic seismograms. The misfit is calculated by the following equation (e.g., Ohminato et al., 1998),

$$E_1 = \frac{\sum_{n=1}^{N_t}\sum_{k=1}^{N_s}\left(U_n^{\mathrm{obs}}(k\Delta t) - U_n^{\mathrm{syn}}(k\Delta t)\right)^2}{\sum_{n=1}^{N_t}\sum_{k=1}^{N_s}\left(U_n^{\mathrm{obs}}(k\Delta t)\right)^2}, \tag{3.10}$$

where $U_n^{\mathrm{obs}}(k\Delta t)$ and $U_n^{\mathrm{syn}}(k\Delta t)$ are the k-th time sample of the observed and synthetic seismograms, N_t is the number of data traces and N_s is the number of samples in each trace.

3.2 Results

We firstly apply the inversion method to the seismograms in which a zero-phase Butterworth band-pass filter of 0.05-0.2 Hz is applied. Figure 3.2 shows the distribution of optimal source locations for 103 events. The number of events for each source grid is indicated by the different size and color of a hexagon or a gray circle. We define source clusters only from the difference in these locations and label the two main source clusters as location (i) (63 events) and location (ii) (28 events). The result shows that most of the VLP (0.05-0.2 Hz) sources are located at the west of or the edge of the crater rim with 600 or 650 m a.s.l. The depth becomes about 100-150 m shallower than the source location result of previous studies (e.g., Chouet et al., 2003, 2008) which is shown by a gray star.

We show the results of source mechanism and waveform fitting for the events in location (i) and (ii). Figures 3.3 (a) and (b) show the average of moment tensor time functions of all events in location (i) and (ii). The moment tensor solutions for both clusters indicate that the vertical dipole component in the source mechanism M_{zz} is dominant. Figures 3.3 (c) and (d) represent

eigenvectors for the “average” moment tensor solutions shown in Figures 3.3 (a) and (b), respectively. The amplitudes of eigenvectors are represented by the eigenvalues of the maximum amplitudes of moment tensor time functions. Figures 3.4 (a) and (b) compare the waveforms of observation and synthetics for the two type events. The waveforms are well matched with each other for both events ($E_1 = 10.0$ % and 10.2 %). The average value of E_1 in all the 103 events is 10.7 %. Also, the average values of the squared errors in the events in location (i) and (ii) are 9.6-13.2 % and 7.6-13.1 %, respectively.

Figure 3.5 compares the root-mean-square (RMS) amplitude distribution between the events in location (i) and (ii). The amplitude distributions of both the two source clusters are almost same for all events. The comparison shows that the amplitude distributions at NS component of ST3 and ST5 are slightly different between the two source clusters. Note that these amplitude distribution changes could not be seen in the permanent seismic network. Figures 3.6 (a) and (b) compare the normalized VLP waveforms between the two source clusters at NS component of ST3 and ST5. These waveforms are aligned in time at 20 s based on the arrival time of infrasound. The comparisons illustrate that the waveforms before about 20 s seem to be similar to each other. However, the waveforms after about 20 s in location (ii) seem to be dominated by longer period than the waveforms in location (i). Such a slight difference in waveforms may reflect temporal changes in the source locations and/or mechanisms during/after the explosions.

The inversion result for the higher frequency part of the VLP band at 0.2-0.5 Hz shows that the 57 events in all 103 events are located just below C crater (Figure 3.7), which is labeled as location (iii). This location is shifted 100 m east from the main source cluster for 0.05-0.2 Hz (location (i)) shown in Figure 3.2 so that it becomes closer to NE crater. We define source clusters only from the difference in the source locations and label the top two clusters as location (iii) and location (iv) (13 events). Figures 3.8 (a) and (b) show the solutions of the moment tensor time functions for the events in the two source clusters. The solutions for the events in location (iv) seem unstable but the solutions for the events in location (iii) are stable and the diagonal moment tensor components are dominated. Due to the wavelength in the frequency band and the condition of the network, the resolution of the source mechanisms may not be still assured. The mean value of E_1 for the 103 events is 15.1 %

Figure 3.9 shows the distribution of optimal source locations for the 103 seismic events at 0.5-1.0 Hz (LP). We label the main three clusters as location (v) (21 events), location (vi) (17 events), and location (vii) (14 events). The result shows that source locations are fluctuated compared to the

lower frequency band because of lower signal-to-noise ratios of signals or more complex waveforms which may be affected by heterogeneities or scattering processes in the volcanic structure. However, the source clusters are further shifted to the east and the depths become shallower compared with VLP sources. Particularly, the events in location (v) and (vii) are roughly below NE crater. These sources are located nearby those of earthquakes at 0.5-2.5 Hz frequency band (Chouet et al., 1997). Figure 3.10 shows the solutions of the moment tensor time functions for the events in three source clusters. The solutions become further unstable and the mean value of E_1 for all the 103 events is 23.0 %. The results indicate that the diagonal moment tensor components are also dominated.

Figure 3.11 compares the causal band-pass filtered waveforms of UD component at ST1 at different frequency bands (0.05-0.2 Hz, 0.2-0.5 Hz and 0.5-1.0 Hz) to see temporal evolution. This figure shows that the origin times of the initial motion are almost same at different frequency bands. Almost no origin time differences at different frequency bands may indicate that these sources are almost simultaneously excited. The relation between the origin times and the source locations is discussed in detail in Chapter 5.

3.3 Discussion

3.3.1 Comparison with the source locations determined by semblance analysis

Hereafter, we mainly focus on the seismic signals at 0.05-0.2 Hz to verify the accuracy of source locations and mechanisms that are determined by using the very-near-field data because the solutions are obtained with lower errors (E_1) than other frequency bands.

The locations of the VLP (0.05-0.2 Hz) sources determined in this study show 100-150 m shallower than the source location determined by moment tensor inversion (Chouet et al., 2003, 2008) and polarization analysis (Marchetti and Ripepe, 2005). In order to examine whether similar source location can be determined by another source location method, we compare our results with the source location of the VLP signals that are determined by a semblance analysis of Kawakatsu et al. (2000). This method measures waveform coherency among the stations and high coherency indicates the seismic energy isotropically radiates from a source to all stations as compressive body waves. The waveform semblance can be expressed in order to incorporate information contained in rectilinearity of the particle motions of the seismograms by emphasizing the radial component and

subtracting the other components as follows;

$$S_3 = \frac{1}{D}\sum_{j=1}^{L}\left\{\left(\sum_{i=1}^{N} R_{i,j(i)}\right)^2 - N\left(\sum_{i=1}^{N} V_{i,j(i)}^2\right) - N\left(\sum_{i=1}^{N} H_{i,j(i)}^2\right)\right\}, \tag{3.11}$$

where L is the total number of time samples, N is the total number of stations, $R_{i,j(i)} \equiv R_i(t_i + j\Delta t)$ is the radial component of the seismogram at i-th station at $j(i)$-th time sample from the start time t_i which is shifted by the travel time from an assumed source to the station, $V_{i,j(i)}$ is the component in the direction perpendicular to R within the vertical plane which contains both source and receiver, and $H_{i,j(i)}$ is in the horizontal component perpendicular to both R and V. The scaling factor D can be taken as

$$D = N\sum_{j=1}^{L}\sum_{i=1}^{N} R_{i,j(i)}^2. \tag{3.12}$$

Before calculating equation (3.11), each seismogram is normalized to give equal weight of amplitude information to each station. The RMS amplitude of signal of each station becomes unity as follows,

$$RMS_i^2 = \frac{1}{L}\sum_{j=1}^{L}\left(R_{i,j(i)}^2 + V_{i,j(i)}^2 + H_{i,j(i)}^2\right) = 1. \tag{3.13}$$

We calculate the semblance values at each point source by grid search in the same region as moment tensor inversion. We assume a wave velocity of 3.5 km/s. Figure 3.12 (a) illustrates the source distribution and the semblance values are statistically examined in Figure 3.12 (b). The result shows that the source locations are same for 100 events in all 103 events. These are located at about 200 m west of NE crater. The source depths also become about 100 m shallower than previous studies (e.g., Chouet et al., 2003, 2008; Marchetti and Ripepe, 2005). The semblance values are above 0.80 for almost all events. The high coherency representing strong rectilinearity of the waveforms suggests that the source mechanism of the VLP signals is dominated by more isotropic volumetric changes. The main source location determined by the semblance analysis is slightly different from the two main clusters determined by the moment tensor inversion (location (i) and

(ii)). Although the source locations are separated into two main clusters by the moment tensor inversion (location (i) and (ii)), there is no such separation in the semblance results. This may be due to the difference in the assumption of the source mechanism between the two analyses. The semblance analysis supposes an isotropic point source so that it may be difficult to catch the slight differences in the source locations or mechanisms. However, we succeeded in determining the source locations that are close to the results of the moment tensor inversion and clearly different from the previous studies (e.g., Chouet et al., 2003, 2008; Marchetti and Ripepe, 2005) by the semblance analysis.

3.3.2 Model resolution matrices

To investigate how well the model parameters can be resolved in the inverse problem, we calculate a model resolution matrix (Menke, 1984; Stein and Wysession, 2003). Firstly, we assume that the model parameter vector $\boldsymbol{m}$ is true but unknown to explain the observation data $\mathbf{d}^{\mathrm{obs}}$

$$\mathbf{d}^{\mathrm{obs}} = \mathbf{G}\mathbf{m}^{\mathrm{true}}. \tag{3.14}$$

Here, $\mathbf{G}$ is the data kernel corresponding to the Green's functions computed from a point source and $\mathbf{m}^{\mathrm{true}}$ is the vector of the moment tensors. The estimated model $\mathbf{m}^{\mathrm{est}}$ is given by using the generalized inverse of $\mathbf{G}$ and equation (3.14) as

$$\mathbf{m}^{\mathrm{est}} = \mathbf{G}^{-\mathrm{g}}\mathbf{d}^{\mathrm{obs}} = \mathbf{G}^{-\mathrm{g}}[\mathbf{G}\mathbf{m}^{\mathrm{true}}] = [\mathbf{G}^{-\mathrm{g}}\mathbf{G}]\mathbf{m}^{\mathrm{true}} = \mathbf{R}\mathbf{m}^{\mathrm{true}}, \tag{3.15}$$

where the symbol $-\mathrm{g}$ represents the generalized inverse and $\mathbf{R}$ is the model resolution matrix. The estimated model parameters are the weighted average of the true model parameters. The diagonal values of the model resolution matrix simply indicate how well the model parameters can be solved. If $\mathbf{R} = \mathbf{I}$, each model parameter is perfectly solved.

Based on the singular-value decomposition (SVD), an $n \times r$ data kernel $\mathbf{G}$ is decomposed as

$$\mathbf{G} = \mathbf{U}\boldsymbol{\Lambda}\mathbf{V}^{\mathrm{T}}, \tag{3.16}$$

where $\mathbf{U}$ is an $n \times n$ unitary matrix, $\boldsymbol{\Lambda}$ is an $n \times r$ rectangular diagonal matrix, $\mathbf{V}$ is an $r \times r$ unitary matrix and the symbol $^{\mathrm{T}}$ indicates the transpose. The diagonal elements of $\boldsymbol{\Lambda}$ are

nonnegative singular values. If $\mathbf{G}^{-\mathrm{g}}\mathbf{G}$ is singular since at least one eigenvalue of this symmetric matrix is zero, the diagonal elements of $\mathbf{\Lambda}$ are composed of $p\ (<r)$ nonzero eigenvalues. This $p \times p$ matrix $\mathbf{\Lambda}_p$ enables to decompose the data kernel $\mathbf{G}$ by using only the eigenvectors associated with nonzero eigenvalues,

$$\mathbf{G} = \mathbf{U}\mathbf{\Lambda}\mathbf{V}^{\mathrm{T}} = \mathbf{U}_p\mathbf{\Lambda}_p\mathbf{V}_p^{\mathrm{T}}, \tag{3.17}$$

where $\mathbf{U}_p$ is the $n \times (n-p)$ matrix divided from the matrix $\mathbf{U}$ by using the eigenvectors with nonzero eigenvalues and $\mathbf{V}_p$ is the $r \times (r-p)$ matrix divided from the matrix $\mathbf{V}$. In this case, the generalized inverse can be written as

$$\mathbf{G}^{-\mathrm{g}} = \mathbf{V}_p\mathbf{\Lambda}_p^{-1}\mathbf{U}_p^{\mathrm{T}}. \tag{3.18}$$

Then, the model resolution matrix $\mathbf{R}$ yields

$$\mathbf{R} = \mathbf{G}^{-\mathrm{g}}\mathbf{G} = \mathbf{V}_p\mathbf{\Lambda}_p^{-1}\mathbf{U}_p^{\mathrm{T}}\,\mathbf{U}_p\mathbf{\Lambda}_p\mathbf{V}_p^{\mathrm{T}} = \mathbf{V}_p\mathbf{V}_p^{\mathrm{T}}. \tag{3.19}$$

The Green's functions are convolved with the cosine function expressed as equation (3.9) with $t_r = 5$ s. This rising time describes the dominant period of VLP seismograms in our analyses (0.05-0.2 Hz). Figure 3.13 (a) shows the distribution of normalized eigenvalues obtained from the SVD of the data kernel $\mathbf{G}$ computed from the point sources of location (i), location (ii) and 100 m below location (i). We select the point source of 100 m below location (i) because the depth is consistent with the result of VLP source location determined by some previous studies (e.g., Chouet et al., 2003, 2008; Marchetti and Ripepe, 2005) and in order to examine the depth dependence of the resolution. The distribution shows that the sixth eigenvalues are sufficiently small for all source locations, especially location (i) and (ii). These eigenvalues are 0.69 %, 0.23 %, and 1.37 % of overall contribution, respectively. Here, we place the eigenvalues less than 1.0 % of overall contribution with zero to consider the pseudoinverse problem in equations (3.17), (3.18) and (3.19). Figures 3.13 (b), (c) and (d) show the model resolution matrices calculated by using the eigenvalues exceeding the threshold. The results of location (i) and (ii) show that the resolution of the diagonal components of the moment tensors (M_{xx}, M_{yy}, and M_{zz}) are lower than the deviatoric ones. There are large trade-offs between one diagonal moment tensor and the other two diagonal ones. These

results suggest that the diagonal components of the source mechanisms are not very well constrained even by using our very-near-field seismic network. However, the well-constrained deviatoric components indicate the dominance of the diagonal components in the source mechanisms. The model resolution matrix for the source 100 m below location (i) shows the model parameters is completely solved under the condition with a threshold of 1.0 % of overall contribution. Although the physical meaning of 1.0% is not clear but may be related to a signal to noise ratio, this result suggests that the source mechanism solution for a deeper event is likely to be more accurately obtained than a shallower event. This is consistent with the results of synthetic tests of moment tensor inversion for different source location and network configuration conducted by Lanza and Waite (2018).

3.3.3 Examination of source location resolution based on synthetic tests of network performance

We investigate how well the accuracy of source location has been relatively improved by the very-near-field condition compared to the distant seismic network used in other previous studies. Figure 3.14 (a) shows the location of our temporary seismic stations in 2016 and synthetic stations. These 18 synthetic stations are located at 500 m and 1000 m away from the C crater, and the shape and distance are configured to resemble to the network of the previous study by Chouet et al. (2003). Figures 3.14 (b) and (c) indicate the model resolution matrices for the seismic stations in 2016 and the 18 synthetic stations when the source location is set at location (i) obtained. The comparison shows that the resolution for the distant network with a large number of stations is not significantly improved.

We next perform moment tensor inversion for synthetic source mechanisms. We assume three source models, isotropic expansion/contraction with moment tensor ratios of 1:1:1, a crack with N45 °E striking opening/closing to NW-SE direction where the strike is parallel to the long axis of the crater terrace, and a crack opening/closing to vertical direction at 600 m a.s.l., which is similar to our source mechanism solutions. We also assume a Poisson ratio $\nu = 1/2$ so that the principal axes for the both crack models have amplitude ratios of 3:1:1 in descending order. We compute the Green's functions at each station and convolve with an observed waveform at UD component of ST1 at 0.05-0.2 Hz frequency band as a source time function. We also add white noises that are calculated using the root mean squared of the amplitude of this source time function. By using the synthetic waveforms, we conduct moment tensor inversion and calculate the variance reduction

(VR) of waveforms derived from $\mathrm{VR} = 1 - E_1$.

We compare the source region within 90 % of the maximum of VR value between the seismic stations in 2016 and the 18 synthetic stations. Figures 3.15 (a), (b) and (c) compare the regions within 90 % of the maximum VR values for an isotropic source, a N45 °E striking crack, and a sill crack, respectively. We note that the optimal source locations illustrating the maximum VR value are determined at the input locations in the all source models with the all network configurations. Table 3.1 summarizes the number of source grids within 90 % of the maximum VR values. The comparison shows that the number of source grids for the seismic stations in 2016 is significantly smaller than that for the distant synthetic stations. This suggests that the source location is more exactly determined by using the very-near-field data.

3.3.4 Synthetic tests for finite source models

Waveform inversion of VLP signals is usually conducted based on the conception of a point source approximation (Aki and Richards, 1980). In this study, assuming a V_p of 3.5 km/s, whose wavelength (λ) of VLP at 0.05-0.2 Hz is 17.5-70 km, the distance (r) from the source to stations of 0.1-0.7 km, and the magma reservoir extending for about 0.3 km (L) which is consistent with the long axis of the crater area, the point source approximation $L^2 \ll r\lambda/2$ could be satisfied in theory. However, the distance (r) is relatively small compared to the assumed source size so that the near-field effects or the radiation patterns by a finite source should be considered in the condition of the very-near-field observation.

Here, we have synthetic tests for finite source modelling. In the synthetic tests, we first compute synthetic waveforms by adding the Green's functions from the several point sources for two models: a crack with N45 °E striking and with 3×3 source grids opening/closing to NW-SE direction, and a crack opening/closing to vertical direction at 600 m a.s.l. with 3×3 source grids (Figures 3.16 (a) and (c)). Here, we assume that the all point sources move simultaneously. We convolve the synthetic waveforms with an observed waveform at ST1 (UD component) at 0.05-0.2 Hz frequency band as a source time function. We also add white noise that is calculated by using the root mean squared amplitude of this source time function.

The source recovery result shows that the optimal source location is determined at the centroid of the source region in the case of the crack with N45 °E striking, which is illustrated by a white square (Figure 3.16 (a)). In the case of the sill crack, the optimal source is determined at a location only 50 m (1 grid) below the centroid of the crack. These results suggest that there is little problem

in the very-near-field condition for constraining the centroid of VLP source even for finite size of sources. Figures 3.16 (b) and (d) compare the eigenvectors obtained from the maximum amplitudes in the moment tensor components between the source models and the solutions. We note that the magnitudes of the eigenvectors are normalized by the maximum ones to be 3.0 so that we mainly discuss the fitting of the direction of the eigenvectors. The results show that the eigenvectors between input models and output solutions are not so well matched. These comparisons suggest that the source mechanisms in the finite sources may not be well constrained by the very-near-field condition. Particularly, the misfit for the N45° E striking crack model is much larger than the sill crack model. This also suggests that not only the network configuration but also the source type or the geometry of the retrieved mechanism may disable us to constrain the source mechanism by moment tensor inversion (Lanza and Waite, 2018).

These synthetic tests are also conducted for the synthetic network configured by 18 stations (Figure 3.14 (a)). Figure 3.17 shows the recovery of the source locations and mechanisms for the synthetic network. The source location recovery results (Figures 3.17 (a) and (c)) show that the optimal source locations are estimated to the centroid of the source regions in both source models. However, the error (E_1) distribution implies that the centroids are not well constrained compared with the results in Figures 3.16 (a) and (c). The source mechanism recovery results (Figures 3.17 (b) and (d)) suggest that the distant network is more appropriate to constrain the source mechanism than the very-near-field network. The combination of very-near-field and distant network will enable us to obtain both optimal source location and mechanism of eruption earthquakes.

3.3.5 Single force source

Several previous studies of moment tensor inversion of explosion earthquakes include the single forces (e.g., Ohminato et al., 1998, 2006; Chouet et al., 2003; Waite et al., 2008). The vertical single force (F_z) has often been observed in the source mechanism solutions and this has been interpreted as a reaction force by ejection of magma or gas in the conduit (Kanamori et al., 1984). It has been theoretically shown that a single force is generated according to the advection of materials in magma or hydrothermal system (Takei and Kumazawa, 1994). However, the single force components that are resolved at the same time as the moment tensor components are sometimes interpreted as spurious ones due to a mislocated source location, mismodeling of velocity structures, or low signal-to-noise ratio of signals (Davi et al., 2010; De Barros et al., 2013; Trovato et al., 2016).

We perform moment tensor inversion including the single forces for the 103 VLP events to

compare the solutions of moment tensor inversion between six components and nine components including three single forces and six moment tensors. The observed seismogram generated by a moment tensor and a single force is described in the frequency domain as

$$U_n^{\mathrm{obs}}(\omega) = F_p(\omega)G_{np}(\omega) + M_{pq}(\omega)G_{np,q}(\omega), \tag{3.20}$$

where $F_p(\omega)$ is the p-th direction single force. The matrix form can be written as the same one as equation (3.7), but the dimension of the matrix G becomes the number of traces $\times$ 9 and the source mechanism vector that consists of six moment tensors and three single forces. The Green's functions for the single forces are computed by the software of OpenSWPC (Maeda et al., 2017).

Figure 3.18 shows the result of the distribution of optimal VLP (0.05-0.2 Hz) source locations. The number of events for each source grid is indicated by the different size and color of a hexagon or a gray circle. We have labeled the top two clusters as location (viii) (60 events) and location (ix) (27 events) based on only the difference in the locations. The result shows that the locations shift to north direction in 150-200 m compared with the locations determined by using only 6 moment tensors. Figure 3.19 shows the stacked solutions of the single force components and moment tensor components. The results show that the three diagonal moment tensor components and the north-south direction of single force (F_x) are dominant. Figure 3.20 shows the waveform fitting between the observation and synthetics for the two events in location (viii) and location (ix), respectively. The residuals of waveforms (E_1) are improved to 7.3 % and 7.1 %. The mean value of E_1 for 103 events is 7.8 %. We examine the contribution of single forces and moment tensors to the synthetic waveforms. The green dashed lines in Figure 3.20 are the synthetic waveforms calculated from the moment tensors, and the blue dashed lines are calculated from the single forces. The comparison suggests that the horizontal single force (F_x, x: north) mainly contributes to improve the waveform fitting on the NS component of waveforms.

If we forcibly interpret this single force, a plausible physical mechanism is that the single force may act as a reaction force for the southward movement of magma or gas toward the region below the crater. We examine how well the observed single force can explain the physical processes in the conduit. The strength of the force F due to viscous liquid flow in a cylindrical conduit is given as $F = 8\pi\eta\nu l$, where η is the fluid viscosity, ν is the mean fluid velocity, and l is the length of the conduit wall (e.g., Turcotte and Schubert, 2001; Ohminato et al., 2006). Using F of 9.0×10^7 N, which is the mean value of F_x in the 103 VLP events, magma viscosity η of 10^4 Pa・s (Métrich

et al., 2001) and the conduit length l of 250 m, which is the distance from location (viii) to the crater is directly elongated, we obtain the mean fluid velocity of 1.4 m/s. The ascending time of the fluid from the VLP source to the crater is calculated to 178.6 s. However, the main VLP phase starts about 5 s before an explosion so that the ascending time is too slow to explain the temporal evolution from the origin of VLP signals to an explosion.

The model resolution matrices including three single force components and six moment tensor components at source location (viii) are computed (Figures 3.21 (a), (b) and (c)). The amplitudes of the single forces and the moment tensors estimated by moment tensor inversion are generally different with the ratios (M_{pq}/F_p) of 10^3-10^5 (e.g., Ohminato et al., 1998; Chouet et al., 2003; Waite et al., 2008). Our results in Figures 3.19 (a) and (b) also show that the ratios (M_{pq}/F_p) are around 10^3-10^5. This affects the eigenvalues in SVD computation in equation (3.16)-(3.19). Thus, we change the amplitude weight of the Green's functions in the single forces as $F_p/1000$, $F_p/10000$, and $F_p/100000$ in the data kernel to compute the model resolution matrices. The results show that the model parameters cannot be completely solved under the condition that the threshold is 1.0 % of overall contribution.

Due to the difficulty in interpreting the temporal evolution of seismic and acoustic signals such shown in Figure 2.2, smaller amplitude of the vertical single force (F_z) in the solutions, and lower resolution of the model parameters even including the single forces, we are not able to discuss the source mechanism including the single forces.

3.4 Summary

We have conducted seismic moment tensor inversion including tilt responses using temporary very-near-field network data at Stromboli volcano. Most of the VLP (0.05-0.2 Hz) seismic sources associated with small explosions are located at the edge of the crater rim, which are about 200 m away from the eruptive (NE) crater at 600 m or 650 m a.s.l. These two clusters may indicate the difference in the source mechanisms during/after explosions. The source mechanisms show the dominance of the vertical dipole component of the moment tensor, but the model resolution matrices calculated from the Green's functions indicate lower resolutions of three diagonal moment tensors than the deviatoric ones. The seismic sources at 0.2-0.5 Hz (higher frequency part of the VLP band) and 0.5-1.0 Hz (LP) are located closer to NE crater than the sources at 0.05-0.2 Hz. These VLP and LP earthquakes may be almost simultaneously excited from different centroids. Synthetic tests of network performance show that the distant seismic network does not necessarily contribute to the

improvement of the mechanism solutions. Furthermore, the very-near-field network contributes to exactly determine the source locations compared to the synthetic seismic network configured by 18 stations. Synthetic tests of finite source modelling support the reliability of the source locations determined by our very-near-field network data and inaccuracy of the source mechanisms.

Table 3.1 Number of source grids within 90 % of the maximum variance reduction (VR) of waveforms obtained by moment tensor inversion. These regions are illustrated in Figure 3.15.

	Isotropic	N45°E crack	Sill
Seismic stations in 2016	56	48	51
18 synthetic stations	123	108	97

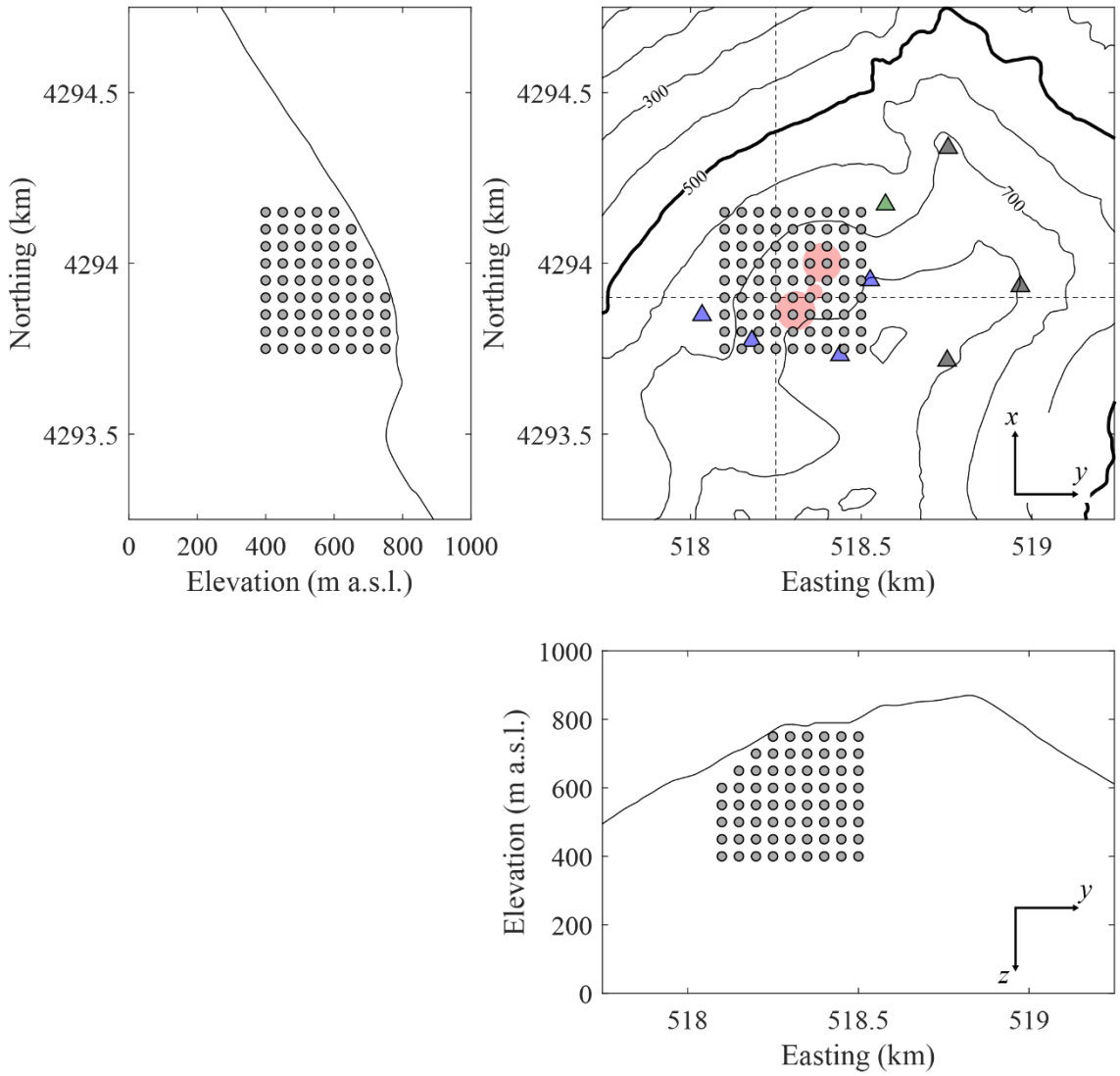

Figure 3.1 Point source distribution for computing the Green's functions. The point sources are embedded with intervals of 50 m in east-west (y), north-south (x) and up-down (z) directions. Total number of the point sources is 543. Dashed lines in the horizontal section indicate the positions of the cross sections. The main craters are represented by the red circles in the horizontal section. The blue, green and black triangles indicate temporary seismic and acoustic, temporary seismic, and permanent seismic and acoustic stations, respectively.

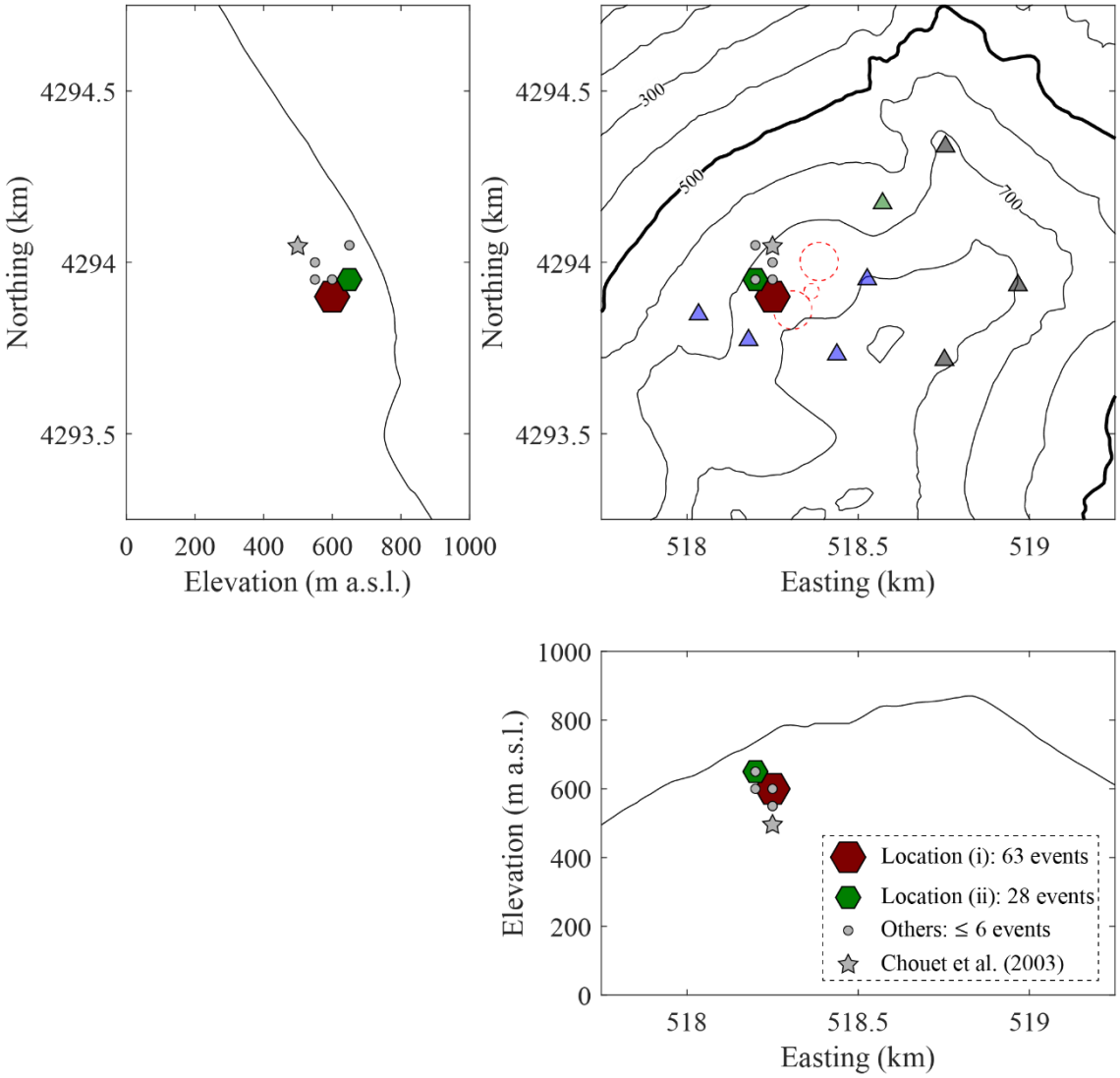

Figure 3.2 Source distribution of 103 seismic events at 0.05-0.2 Hz determined by moment tensor inversion. The brown hexagon shows the location of 63 events (location (i)). The green hexagon shows the location of 28 events (location (ii)). The gray circles show the location of other events and each cluster include less than 6 events. The gray star illustrates the location of VLP source determined by moment tensor inversion by Chouet et al. (2003).

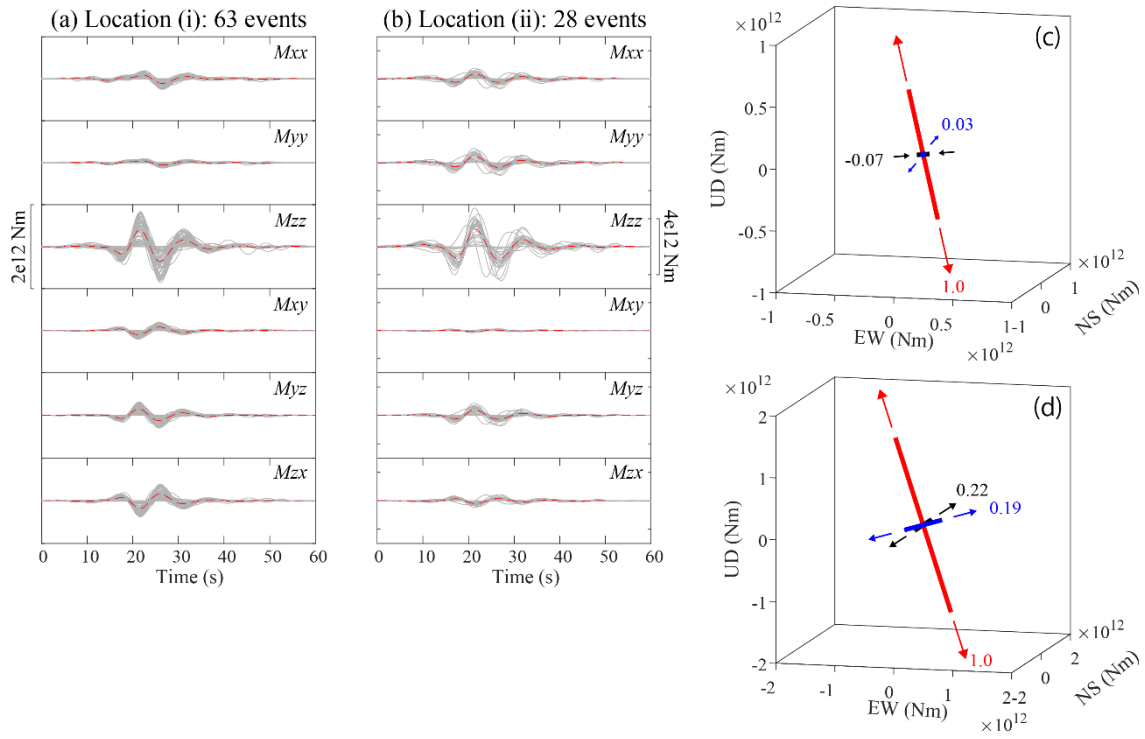

Figure 3.3 (a) Stacking of the moment tensor solutions for the events in location (i). The red dashed lines illustrate the average lines of the stacking moment tensor solutions. Note that the x and y directions are set to be NS and EW, respectively, and the z direction is vertical one. (b) Similar to Figure 3.3 (a) for the events in location (ii). (c) Plot of eigenvectors for the "average" moment tensor solution shown in Figure 3.3 (a). The values indicate the ratios of the principal axes. (d) Similar to Figure 3.3 (c) for the "average" moment tensor solution shown in Figure 3.3 (b).

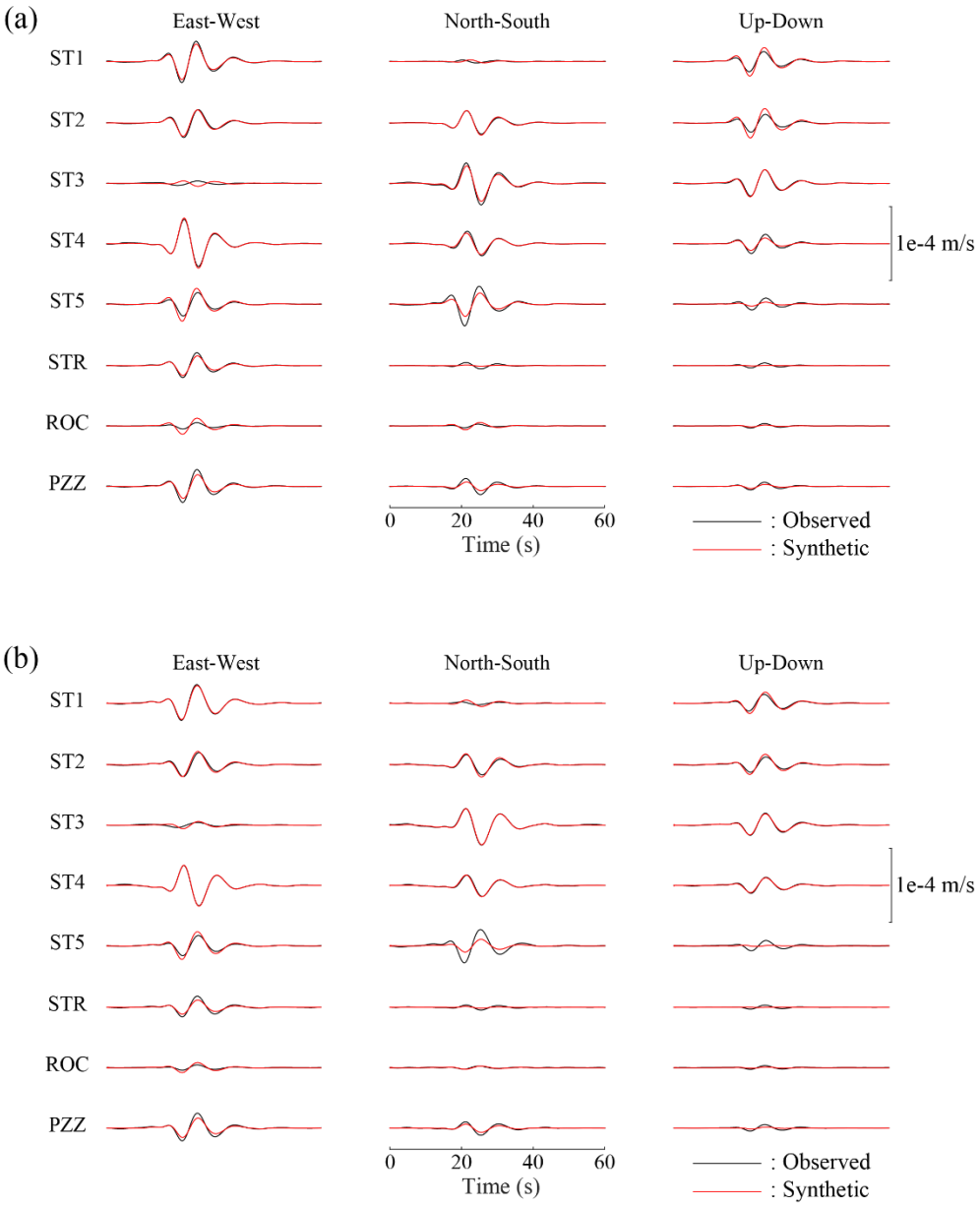

Figure 3.4 (a) Waveform fitting for an event in location (i). The observed seismograms are represented by black lines and synthetic waveforms for the inversion results are represented by red lines. The residual of waveforms calculated by equation (3.10) is 10.0 %. (b) Similar to Figure 3.4 (a) for an event in location (ii). The residual of waveforms is 10.2 %.

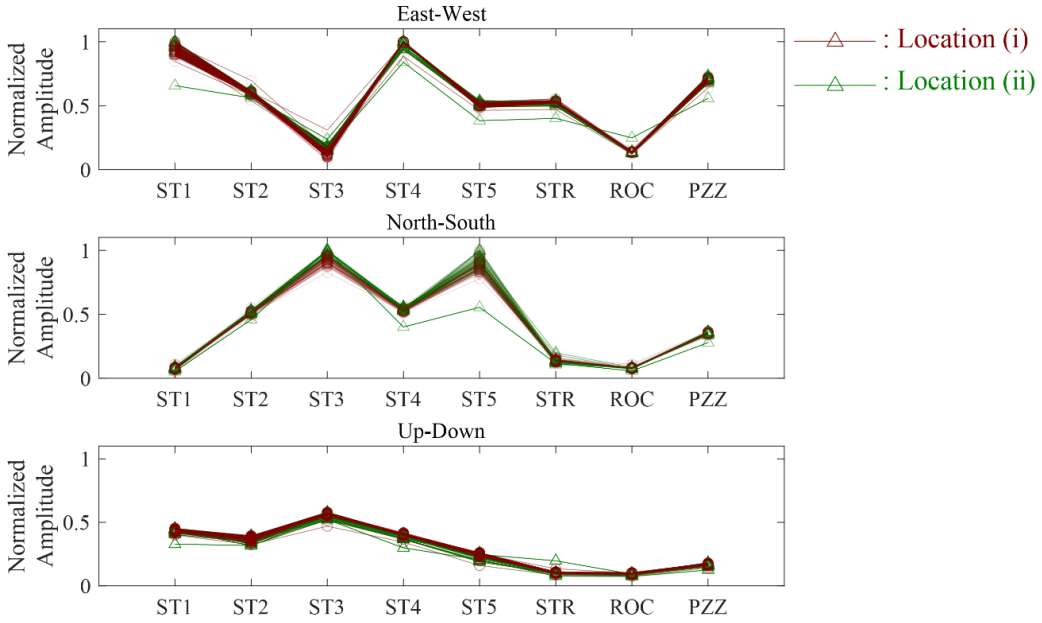

Figure 3.5 Distribution of normalized root-mean-square amplitudes (0.05-0.2 Hz) for all events in location (i) (brown lines with triangles) and (ii) (green lines with triangles).

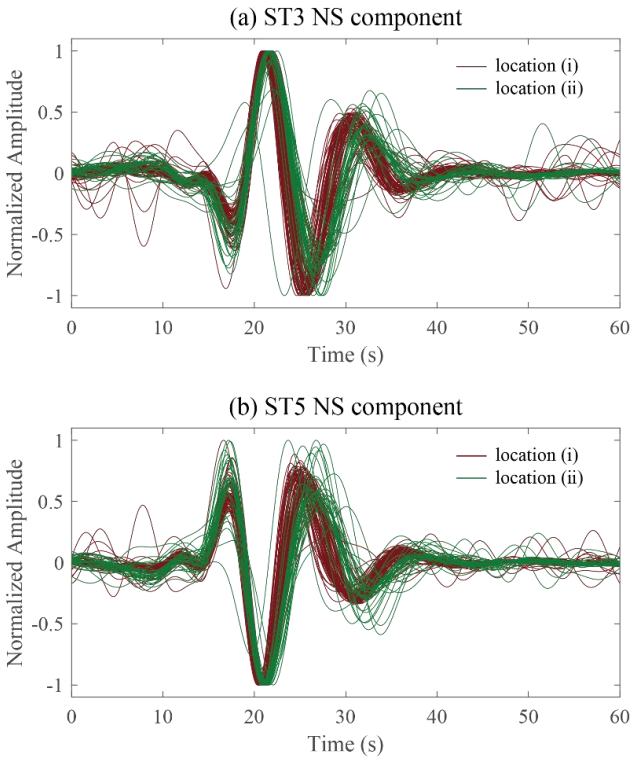

Figure 3.6 (a) Normalized waveforms at 0.05-0.2 Hz for all events in location (i) (brown lines) and (ii) (green lines) at NS component of ST3. (b) Similar to Figure 3.6 (a) for NS component of ST5.

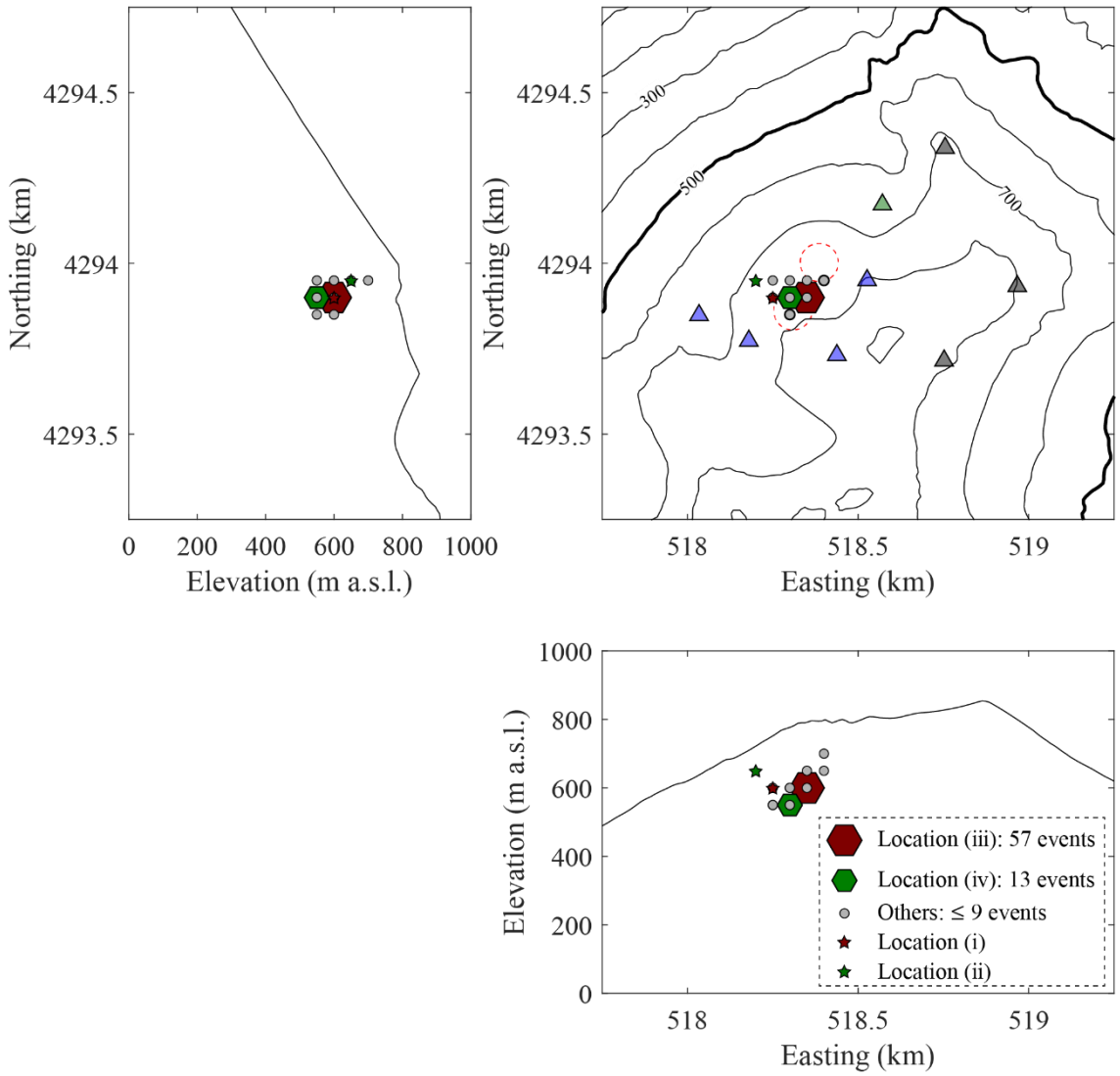

Figure 3.7 Source distribution of 103 seismic events at 0.2-0.5 Hz determined by moment tensor inversion. The brown hexagon shows the location of 57 events (location (iii)). The green hexagon shows the location of 13 events (location (iv)). The gray circles show the location of other events and each cluster include less than 9 events.

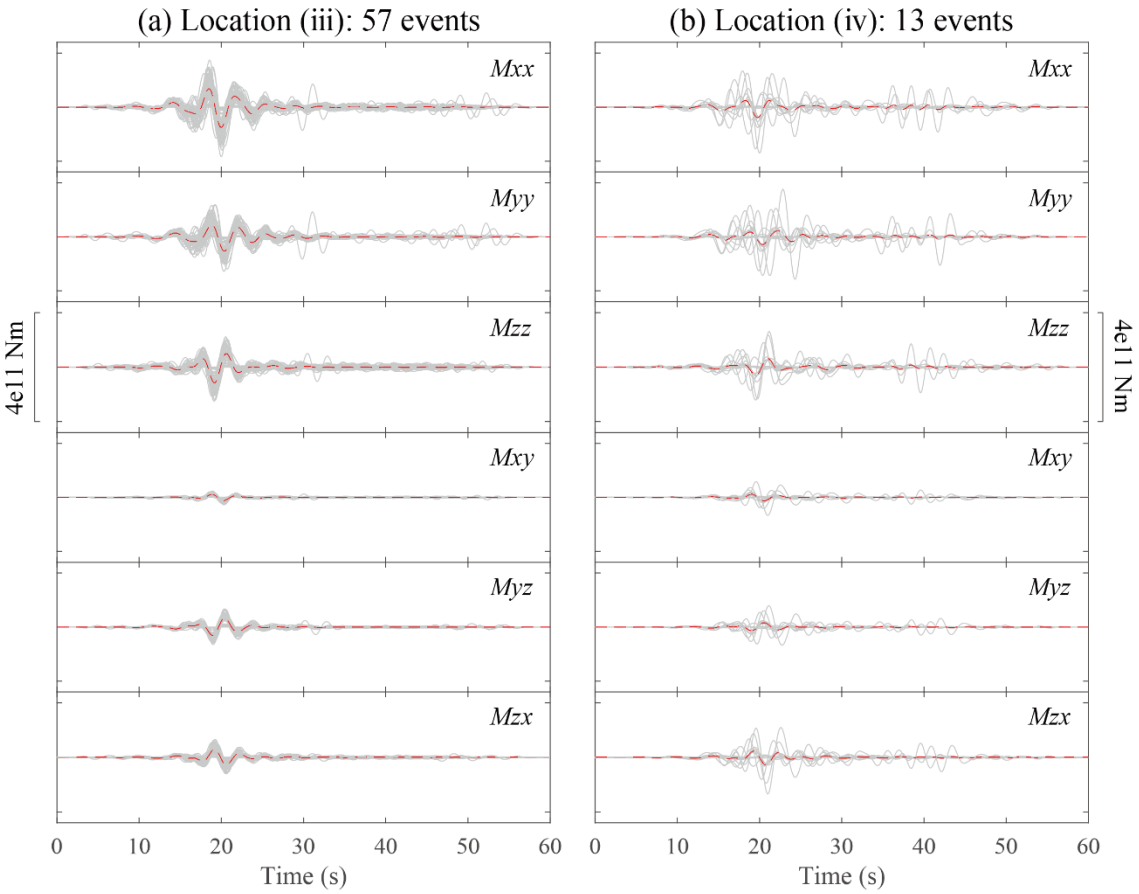

Figure 3.8 (a) Stacking of the moment tensor solutions for the events in location (iii). The red dashed lines illustrate the average lines of the stacking moment tensor solutions. (b) Similar to Figure 3.8 (a) for the events in location (iv).

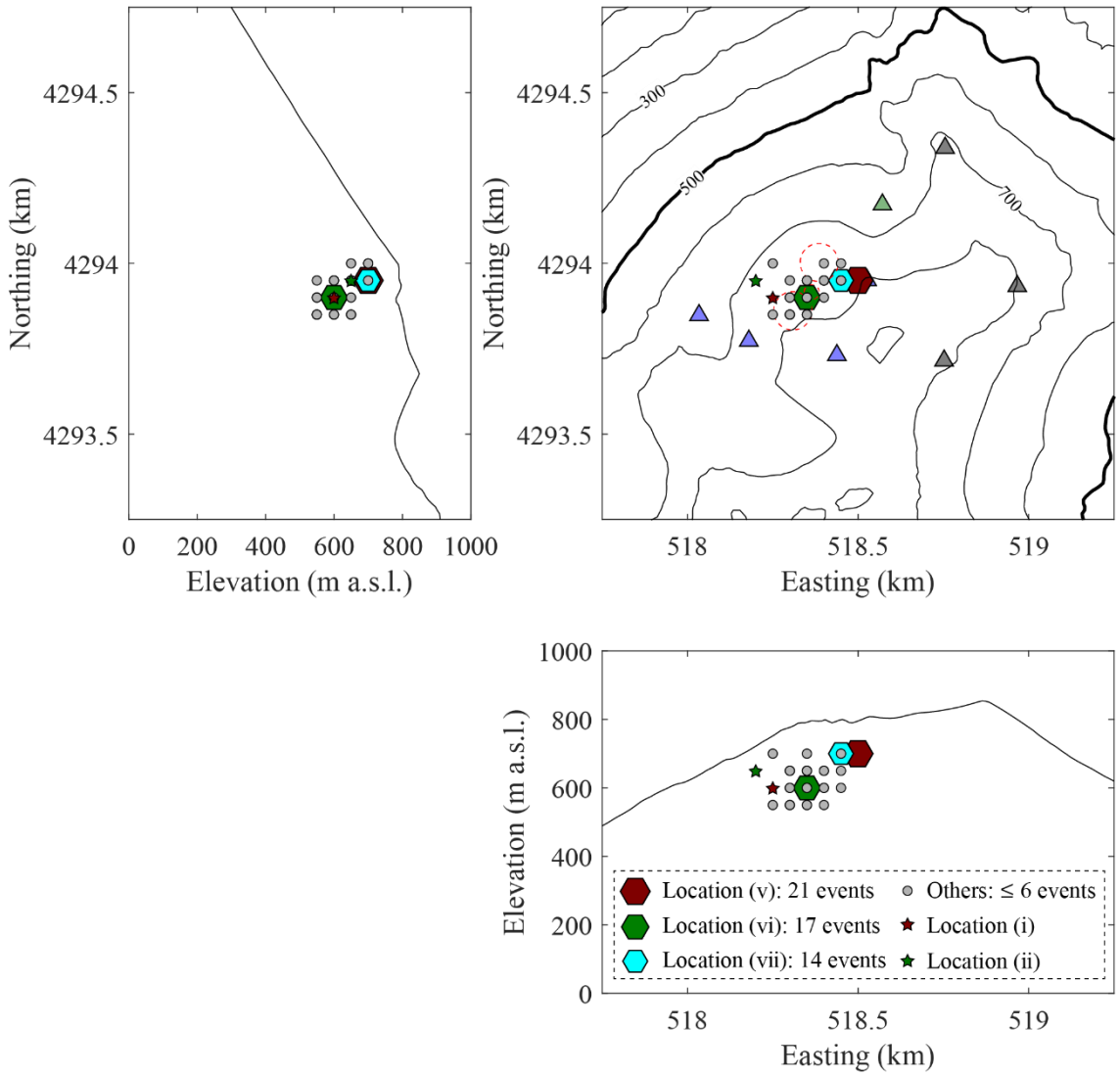

Figure 3.9 Source distribution of 103 seismic events at 0.5-1.0 Hz determined by moment tensor inversion. The brown hexagon shows the location of 21 events (location (v)). The green hexagon shows the location of 17 events (location (vi)). The blue hexagon shows the location of 14 events (location (vii)). The gray circles show the location of other events and each cluster include less than 6 events.

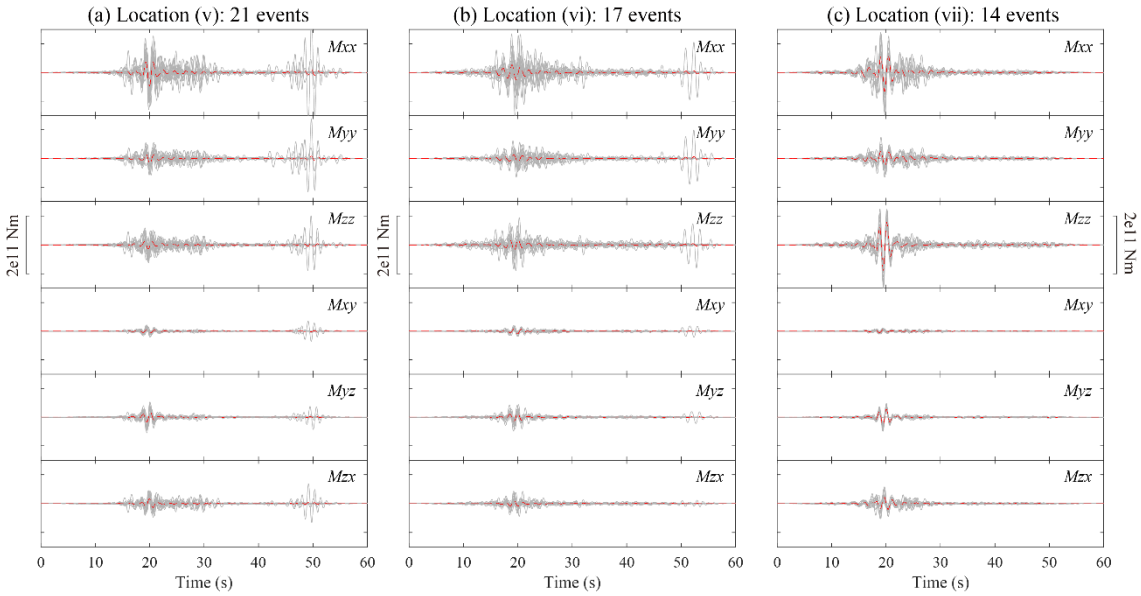

Figure 3.10 (a) Stacking of the moment tensor solutions for the events in location (v). The red dashed lines illustrate the average lines of the stacking moment tensor solutions. (b), (c) Similar to Figure 3.10 (a) for the events in location (vi) and (vii).

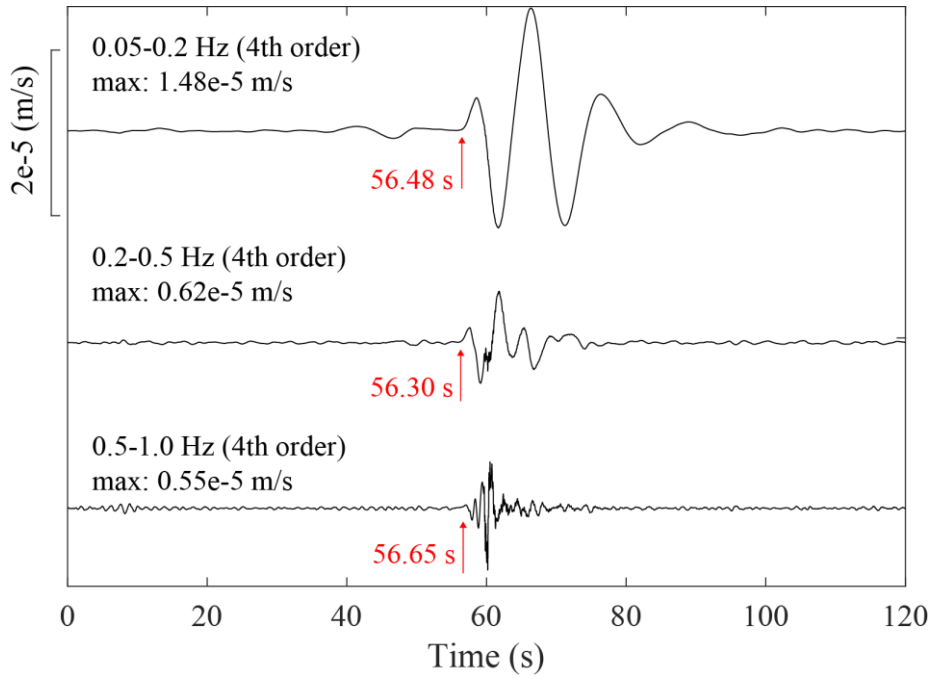

Figure 3.11 Comparison of waveforms in different frequency bands, 0.05-0.2 Hz, 0.2-0.5 Hz, and 0.5-1.0 Hz, using causal band-pass filters. The arrival times shown by red arrows are manually obtained.

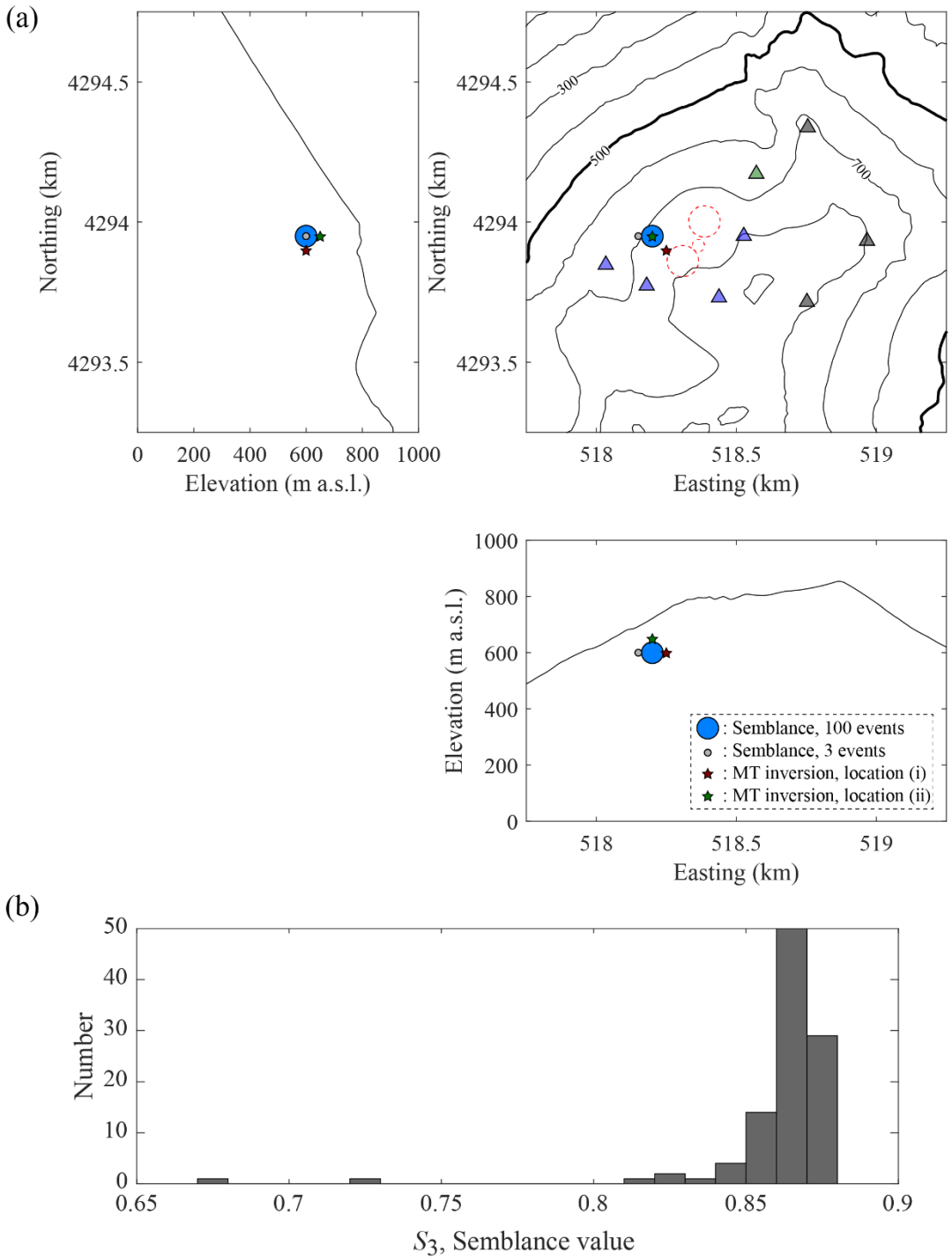

Figure 3.12 (a) Source distribution of 103 VLP (0.05-0.2 Hz) seismic events determined by the semblance analysis and comparison with moment tensor inversion. The methods and number of events are listed in EW cross section. (b) Histogram of the semblance values for 103 VLP events.

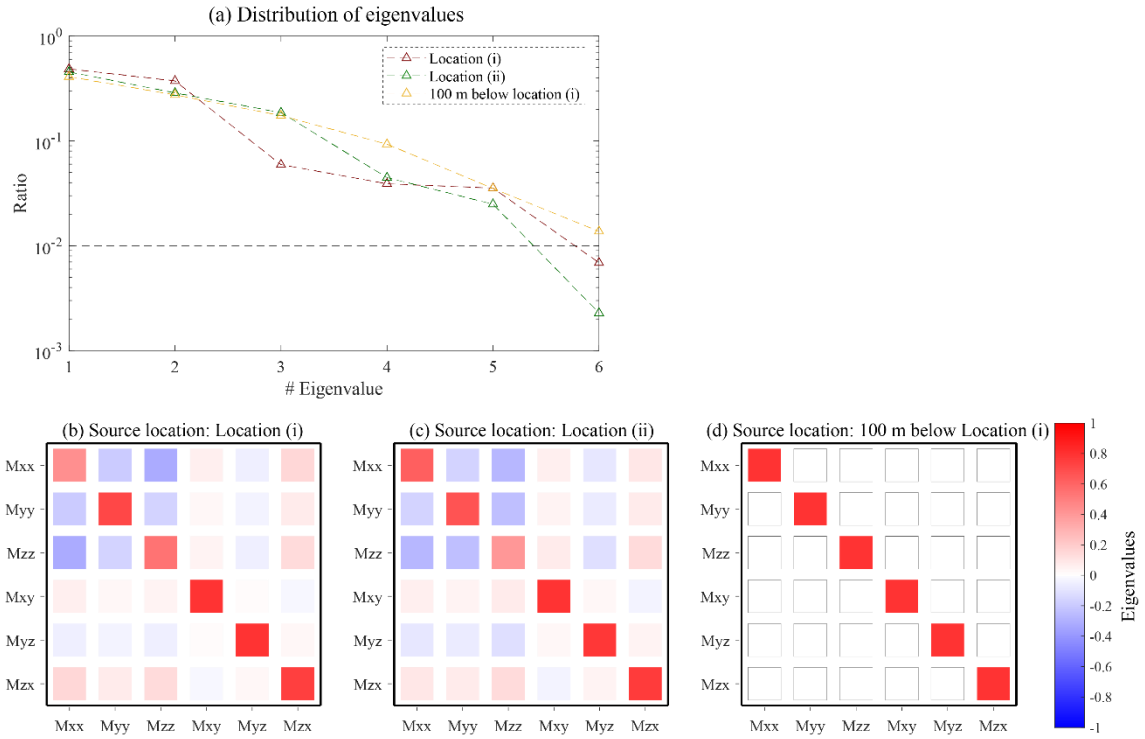

Figure 3.13 (a) Distribution of eigenvalues obtained by the SVD of the data kernel. The colors indicate the different point sources. The black dashed line shows 1.0 % of the overall contribution of the model parameters to the solution and threshold for considering the pseudoinverse problem. (b) Model resolution matrix for source location (i). A color scale indicates the value of the diagonal component in the matrix. (c) Model resolution matrix for source location (ii). (d) Model resolution matrix for the source 100 m below location (i).

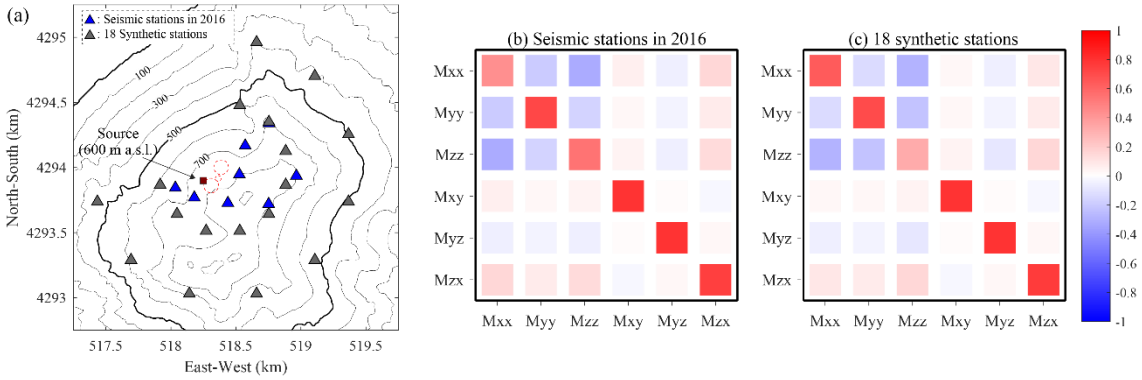

Figure 3.14 (a) Location of seismic stations. Blue triangles show the temporary seismic network in 2016. Black triangles show the synthetic network configured by 18 stations. The brown square indicates the source location determined by moment tensor inversion (location (i)) for computing the Green's functions. The red dashed circles are the locations of the craters. (b) Model resolution matrix computed by using the seismic stations in 2016. (c) Model resolution matrix computed by using the 18 synthetic seismic stations. A color scale indicates the value of the diagonal component in the matrix

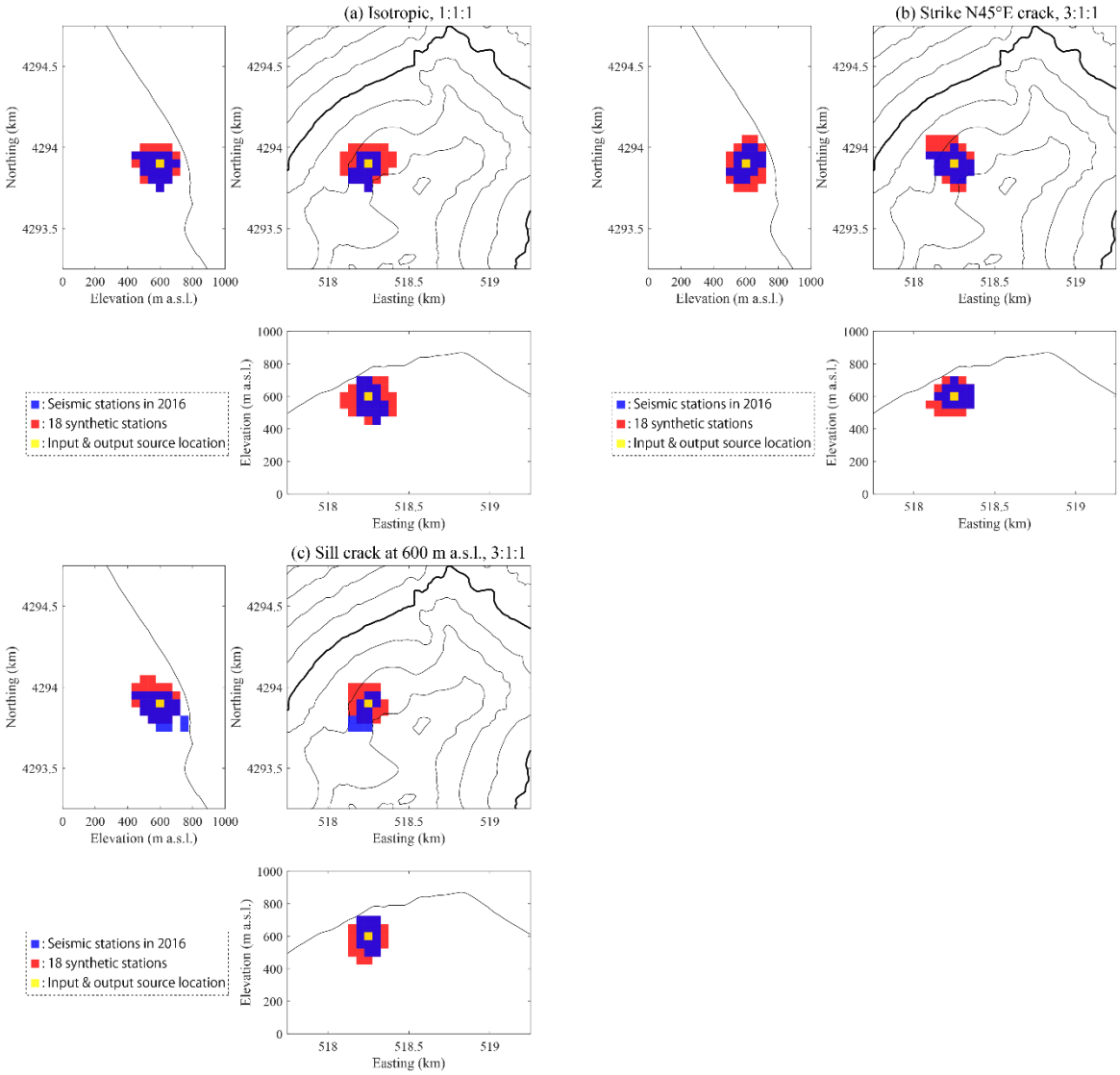

Figure 3.15 (a) Comparison of the regions within 90 % of the maximum VR values between the seismic stations in 2016 (blue squares) and the 18 synthetic stations (red squares) for an isotropic source. The yellow squares indicate the source location which shows the maximum VR values. (b), (c) Similar to Figure 3.15 (a) for a N45°E crack source and a sill crack source.

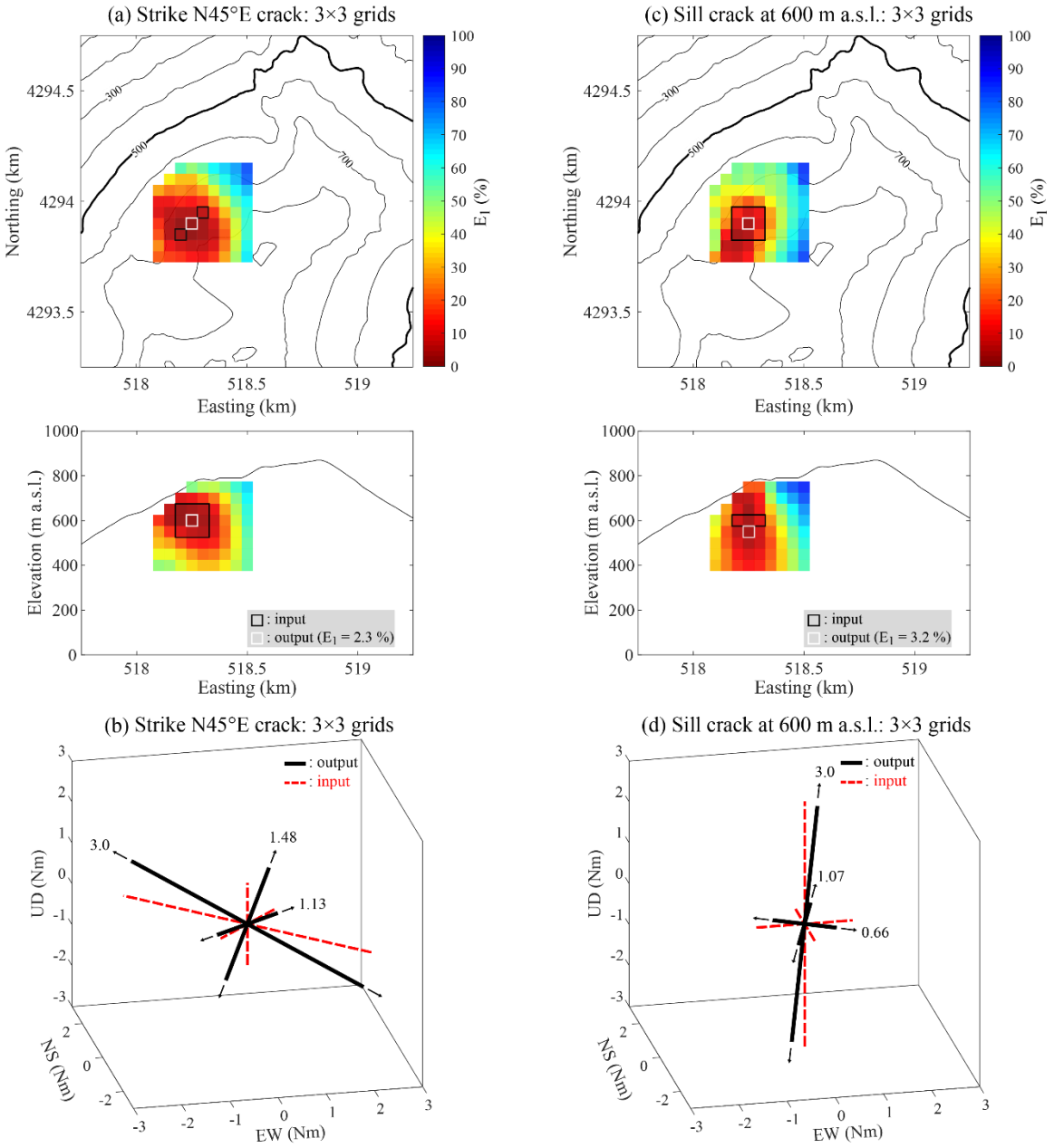

Figure 3.16 (a) Comparison of the source location between input finite source model (black squares) and the output solution (white square) in the case of a N45 °E striking crack for the temporary network in 2016. A color scale illustrates the error value of waveforms (E_1). (b) Comparison of the source mechanism expressed by eigenvectors of moment tensors between input finite source model (red dashed lines) and output solution (black lines). The values are normalized eigenvalues of the vectors. (c), (d) Similar to Figures 3.16 (a) and (b) for a sill crack at 600 m a.s.l.

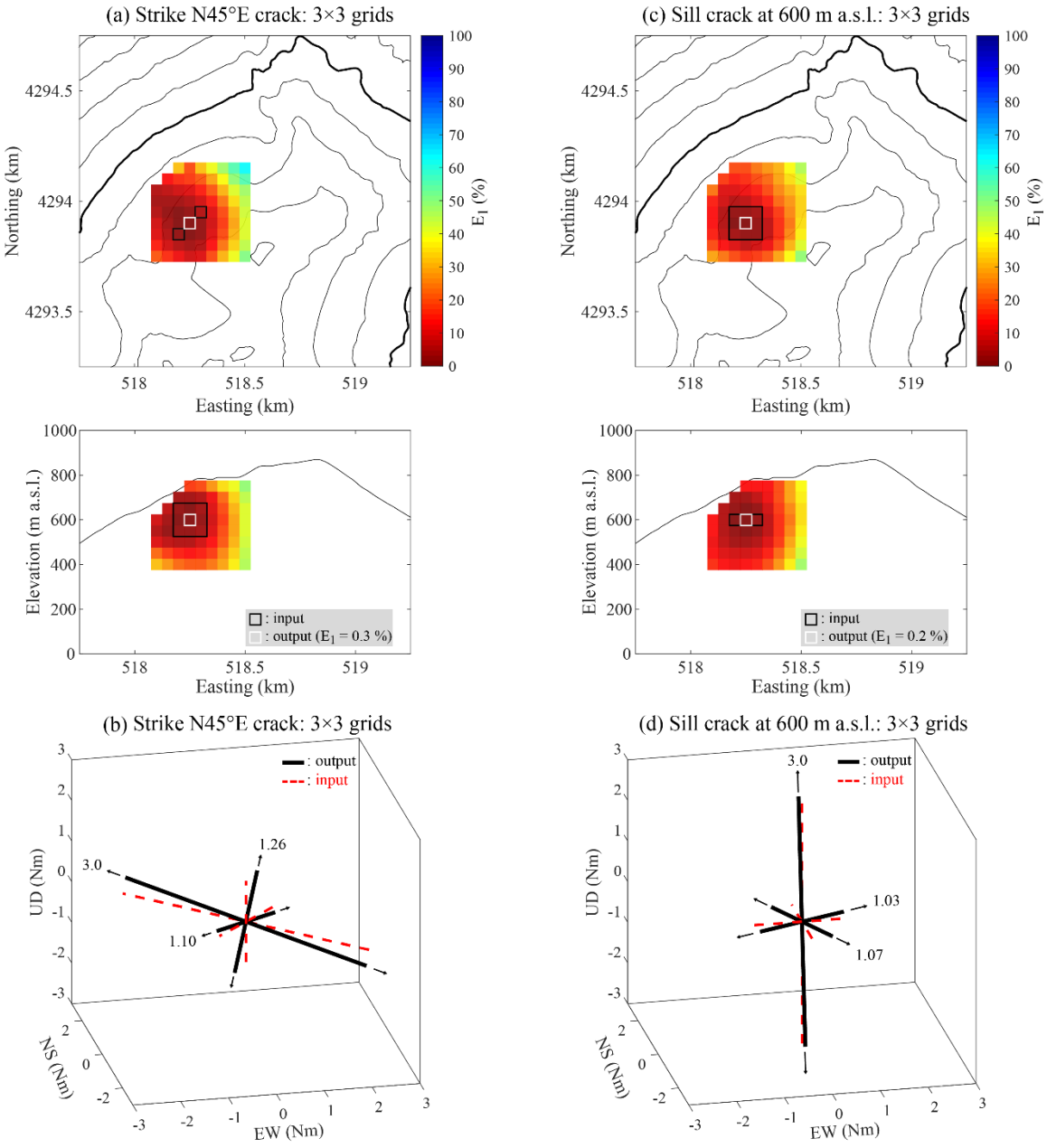

Figure 3.17 Similar to Figure 3.16 for the synthetic network configured by 18 stations.

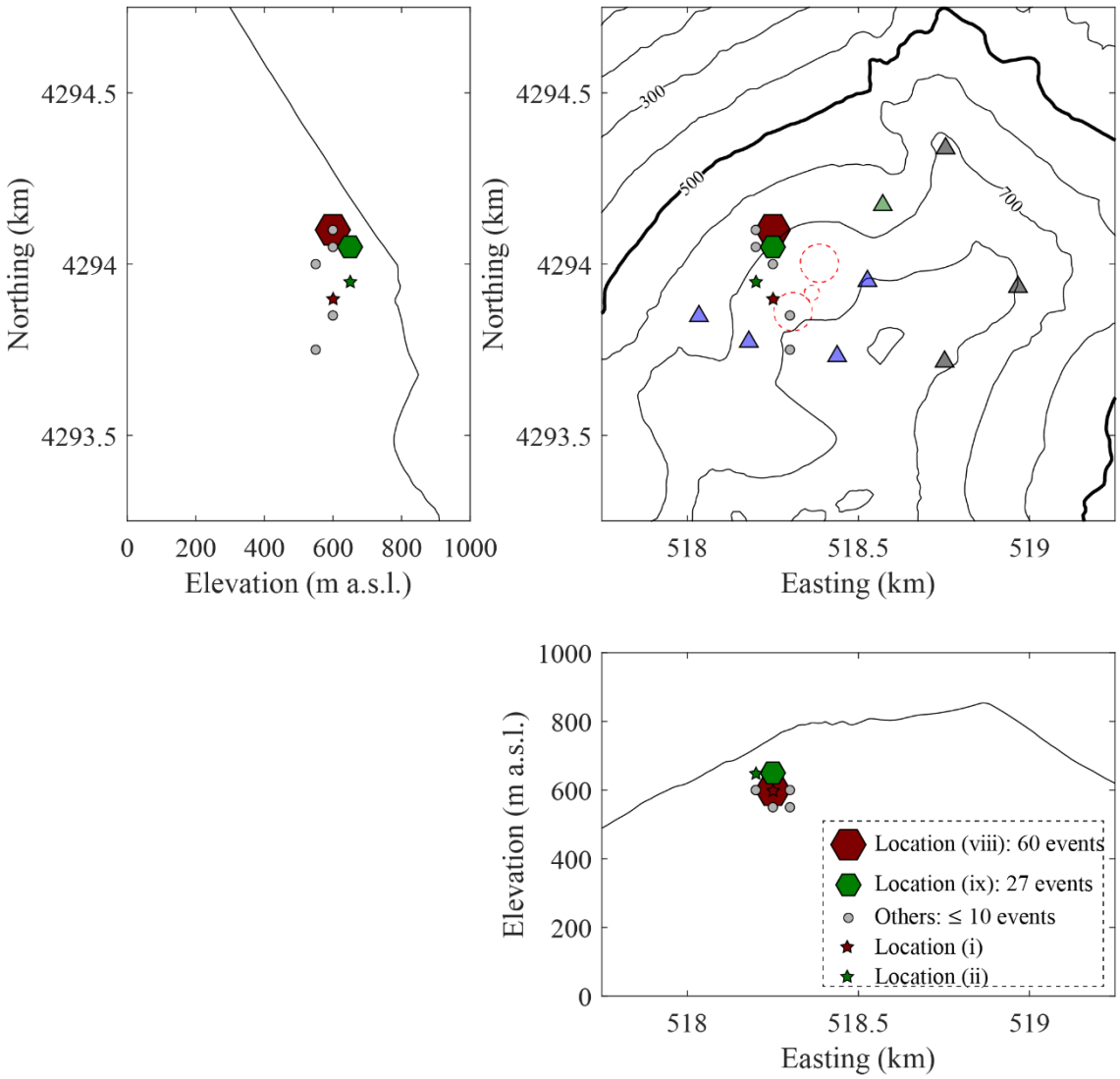

Figure 3.18 Source distribution of 103 VLP (0.05-0.2 Hz) seismic events determined by moment tensor inversion including the single forces. The brown hexagon shows the location of 60 events (location (viii)). The green hexagon shows the location of 27 events (location (ix)). The gray circles show the location of other events and each cluster include less than 10 events.

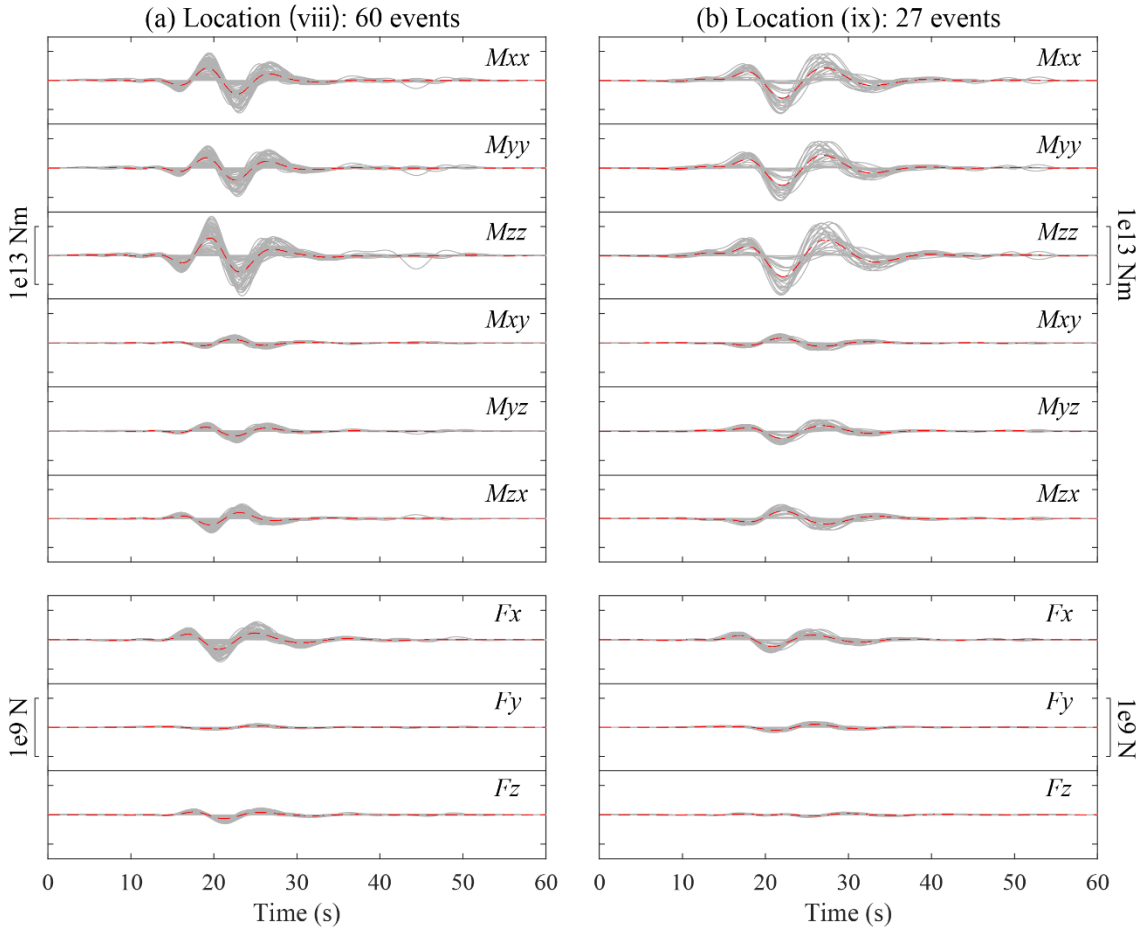

Figure 3.19 (a) Stacking of the moment tensor and single force solutions for the events in location (viii). The red dashed lines illustrate the average lines of the stacking moment tensor and single force solutions. (b) Similar to Figure 3.19 (a) for the events in location (ix).

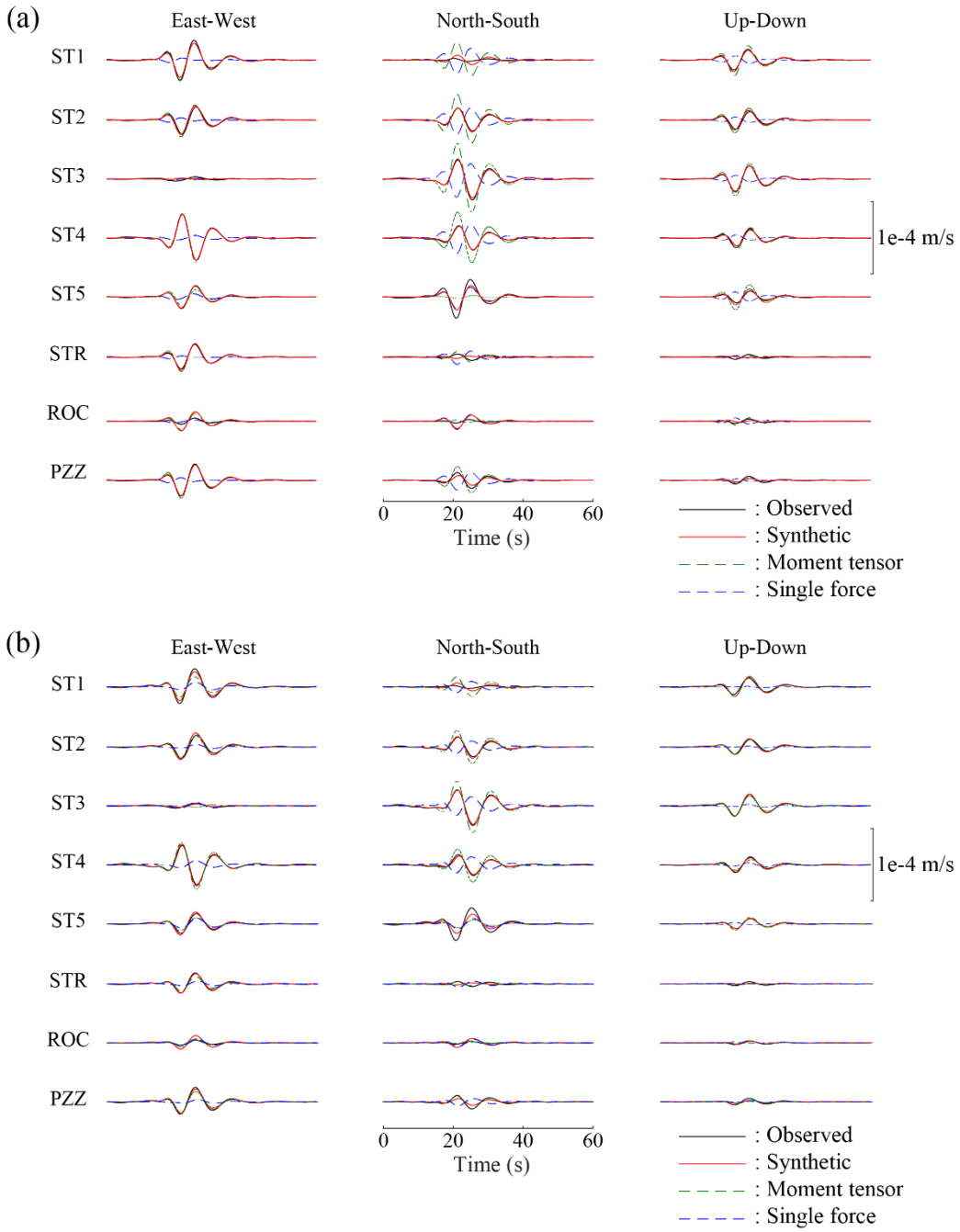

Figure 3.20 (a) Waveform fitting for an event in location (viii). The observed seismograms are represented by black lines and synthetic waveforms for the inversion results are represented by red lines. The green dashed lines indicate the waveforms computed by moment tensor solutions. The blue dashed lines show the waveforms computed by single force solutions. The residual of waveforms calculated by equation (3.10) is 7.3 %. (b) Similar to Figure 3.20 (a) for an event in location (ix). The residual of waveforms is 7.1 %.

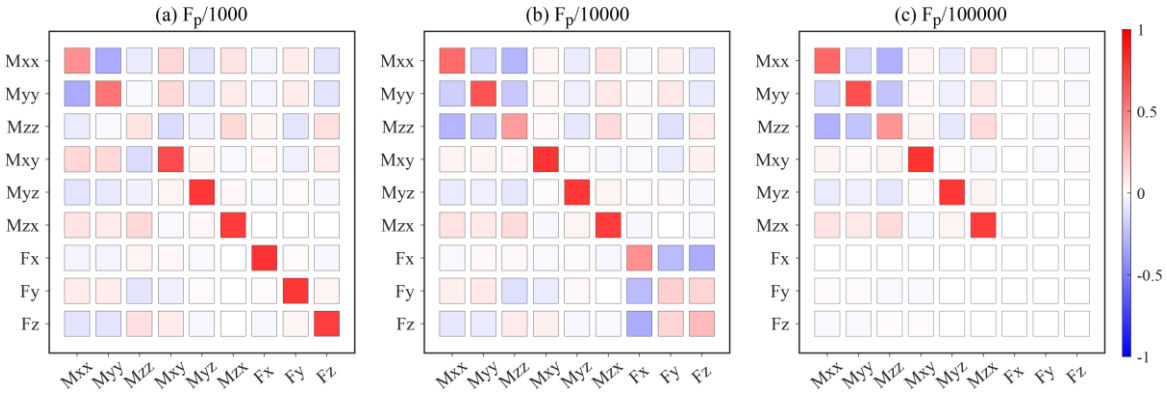

Figure 3.21 (a) Model resolution matrix including the single forces for source location (viii) with the amplitude weight of the Green's functions in the single forces of $F_p/1000$. (b) Similar to Figure 3.21 (a) for $F_p/10000$. (c) Similar to Figure 3.21 (a) for $F_p/100000$.

Chapter 4

Relative hypocenter determination of eruption earthquakes

In this chapter, the source locations of VLP signals at 0.05-0.2 Hz are estimated by using a method which combines the modified master event method after several previous studies (e.g. Stoddard and Woods 1990; Zollo et al. 1995) with the deconvolution technique (e.g., Snieder and Safak, 2006). Seismic events are located relative to the location of a "master event" using arrival time differences measured by deconvolving the single events (hereafter called "slave event") with the "master event" at each station. This method can be effective to investigate how the repetitive earthquakes are distributed around a master event based on changes in waveform correlation and source time function. By using this method, we examine the location errors and variabilities within a small region that is difficult to evaluate by the moment tensor inversion that uses a grid search.

4.1 Method

The arrival time of seismic wave at a station for the master event can be written as

$$t_{m,k} = T_k(x_m, y_m, z_m; x_k, y_k, z_k) + \tau_m, \tag{4.1}$$

where T_k is the travel time from the master event location (x_m, y_m, z_m) to the k-th station (x_k, y_k, z_k) and τ_m is the origin time of the master event. When a slave event is closely located to the master event, the arrival time difference between the master event and the slave event can be approximated to

$$\begin{aligned} \Delta t_k &\equiv t_{s,k} - t_{m,k} \\ &= T_k(x_s, y_s, z_s; x_k, y_k, z_k) + \tau_s - T_k(x_m, y_m, z_m; x_k, y_k, z_k) - \tau_m \\ &\cong \frac{\partial T_k}{\partial x_m}\Delta x + \frac{\partial T_k}{\partial y_m}\Delta y + \frac{\partial T_k}{\partial z_m}\Delta z + \Delta\tau, \end{aligned} \tag{4.2}$$

where (x_s, y_s, z_s) represents the location of the slave event, τ_s is the origin time of the slave event, $(\Delta x, \Delta y, \Delta z) = (x_s - x_m, y_s - y_m, z_s - z_m)$ is the relative location of the slave event from the master event, and $\Delta\tau = \tau_s - \tau_m$ is the origin time difference. We further also calculate the residual between the arrival time differences between the k-th and l-th stations such as

$$\begin{aligned}\Delta t_{kl} &\equiv \Delta t_k - \Delta t_l \\ &= \left(\frac{\partial T_k}{\partial x_m} - \frac{\partial T_l}{\partial x_m}\right)\Delta x + \left(\frac{\partial T_k}{\partial y_m} - \frac{\partial T_l}{\partial y_m}\right)\Delta y + \left(\frac{\partial T_k}{\partial z_m} - \frac{\partial T_l}{\partial z_m}\right)\Delta z,\end{aligned} \tag{4.3}$$

and the matrix form of equation (4.3) can be represented as

$$\mathbf{d}_t = \mathbf{G}_t \mathbf{m}_r\,, \tag{4.4}$$

in which $\mathbf{d_t}$ is the data vector associated with the time difference Δt_{kl} with dimensions of the number of station pairs, $\mathbf{G_t}$ represents the matrix consisting of the partial difference of the travel times, and $\mathbf{m_r}$ denotes the relative source location. The squared residuals between the observed and the synthetic seismograms are minimized by using the least-squares method, and the solution can be obtained as

$$\mathbf{m}_r^{\mathrm{s}} = \left(\mathbf{G}_t{}^{\mathrm{T}}\mathbf{G}_t\right)^{-1}\mathbf{G}_t{}^{\mathrm{T}}\mathbf{d}_t. \tag{4.5}$$

Error of the estimated relative location is computed by applying an error propagation rule. The residual vector between the observed and synthetic arrival time difference is written as

$$\mathbf{e} = \mathbf{d}_t^{\mathrm{syn}} - \mathbf{d}_t^{\mathrm{obs}}, \tag{4.6}$$

where $\mathbf{d}_t^{\mathrm{syn}}$ is the synthetic vector associated with the arrival time difference. The matrix of the errors $\sum_t$ is composed by the variance and covariance of the relative location error and defined as

$$\begin{aligned}\sum_m &\equiv \langle(\mathbf{m}_r^{\mathrm{s}} - \mathbf{m}_r^{\mathrm{true}})(\mathbf{m}_r^{\mathrm{s}} - \mathbf{m}_r^{\mathrm{true}})^{\mathrm{T}}\rangle \\ &= \langle\left(\left(\mathbf{G}_t{}^{\mathrm{T}}\mathbf{G}_t\right)^{-1}\mathbf{G}_t{}^{\mathrm{T}}\mathbf{e}\right)\left(\left(\mathbf{G}_t{}^{\mathrm{T}}\mathbf{G}_t\right)^{-1}\mathbf{G}_t{}^{\mathrm{T}}\mathbf{e}\right)^{\mathrm{T}}\rangle \\ &= \mathbf{C}\langle\mathbf{e}\mathbf{e}^{\mathrm{T}}\rangle\mathbf{C}^{\mathrm{T}} \\ &= \mathbf{C}\sum_t\mathbf{C}^{\mathrm{T}}, \end{aligned} \tag{4.7}$$

where $\mathbf{C}$ represents $\left(\mathbf{G}_t{}^{\mathrm{T}}\mathbf{G}_t\right)^{-1}\mathbf{G}_t{}^{\mathrm{T}}$ and the notation < > indicates the average values. Here, the off-diagonal components are assumed to be independent of each other in $\sum_t$. As a result, the error of the solution $\mathbf{m}_r$ is obtained by the following equation,

$$\sigma_i = \left(\sqrt{\sum_m}\right)_{ii}, \tag{4.8}$$

where i represents the errors along north-south (NS), east-west (EW) and up-down (UD) axes.

Arrival times of VLP seismic events are not easily measured by inspection nor automatic picking techniques. We next describe here a method based on the deconvolution technique (e.g., Snieder and Safak, 2006) to calculate the arrival time difference, Δt_k in equation (4.2), between the master and slave events at each station. Seismic signal representing the master event at the k-th station is expressed in the frequency domain by the following equation

$$u_{m,k}(\omega) = S_m(\omega)P_{m,k}(\omega)A_k(\omega)I_k(\omega), \tag{4.9}$$

where $S_m(\omega)$ represents the source spectrum of the master event, $P_{m,k}(\omega)$ is the propagation effect, $A_k(\omega)$ is the site amplification factor and $I_k(\omega)$ is the instrumental response. When the locations of master and slave events appear to be close to each other, the deconvolution of their signals $D_k(\omega)$ is expressed by the ratio of their spectra,

$$D_k(\omega) = \frac{u_{s,k}(\omega)}{u_{m,k}(\omega)} = \frac{S_s(\omega)P_{s,k}(\omega)A_k(\omega)I_k(\omega)}{S_m(\omega)P_{m,k}(\omega)A_k(\omega)I_k(\omega)} \cong \frac{S_s(\omega)}{S_m(\omega)}, \tag{4.10}$$

which is independent of the location of the station because the propagation effects can be regarded as almost equal ($P_{m,k}(\omega) \cong P_{s,k}(\omega)$). Hence, the spectral ratios calculated at all components of all the stations are almost the same to each other. Since the instrumental response $I_k(\omega)$ can be cancelled, the spectral ratios can be regarded as the relative source time function from the master

event. Therefore, we are able to include the seismic signals recorded by tiltmeters.

Equation (4.10) may become unstable near the notches in the spectrum $u_{m,k}(\omega)$. To stabilize the deconvolution spectrum, we use the following equation,

$$D_k(\omega) = \frac{u_{s,k}(\omega)u^*_{m,k}(\omega)}{\left|u_{m,k}(\omega)\right|^2 + \varepsilon}, \tag{4.11}$$

where the asterisk * denotes the complex conjugation and ε is the stabilization parameter set to be a percentage of the average spectral power of $u_{m,k}$ (Snieder and Safak, 2006). While the denominator in equation (4.11) has no phase characteristics, the numerator represents the cross spectrum of two signals, so that the arrival time difference between the master event and the slave event can be obtained by the inverse Fourier transform. Then, the bandpass filter of 0.05-0.2 Hz is applied to the deconvolution waveforms. Finally, the cross-correlation function (CCF) is applied to the deconvolution waveforms between the two stations for measuring the lag time Δt_{kl}.

Figure 4.1 illustrates the outline of the deconvolution analysis. We compare this analysis with the analysis by using the cross-correlation function only. The comparison suggests that the CCF obtained from the deconvolution analysis is more suitable for measuring the lag time than that obtained from the CCF analysis, because the CCF obtained from the CCF analysis sometimes shows several peaks which could result from Gibbs ringing induced by the band pass filter, which sometimes makes us pick up the incorrect peaks. Therefore, the arrival time difference can be more easily and reliably obtained by the deconvolution technique.

4.2 Results

In this study, an event with the largest RMS amplitude at UD component of ST1 in the source cluster of location (i) (Figure 3.2) is selected as the master event. The stabilization parameter (ε) is set to be 10 %. We select the best time window of deconvolution waveforms for measuring the lag time Δt_{kl}. We set the window width of deconvolution waveforms from 1.0 s to 10 s. We then measure the lag time Δt_{kl} by CCFs and obtain the correlation coefficients. We set that the threshold of the correlation coefficient is 0.90. This value comes from the similarity of VLP (0.05-0.2 Hz) waveform in the network. If the coefficient is below 0.90, the station pair is not used to measure the lag time. We calculate the number of station pairs that the correlation coefficient of two deconvolution waveforms is above 0.90 for each event and then take the mean number in the 103 VLP events.

Finally, we compare the average number of station pairs for each time window width. Figure 4.2 (a) shows the relationship between the time window width of deconvolution waveforms and the average number of station pairs. In this study, we select the window width of 6.5 s when the average number of station pairs is maximum. This time window is almost equivalent to the width of one pulse of the deconvolution waveform at 0.05-0.2 Hz (Figure 4.2 (b)).

Figure 4.3 shows the result of source locations of VLP signals at 0.05-0.2 Hz. The deep color indicates that the absolute source location error is determined to be less than 25 m, a half size of the grid size used in the moment tensor inversion in Chapter 3. There are 89 events shown in the deep color and there are 60 events located at the same position of the master event. Figure 4.3 (b) enlarges the cross sections shown in the black areas in Figure 4.3 (a). All events with the location error less than 25 m are located in these areas. The distribution shows that most of the VLP sources are located around the master event with the range of about 50 m in horizontal and about 80 m in depth. However, there appears to be no correlation between the relative source location and the source clusters determined by moment tensor inversion in Chapter 3. The location errors of the 89 events with the location errors less than 25 m are 0-5.2 m (EW), 0-15.8 m (NS), and 0-23.0 m (UD). There are 14 events with the location error above 25 m shown in the light color. Most of these events are located out of the black areas shown in Figure 4.3. The location errors of these 14 events are 7.5-50.6 m (EW), 13.7-108.6 m (NS), and 28.8-215.6 m (UD), respectively. This may be due to small number of station pairs that satisfy the threshold of the correlation coefficient of 0.90 or due to low signal-to-noise ratios of deconvolution waveforms. These may be derived from low signal-to-noise ratios of or low correlation of the observed VLP waveforms.

4.3 Discussion

Figures 4.4 (a), (b) and (c) compare the deconvolution waveforms on each source cluster determined by moment tensor inversion in Chapter 3. There seems to be almost similar in deconvolution waveforms between location (i) and location (ii). The difference which can be slightly seen after the peak may be due to difference in waveforms which can be seen after the onset of acoustic waves shown in Figure 3.6. However, the difference may not affect to measurement of the relative travel time difference at the window width of 6.5 s. We suggest two possibilities to interpret the two source clusters determined by moment tensor inversion. One is that the two main source clusters obtained from the moment tensor inversion may be separated because of the grid size limitation (50 m), which could hardly depend on travel time difference. The other is that the deconvolution waveforms

in the time window width of 6.5 s reflect relative changes of only a part of the VLP waveforms. Thus, the locations within a limited time may be almost same, although the source locations may change with time. We discuss the temporal change in VLP source during an eruption in Chapter 6.

We next discuss the stabilization parameter ε. The larger ε enables deconvolution to be stabilized, but the difference from the "true" deconvolution waveform becomes larger. The smaller ε enables deconvolution to approximate the "true" deconvolution waveform, but the calculation becomes more unstable. We change the stabilization parameters as 0.1 %, 1.0 %, 5.0 % and 10 % and compare the deconvolution waveforms. The comparison in Figures 4.5 (a) and (b) shows that the amplitude on smaller values of the stabilization parameter becomes larger than on the larger value. Figure 4.6 shows the source distribution of the 103 VLP earthquakes determined by our source location method when the stabilization parameter is set to be 0.1 %. The deep color indicates that the absolute source location error is determined to be less than 25 m. There are 77 events shown in the deep color and there are 59 events located at the same position of the master event. Figure 4.6 (b) enlarges the cross sections shown in the black areas in Figure 4.6 (a). All events with the location error less than 25 m are located in these areas. The result shows that several VLP events in location (ii) in Chapter 3 are located at several to 30 m north from and 5-50 m shallower than the master event. However, the differences from the master event are less than the grid size (50 m) in the moment tensor inversion. The location errors of the 77 events with the location errors less than 25 m are 0-5.5 m (EW), 0-10.9 m (NS), and 0-22.5 m (UD). There are 26 events with the location error above 25 m shown in the light color. Most of these events are located out of the black areas shown in Figure 4.6. The location errors of these 14 events are 2.0-54.2 m (EW), 5.6-120.0 m (NS), and 25.0-227.8 m (UD). The number of the events with the location error above 25 m is increased from 14 to 26. This may be due to the instability of the calculation of deconvolution and the trade-off between the stability and the certainty of deconvolution should be considered by trial and error.

We also investigate the relative source locations when the master event is one of the events located in location (ii) (Figure 3.2). The result shows that most of the relative source locations are located around the master event but there was no clear separation into two source clusters such as the result of moment tensor inversion. The source location errors are still within several tens of meters. We suggested the two possibilities to interpret the difference in the results between the moment tensor inversion and the relative hypocenter determination: the grid size limitation, or the temporal change in the source locations. However, it may be difficult to completely distinguish the factor here.

During the observation period, the eruptive activity was mainly concentrated on NE crater so that we could not discuss the relationship between the difference of eruptive craters and VLP activity. However, we will show the difference of relative source location and relative source time function by analyzing the VLP activity associated with the eruptions at both NE and SW craters. Our locating method will be useful to understand the magma movement in the conduit system at Stromboli volcano.

4.4 Summary

We have applied a precise relative hypocenter determination method which combined the master event method and the deconvolution technique. The deconvolution technique enables us to precisely obtain the relative arrival time difference between two seismic events. The VLP (0.05-0.2 Hz) sources range about 50 m in horizontal and about 80 m in vertical directions around the master event determined by the moment tensor inversion in Chapter 3. When the stabilization parameter on calculation of deconvolution is set to be 10 % of the average spectral power of seismogram of the master event, there are no correlation between the relative source location and the source clusters determined by the moment tensor inversion in Chapter 3. Similar results are obtained when the stabilization parameter on calculation of deconvolution is set to be 0.1 % or the master event is changed. We suggest that the two source clusters obtained from the moment tensor inversion may be separated because of the grid size limitation (50 m). We also consider the possibility that the relative locations change with time. Here, it may be difficult to completely conclude the factor of the location differences. However, the relative hypocenter determination based on waveform correlations and travel time differences examines the location errors and variabilities of the sources within a region that is difficult to evaluate by the grid size (50 m) of the moment tensor inversion. Our highly accurate hypocenter determination method with errors of tens of meters will be effective to monitor spatio-temporal changes in the repetitive earthquakes or to track movement of the magmatic column in the conduit at Stromboli volcano or other volcanoes.

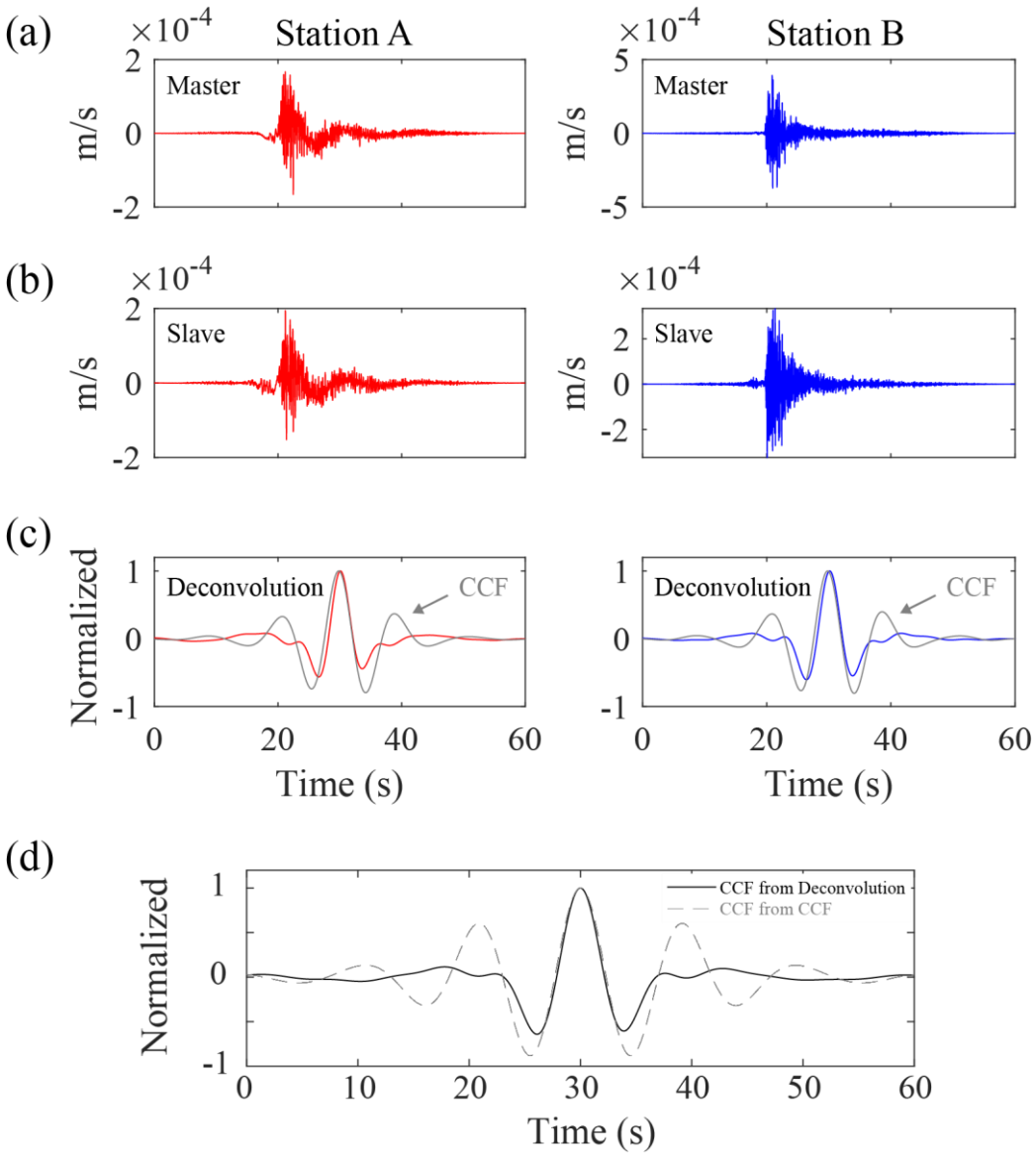

Figure 4.1 Outline of the deconvolution analysis. (a), (b) Seismograms of a master event and a slave event at two stations, respectively. (c) Deconvolution waveforms at different stations to obtain Δt_k in equation (4.2). The gray lines indicate the cross-correlation functions (CCFs) of the seismograms between the master and the slave event to compare with deconvolution. Note that both waveforms are band-pass-filtered at 0.05-0.2 Hz. (d) A cross-correlation function of two deconvolution waveforms in Figure 4.1 (c) is computed to measure Δt_{kl} in equation (4.3) (black line). The gray line indicates the CCF obtained from the two CCFs in Figure 4.1 (c).

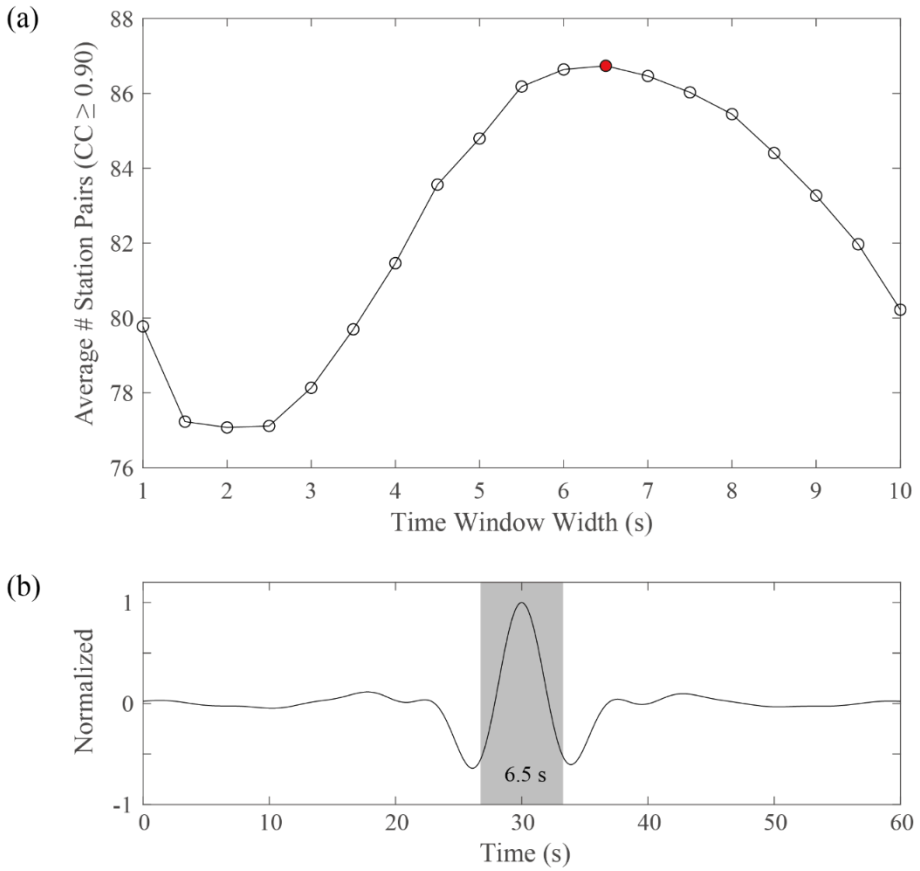

Figure 4.2 (a) The relationship between the time window width of deconvolution waveforms and the average number of station pairs that the correlation coefficient (CC) of two deconvolution waveforms to calculate Δt_{kl} in equation (4.3) is above 0.90 in 103 events. A red point indicates that the average number of station pairs is largest so that the time window width of deconvolution waveforms is determined as 6.5 s. (b) An example of deconvolution waveform and the time window of 6.5 s.

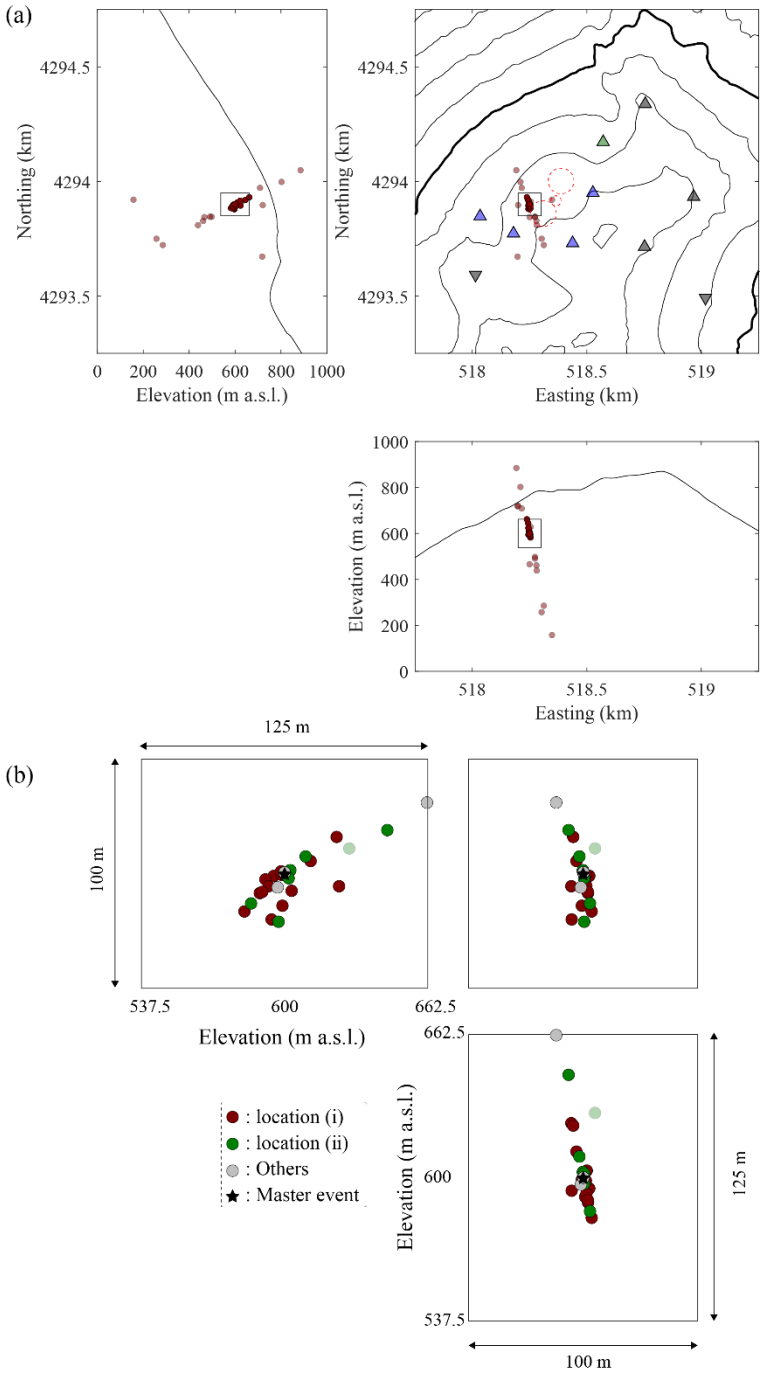

Figure 4.3 (a) Source distribution of the 103 VLP signals determined by our source location method. The deep color indicates that the absolute source location error is determined to be less than 25 m. The light color indicates that the source location error is above 25 m. (b) Zoom up of the source cluster. The color indicates the source clusters determined by moment tensor inversion in Chapter 3. The black star shows location of the master event. The master event is located by the moment tensor inversion.

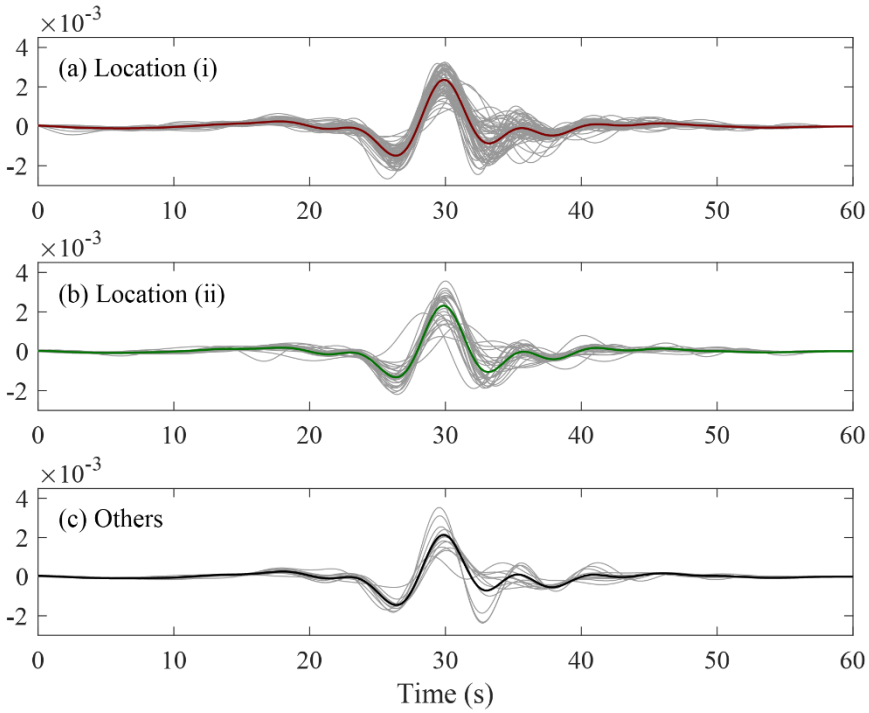

Figure 4.4 (a), (b), (c) Comparison of stacking of deconvolution waveforms on each source cluster determined by moment tensor inversion. The brown, green and black lines illustrate the mean of the stacking for location (i), location (ii), and others shown in Figure 3.2.

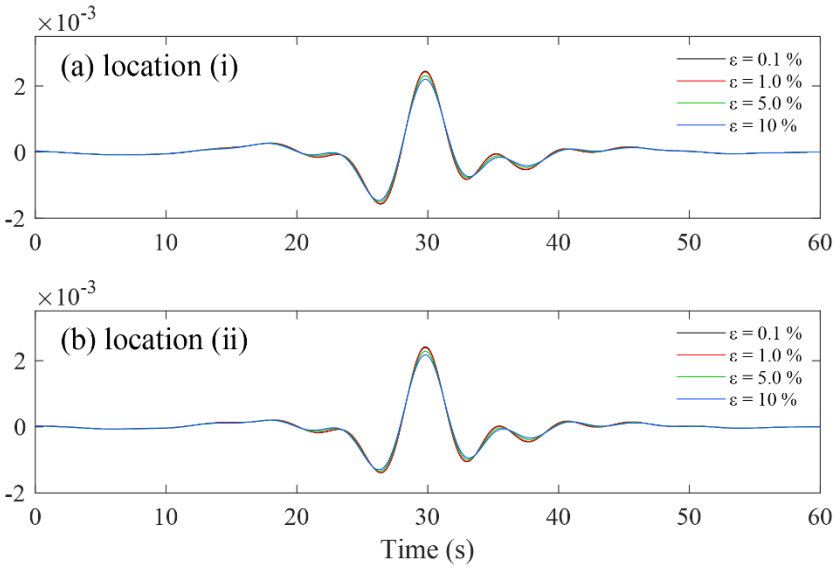

Figure 4.5 (a) The mean of stacking of deconvolution waveforms for location (i) shown in Figure 3.2. when the stabilization parameter ε is changed as 0.1 % (black), 1.0 % (red), 5.0 % (green), and 10 % (blue) of the average spectral power of seismogram of the master event. (b) Similar to Figure 4.5 (a) for location (ii).

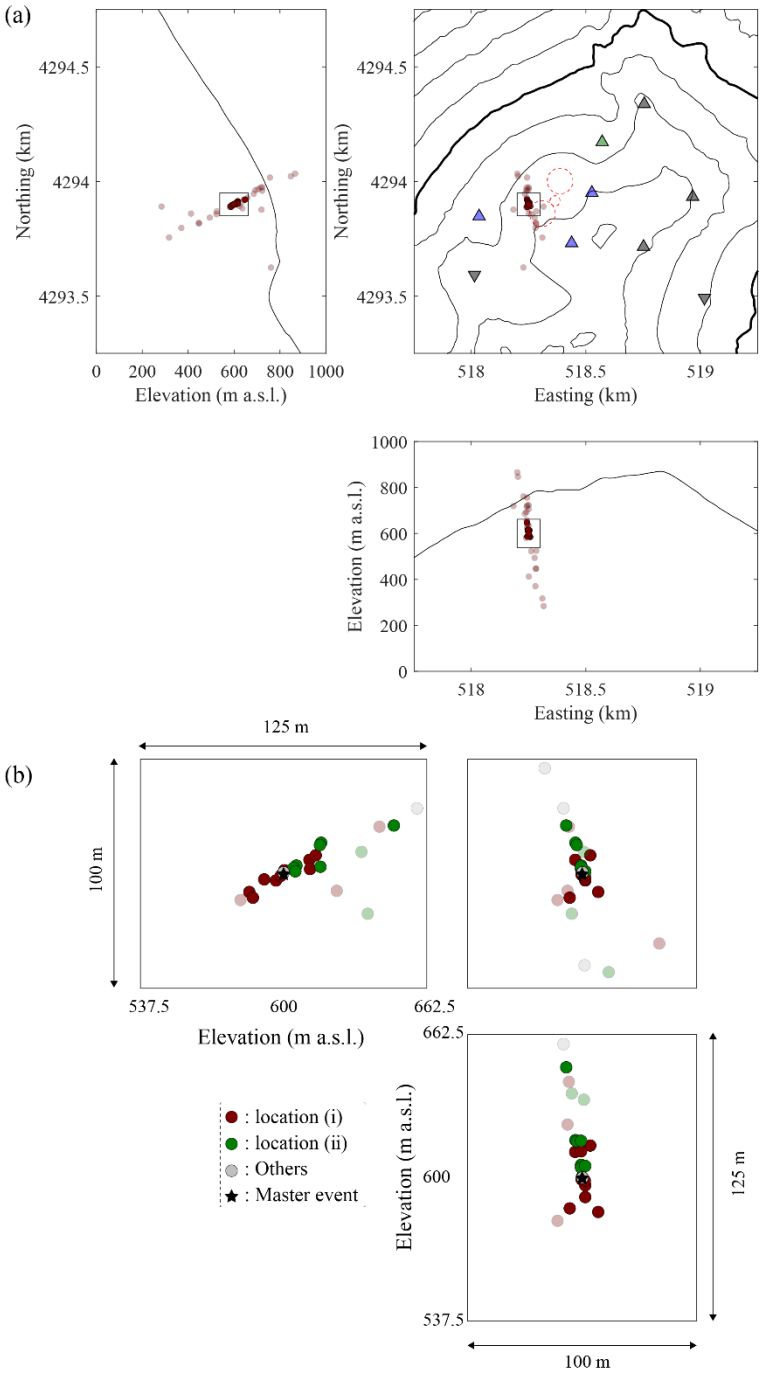

Figure 4.6 (a) Source distribution of the 103 VLP signals determined by our source location method when the stabilization parameter is set to be 0.1 % of the average spectral power of seismogram of the master event. The deep color indicates that the absolute source location error is determined to be less than 25 m. The light color indicates that the source location error is above 25 m. (b) Zoom up of the source cluster. The color indicates the source clusters determined by moment tensor inversion in Chapter 3. The black star shows location of the master event. The master event is located by the moment tensor inversion.

Chapter 5

Initial motion analyses of seismic and acoustic waves

In this chapter, we analyze seismic and acoustic signals, focusing of the time delay between the two signals. On Strombolian eruptions, the process of generation, ascent and bursting of a large gas slug in the conduit has been considered and these generate seismic, acoustic and thermal signals (Ripepe et al., 2001; Harris and Ripepe, 2007; Gurioli et al., 2014). The different source locations, propagation speeds and paths cause different arrival times of these signals. In this study, the thermal sensors had not been deployed in the very-near-field network but seismic and acoustic signals with high signal-to-noise ratio could be obtained in the very-near-field network. By using the high quality observation data and a conduit model proposed by Ripepe et al. (2001), we estimate source locations of bubble bursts and propagation velocity of magma or gas bubbles in the conduit. We mainly discuss the accuracy of these estimated parameters, comparing the results with previous studies and by changing model conditions.

5.1 A conduit model as inferred from arrival time difference between seismic and acoustic signals

Figure 5.1 (a) illustrates a schematic conduit model modified after Ripepe et al. (2001). The VLP source is considered to be the location of gas coalescence. The explosion source is considered to generate higher frequency seismic (> 1 Hz) signal and acoustic signal. The origin times of these signals appear to be different (Figure 5.1 (b)). These time delays can be explained as follows. The travel time of seismic wave above 1 Hz (t_s) is expressed as

$$t_s = \frac{r'}{\alpha}, \tag{5.1}$$

where r' represents the distance between the explosion source and the sensor (ST1) and α is the P-wave velocity. The travel time of acoustic wave (t_a) can be represented as

$$t_a = \frac{h_c}{c'} + \frac{x}{c}, \tag{5.2}$$

where h_c represents the distance between the explosion source and the surface in the conduit, c' is the sound speed in the conduit, x is the distance between the crater and the sensor, and c shows the sound speed in the air. Thus, the explosion source (h_c) can be obtained as a function of the arrival time difference $t_a - t_s$:

$$t_a - t_s = \frac{h_c}{c'} + \frac{x}{c} - \frac{r'}{\alpha}. \tag{5.3}$$

The distance (r') is the function of the explosion source depth (h_c) and expressed as

$$r' = \sqrt{(h_c + 43)^2 + x'^2} \tag{5.4}$$

where $h_c + 43$ represents the depth difference between the explosion source and the sensor (813 m a.s.l.) using the elevation of the crater terrace (770 m a.s.l.), and x' represents the horizontal distance from the crater to the sensor. Similarly, the time delay between seismic VLP and acoustic signals is expressed as;

$$t_a - t_{vlp} = \frac{h - h_c}{U} + \frac{h_c}{c'} + \frac{x}{c} - \frac{r}{\alpha}, \tag{5.5}$$

where h is the VLP source depth given by the source location results of the moment tensor inversion, r is the distance from the VLP source and the sensor, and U is the velocity at which the material (magma or gas) ascends in the magma-filled conduit section between the gas coalescence zone (VLP source) and the magma surface. The distance (r) is the function of the VLP source depth (h) and expressed as

$$r = \sqrt{(h + 43)^2 + x'^2}. \tag{5.6}$$

The optimal velocity of U can be obtained by using the observation value of $t_a - t_{vlp}$ and the result of the explosion source (h_c) obtained by equation (5.3).

5.2 Measurement of arrival times

It is generally difficult to pick up the initial motion of VLP seismic signals due to its long period wave. Braun and Ripepe (1993) manually picked the arrival time difference $t_a - t_{vlp}$ of 0.75-5.5 s with the mean value of 3.2 s at a station 300 m away from the active vent. The variation was so large but the propagation velocity U was estimated by using this mean value. The improvement of measurement applying automatically picking methods and using high quality data should be necessary to accurately obtain the conduit parameters. We use the data at ST1, which is only 115 m away from NE crater, because both seismic and acoustic signals associated with volcanic explosions are recorded with a high signal to noise ratio.

Raw velocity seismogram at ST1 sometimes shows clear very-long-period phases before the onset of explosions (Figure 5.2). We apply bandpass filters at 0.05-0.2 Hz to raw seismogram by changing the order and causal or acausal to examine how well the initial motion can be obtained. Comparison in Figure 5.2 (b) shows that the causal filter with 2nd-order seems to be appropriate and easier to pick up the initial motion. The acausal filter also enables us to pick up the initial motion but it seems to be earlier than the raw seismogram. In this study, we measure the onset time of VLP seismic (0.05-0.2 Hz) signals by manually picking raw seismograms and by automatically picking causal-filtered seismograms and compare these results.

We apply a method of Maeda (1985) for the automatic picking. This method is based on the concept that the onset of a phase is equivalent to the point dividing a section into two sections by using Akaike Information Criterion (AIC). The AIC value at k-th sample point in the total sample points n can be expressed as follow;

$$\mathrm{AIC}(k) = n \log 2\pi + k \log \sigma_1^2 + (n-k) \log \sigma_2^2 + n + 2 \times 4, \tag{5.7}$$

where σ_1^2 and σ_2^2 represent the variations in first section from 1st to k-th sample point and second section from $(k+1)$-th to n-th sample point assuming that the seismic noise is based on a normal distribution model. The clarity of picking is expressed by the following equation,

$$DD = \left(\mathrm{AIC}(k_{\min} - \delta k) + \mathrm{AIC}(k_{\min} + \delta k) - 2\mathrm{AIC}(k_{\min})\right)/\delta k^2, \tag{5.8}$$

where $k_{\min}$ represents the sample point where $\mathrm{AIC}(k)$ is the minimum and δk shows the number of samples. We use $\delta k = 10$ which corresponds to 0.1 s for seismic signals above 1 Hz

and acoustic signals, and $\delta k = 30$ (0.3 s) for VLP seismic signal. This equation evaluates how much sharply the AIC function is impulsive around $k_{\min}$. We select time windows for calculating the AIC functions by trial and error. The time window for VLP seismic signals is set to be 8 s starting from 10 s before the time of maximum amplitude of acoustic signal ($t_{\mathrm{a}}^{\max}$). The time window for seismic signals above 1 Hz is set to be 3 s starting 2.5 s before $t_{\mathrm{a}}^{\max}$. The time window for acoustic signals is set to be 3 s starting 2 s before $t_{\mathrm{a}}^{\max}$.

Figure 5.3 (a) shows an example of automatic picking for seismic, and acoustic signals associated with an explosion. The estimated arrival times at which the AIC values are minimum are 26.67 s (VLP, 0.05-0.2 Hz), 29.55 s (seismic, > 1 Hz) and 29.95 s (acoustic), respectively, when the lapse time of the maximum amplitude of acoustic signal is set at 30.00 s. DD values show higher values for seismic (> 1 Hz) and acoustic signals than the VLP seismic signal. According to Maeda (1985), the certainty of picking can be ensured when DD value is above 1.0. In order to obtain high quality arrival time data, we regard the DD values above 5.0 as high quality for seismic (> 1 Hz) and acoustic signals at ST1 in this study. For VLP seismic signals, we evaluate the quality by comparing the manually picking results. Figure 5.3 (b) illustrates the arrival time picking of VLP seismic signal for causal filter, acausal filter, and raw data. The time difference between causal-filtered waveform and raw seismogram is only 0.50 s. On the other hand, the arrival times that are measured from acausal-filtered waveform are not appropriate.

5.3 Results

We use the data from 07:05 to 23:59 on September 26, 2016 . There are 45 VLP events during the period. Figure 5.4 shows the results of arrival time difference $t_{\mathrm{a}} - t_{\mathrm{s}}$ and $t_{\mathrm{a}} - t_{\mathrm{vlp}}$. The mean with standard deviation of the time difference $t_{\mathrm{a}} - t_{\mathrm{s}}$ is estimated to be 0.37 ± 0.05 s for the selected 26 events out of the 45 events. The time difference $t_{\mathrm{a}} - t_{\mathrm{vlp}}$ is estimated to be 3.77 ± 0.71 s for the selected 29 events out of the 45 events. Figure 5.5 (a) shows the comparison of arrival picking results of VLP seismic signals. This figure shows that our automatically picking results are almost same as or slightly delayed from the manually picking results. The mean of absolute time differences $\left|t_{\mathrm{causal}} - t_{\mathrm{manually}}\right|$ is 0.80 s. Thus, we select the VLP events with the time difference less than 0.80 s. Figure 5.5 (b) shows the comparison of picking results between causal and acausal filter, but the onsets for acausal-filtered waveforms are systematically 2.0-3.0 s earlier than the ones for causal-filtered waveforms.

Figure 5.6 illustrates the results of the explosion source (h_{c}) and the propagation velocity (U).

We assume a sound speed in the air (c) of 340 m/s. We use a sound speed in the conduit (c') of 708 m/s assuming the temperature in the conduit (T_c) is 1273 K, the same order of magma temperature and $c' = c(T_c/T_{air})^{-1/2}$ (Cas and Wright, 1992). A P-wave velocity (α) of 3500 m/s (Chouet et al., 2003), the VLP source depth (h) of 170 m (600 m a.s.l.), and the distance from NE crater to the station (x) of 115 m are used. The mean values with standard deviation of the explosion source depth (h_c) and the propagation velocity (U) are estimated to be 72.9 ± 42.8 m, and 30.6 ± 13.4 m/s, respectively, for high quality picking results shown by black filled circles. Source depths of two events are estimated to be negative. This may be because the temperature in the conduit is lower than 1273 K. The lower temperature makes the sound speed inside the conduit decrease and the explosion depth deeper. For example, when the sound speed inside the conduit (c') of 340 m/s ($= c$) is used, the depths of the two events are improved to be -8.7 m (from -18.8 m), and -1.8 m (from -3.7 m), which are almost at the surface of the crater. The propagation velocities estimated by manually picking results show similar tendency with the results from automatically picking.

Table 5.1 compares the results of VLP source location, the explosion source (h_c) and the propagation velocity (U) between this study and previous studies. Ripepe et al. (2001) and Harris and Ripepe (2007) fixed time difference corresponding to $t_a - t_{vlp}$ using the mean value of 3.2 s. Gurioli et al. (2014) fixed the explosion source to 100 m depth so that the propagation velocity could be estimated with small variation. Our results using the very-near-field observation data are within the range of the values estimated by the previous studies.

5.4 Discussion

5.4.1 Comparison with the result using a different station

We analyze the seismic and acoustic data at ST3, which is 280 m away from NE crater, to verify the results of the conduit parameters. Compared to the data at ST1, higher signal-to-noise ratios of VLP seismic and lower signal-to-noise ratios of higher frequency seismic and acoustic signals are recorded at this station. Figure 5.7 (a) shows an example of raw seismogram at UD component of ST3. This contains stronger VLP components than ST1, suggesting the centroid of VLP source determined at west of the eruptive craters in Chapter 3 and 4. In order to remove VLP components as much as possible, we apply a causal high-pass filter above 3 Hz to seismic signals and then measure the onsets of seismic signals (t_s). Due to lower signal-to-noise ratios, the thresholds of DD values for seismic (> 3 Hz) and acoustic signals are set to be 1.0 to regard as high quality data.

Figures 5.7 (b) and (c) compare the results of the conduit parameters between ST1 and ST3. The black filled circles satisfy the conditions of high quality data at both ST1 and ST3. The mean values with standard deviation of the explosion source depth (h_c) and the propagation velocity (U) are estimated to be 81.1 ± 34.5 m, and 29.0 ± 14.2 m/s, respectively, from the analysis of data at ST3. The comparison shows that the results at ST3 are generally consistent with the results at ST1. It is suggested that high-quality data with large amplitudes of the geophysical signals even at a little distant station enable us to accurately measure the conduit parameters. If the eruptive activity is more active, the seismic and acoustic data at the permanent stations will be useful to accurately monitor the magma level.

5.4.2 Examination of different parameters

We examine the conduit parameters by changing the VLP source location, P-wave velocity, and sound speed inside the conduit to evaluate how much variation the estimated values have. The VLP source depth (h) is changed from 170 m (600 m a.s.l.) to 120 m (650 m a.s.l.) based on moment tensor inversion results and relative hypocenter determination in Chapter 3 and 4. The P-wave velocity is changed to 2000 m/s (Chouet et al., 1997). The sound speed inside the conduit is assumed to be 340 m/s, which is the same as the sound speed in the air, showing possible minimum value. Table 5.2 summarizes the results for different parameter conditions. The result shows that the P-wave velocity critically affects the explosion source depths. When the VLP source location is 120 m depth (650 m a.s.l.) and the P-wave velocity is 2000 m/s, the propagation velocity becomes so small (3.6 ± 16.3 m/s), but a half of the events (24/45) have negative velocities. This suggests that P-wave velocity of 3500 m/s may be more appropriate than below 2000 m/s. The result for the sound speed in the conduit of 340 m/s indicate the upper limit of the propagation velocity (U) in this conduit model condition.

5.4.3 Examination of other conduit models

The conduit model condition presented by Ripepe et al. (2001) assumes that the gas coalescence source is located just below the crater. However, our source location results indicate that the VLP source is located at west from the eruptive NE crater. Following the VLP source location, we present two plausible conduit configurations (Figures 5.8 (a) and (b)). The first model (Figure 5.8 (a)) shows that the VLP source suggests the location of gas accumulation at the top of the chamber (e.g., Chouet

et al., 1997). In this case, propagation velocity becomes faster due to the path from a horizontal extension to a vertical conduit (Δx). The distance (r) is expressed as

$$r = \sqrt{(h + 43)^2 + (\Delta x + x')^2}\,. \tag{5.9}$$

When we assume the VLP depth (h) of 170 m (600 m a.s.l.), the mean velocity with standard deviation is estimated to be 98.8 ± 18.3 m/s. The second model (Figure 5.8 (b)) shows that the conduit directly elongate from the VLP source to the crater. In this case, the distance (r') is expressed as

$$r' = \sqrt{(h_c + 43)^2 + (h_c \frac{\Delta x}{h} + x')^2}. \tag{5.10}$$

When we assume the VLP depth (h) of 170 m (600 m a.s.l.), the mean values of the explosion source (h_c) and the propagation velocity (U) are estimated to be 48.5 ± 26.7 m, and 62.2 ± 15.4 m/s. Two results are faster than the theoretical values of slug ascent (Batchelor, 1967). Thus, models that can explain high-speed propagation velocity may not depend on the structures beneath the craters. Rather, physical properties of bubbles or another model such as pressure waves propagating in the magma-filled conduit (Tameguri et al., 2002) are more likely to explain fast propagation velocity.

5.4.4 Examination of seismic signals at different frequency bands

The moment tensor inversion results in Chapter 3 show that the centroids of seismic sources at 0.2-0.5 Hz and 0.5-1.0 Hz are mainly located below the crater terrace. These earthquakes occur almost simultaneously (Figure 3.11). We measure the initial motion of seismic signals at 0.2-0.5 Hz and 0.5-1.0 Hz by using the same method as 0.05-0.2 Hz to estimate the propagation velocities (U) at different frequency bands. We use the same 29 events as 0.05-0.2 Hz (see Section 5.3). We assume a sound speed in the air (c) of 340 m/s, a sound speed in the conduit (c') of 708 m/s, a P-wave velocity (α) of 3500 m/s. Based on the moment tensor inversion results, we use the source depth (h) of 170 m (600 m a.s.l.) for 0.05-0.2 Hz and 0.2-0.5 Hz, and the source depth (h) of 70 m (700 m a.s.l.) for 0.5-1.0 Hz. Table 5.3 summarizes the source depth and the result of the propagation velocities (U) at different frequency bands. The evaluation of the clarity of picking for 0.2-0.5 Hz

and 0.5-1.0 Hz by using DD values is not conducted so that the variation becomes larger. However, the propagation velocity at 0.2-0.5 Hz is estimated to be on the order of tens of m/s (50.7 ± 28.5 m/s), which is similar to 0.05-0.2 Hz. The propagation velocity at 0.5-1.0 Hz is estimated to be almost zero (0.2 ± 25.1 m/s) because the explosion source depth (72.9 ± 42.8 m) is almost same as the source depths that are estimated by the moment tensor inversion. The result implies that no large propagation of gas bubbles occurs just before the explosion around the source and that this source depth is where a burst of accumulated gas below the crater is triggered.

5.5 Summary

In this chapter, we have analyzed the seismic and acoustic signals associated with small explosions to estimate the conduit parameters. The automatically picking method presented by Maeda (1985) and seismic and acoustic data in the very-near-field network enable us to obtain high quality data of arrivals of seismic and acoustic signals. The explosion source depth is estimated to be 72.9 ± 42.8 m. The propagation velocity of magma/gas inside the conduit is estimated to be 30.6 ± 13.4 m/s when the VLP source depth is 170 m. The high-speed propagation of magma/gas is estimated by examining the data at a different station, different model parameters, and different conduit models. The source of LP earthquakes at 0.5-1.0 Hz located very close to the explosion source may trigger the bubble burst in the conduit. Our accurately estimated conduit parameters will contribute to understand the conduit dynamics at Stromboli volcano or to the introduction of a new model of Strombolian eruptions.

Table 5.1 Comparison of the estimated results of VLP source, explosion source, and propagation velocity between this study and the previous studies. The methods and concepts for estimating the parameters are also listed. The value written by gray shows the result when the VLP source is at 650 m a.s.l.

	This study	Ripepe et al. (2001) Harris and Ripepe (2007)	Gurioli et al. (2014)
VLP	600-650 m a.s.l.	500 m a.s.l.	400-500 m a.s.l.
	Moment tensor inversion	Polarization analysis / Moment tensor inversion (Chouet et al., 2003; Marchetti and Ripepe, 2005)	
h_c	72.9 ± 42.8 m	20-220 m	100 m (mean)
	Time difference between infrasound and high frequency seismic signal	Time difference between infrasound and thermal signal that records emission of gas or fragments	
U	30.6 ± 13.4 m/s, 14.4 ± 13.1 m/s	10-70 m/s	13-25 m/s
	Time difference between infrasound and VLP signal		

Table 5.2 Comparison of the estimated results of explosion source and propagation velocity for different conditions of P-wave velocity (α) and sound speed inside the conduit (c'). The values written by gray show the results when the VLP source is at 650 m a.s.l.

	$\alpha =$ 3500 m/s $c' =$ 708 m/s	$\alpha =$ 2000 m/s $c' =$ 708 m/s	$\alpha =$ 3500 m/s $c' =$ 340 m/s
h_c	72.9 ± 42.8 m	105.6 ± 50.9 m	32.1 ± 18.7 m
U	30.6 ± 13.4 m/s	20.5 ± 16.2 m/s	44.3 ± 8.1 m/s
U	14.4 ± 13.1 m/s	3.6 ± 16.3 m/s	28.2 ± 6.7 m/s

Table 5.3 Comparison of the source depths that are estimated by moment tensor inversion and the results of propagation velocities (U) for different frequency band. The P-wave velocity (α) of 3500 m/s and the sound speed inside the conduit (c') of 708 m/s and the sound speed in the air (c) of 340 m/s are assumed.

	0.05-0.2 Hz (VLP)	0.2-0.5 Hz (VLP)	0.5-1.0 Hz (LP)
h	170 m (600 m a.s.l.)	170 m (600 m a.s.l.)	70 m (700 m a.s.l.)
U	30.6 ± 13.4 m/s	50.7 ± 28.5 m/s	0.2 ± 25.1 m/s

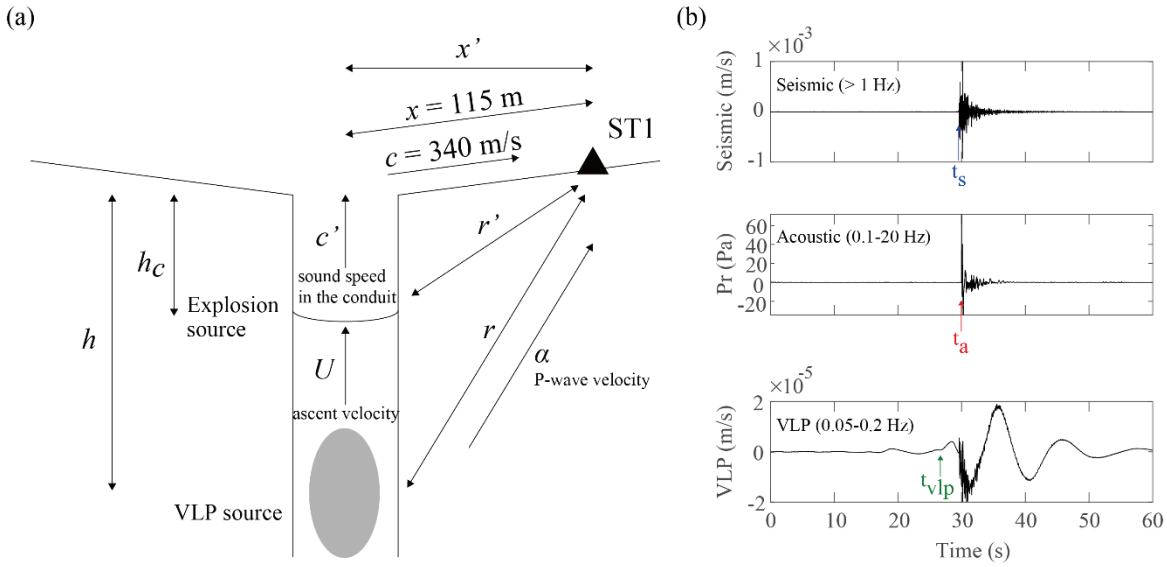

Figure 5.1 (a) A schematic conduit model for shallow system at Stromboli volcano modified after Ripepe et al. (2001). The VLP source is located at depth h below the surface. The explosion source is located at depth h_c. The propagation velocity from the depth h to the depth h_c is U. The parameters c' and c show the sound speeds inside the conduit and in the air, respectively. The parameters r' and r show the distance from explosion source and VLP source to the sensor (ST1). The distance from the crater surface to the sensor is x (115 m). The parameter x' represents the horizontal distance from the crater to the sensor. The parameter α illustrates the P-wave velocity. (b) Example of seismic (> 1 Hz), acoustic (0.1-20 Hz), and VLP seismic (0.05-0.2 Hz) signals showing the origin time of each signal.

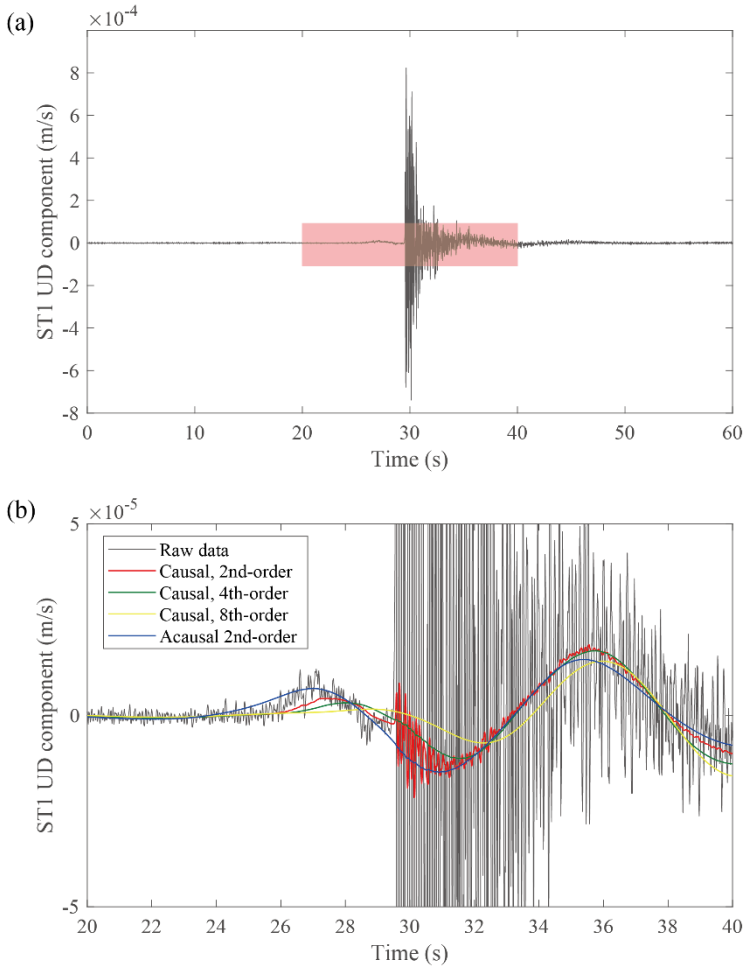

Figure 5.2 (a) Example of velocity seismogram at UD component of ST1. (b) Zoom up of the waveform shown in Figure 5.2 (a) and VLP (0.05-0.2 Hz) waveforms filtered by different types. The filter types are listed in the upper left part of the panel.

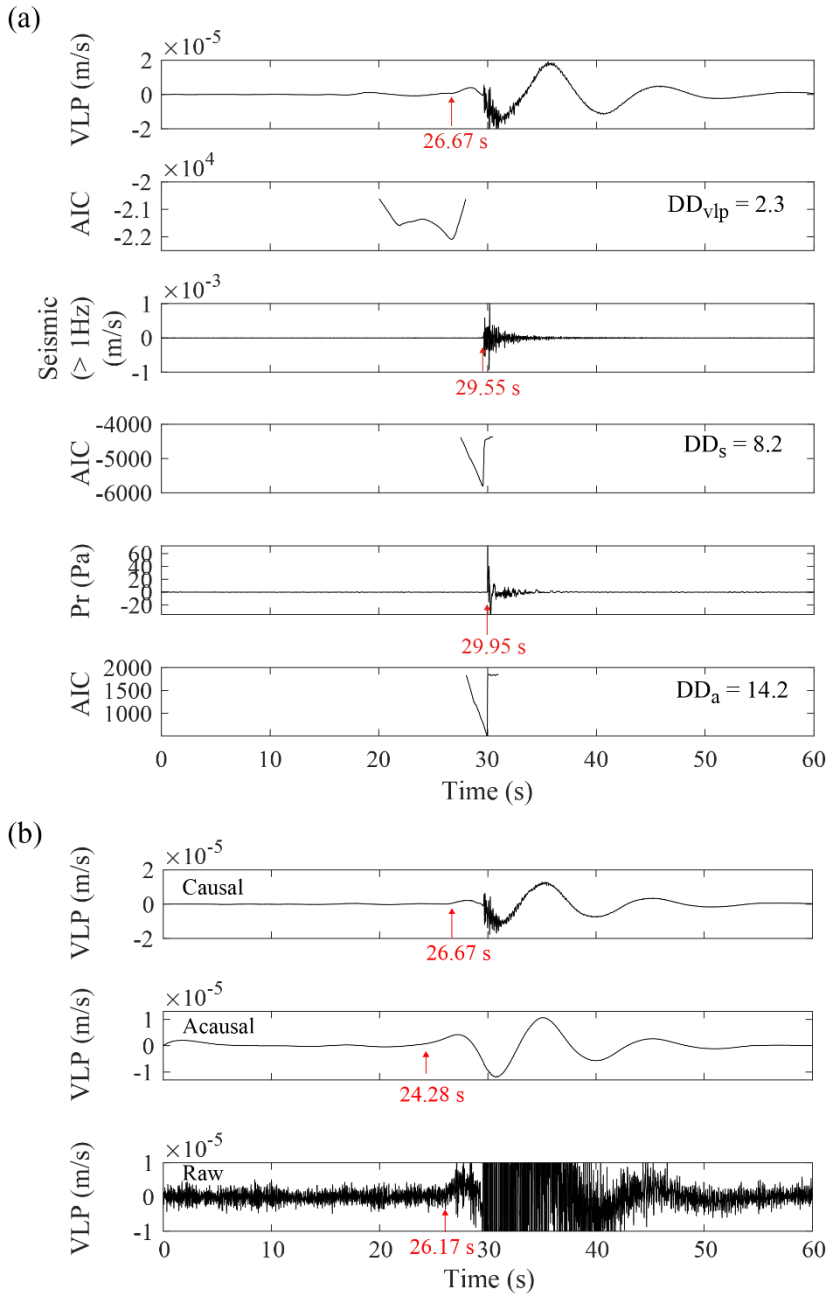

Figure 5.3 (a) Initial motion picking of VLP seismic, seismic (> 1 Hz), and acoustic signals. The red arrows show the origin times when the maximum amplitude of acoustic signal is at 30.00 s. The DD values listed in the upper right part of AIC functions show the clarity of piking results. (b) Initial motion picking for causal-filtered, acausal-filtered and raw waveforms (enlarged). The arrival times for the upper two waveforms are obtained by automatically picking, and the arrival time for the raw waveform is manually obtained.

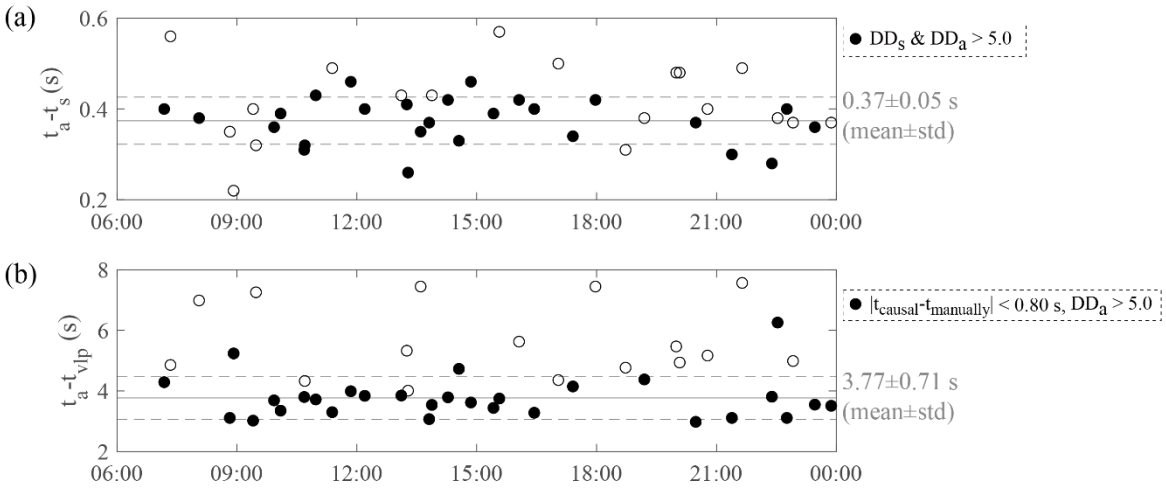

Figure 5.4 (a) The time series of the arrival time $t_a - t_s$ on 26 September 2016. The black filled circles show the data with DD values for seismic (> 1 Hz, DD_s) and acoustic signals (DD_a) above 5.0. The non-filled circles show other events. (b) The time series of the arrival time $t_a - t_{vlp}$ on 26 September 2016. The black filled circles show the data with the time difference between automatically and manually picking less than 0.80 s (mean value), and DD_a above 5.0. The non-filled circles show other events.

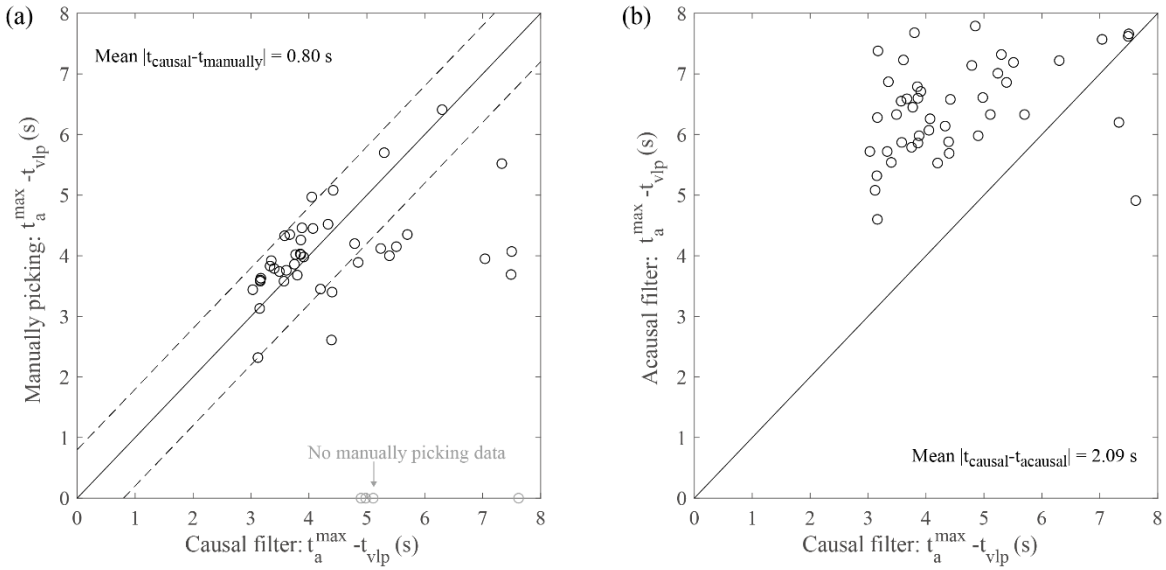

Figure 5.5 (a) Comparison of arrival time picking results between the causal-filtered waveforms and raw seismograms. The gray circles show the data without manually picking data due to very low amplitude of the first phase. The dashed lines illustrate the mean value of the time differences $|t_{\text{causal}} - t_{\text{manually}}|$ for all 45 events. (b) Comparison of arrival time picking results between the causal-filtered waveforms and acausal-filtered waveforms. The mean value of the time differences $|t_{\text{causal}} - t_{\text{acausal}}|$ is 2.09 s.

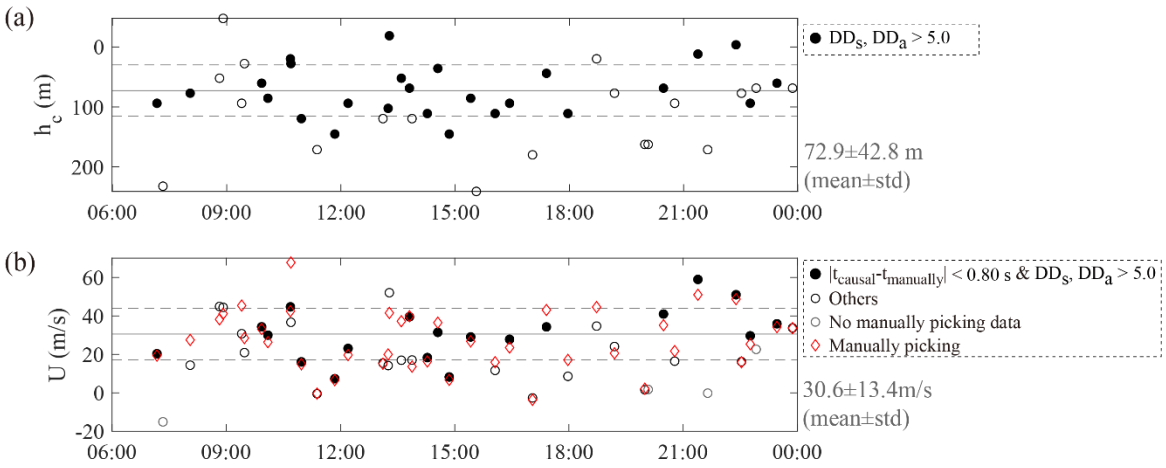

Figure 5.6 (a) The time series of the explosion source depth on 26 September 2016. The black filled circles show the data with DD values lager than 5.0 for seismic (> 1 Hz, DD_{s}) and acoustic signals (DD_{a}). The non-filled circles show the other events. (b) The time series of the propagation velocity for the events on 26 September 2016. The black filled circles show the data with the time difference of < 0.80 s (mean value) between automatically and manually picking ($\left|t_{\mathrm{causal}} - t_{\mathrm{manually}}\right|$), and DD_{s} and DD_{a} > 5.0. The non-filled black circles show the other events and the gray circles show the data without manually picking data. The red diamonds show the results of the propagation velocity estimated by using manually picking data.

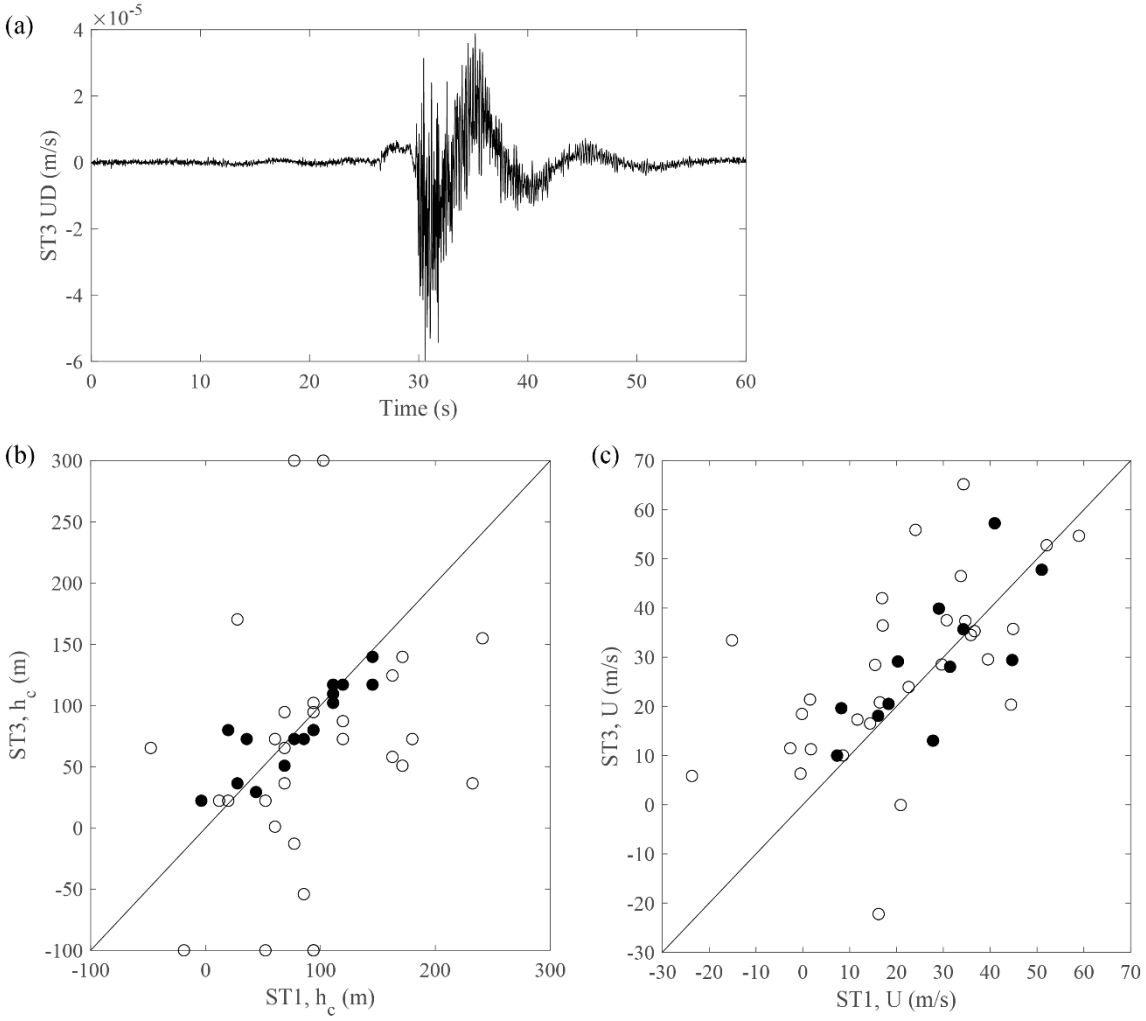

Figure 5.7 (a) Raw velocity seismogram associated with an explosion recorded at UD component of ST3. (b) Comparison of the estimated explosion source depth between ST1 and ST3. The black filled circles show the data with DD values for seismic (> 1 Hz for ST1 and > 3 Hz for ST3) signals (DD_{s}) and acoustic signals (DD_{a}) above 5.0 at ST1 and above 1.0 at ST3. The non-filled circles show other events. (c) Comparison of the estimated propagation velocities between ST1 and ST3. The black filled circles show the data with the time difference between automatically and manually picking ($\left|t_{\mathrm{causal}} - t_{\mathrm{manually}}\right|$) less than 0.80 s (mean value), and DD_{s} and DD_{a} above 5.0 at ST1 and above 1.0 at ST3. The non-filled circles show other events.

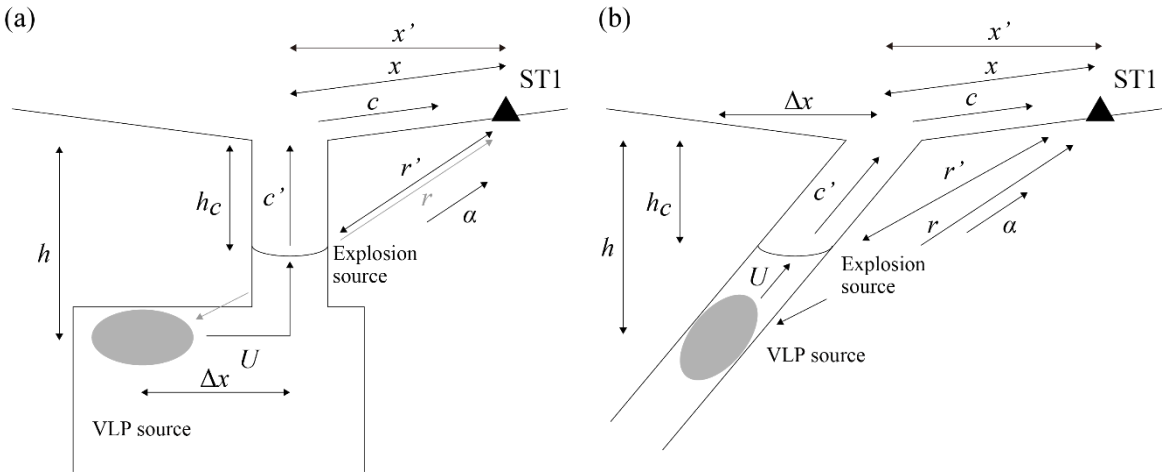

Figure 5.8 (a) A schematic conduit model for shallow system at Stromboli volcano based on the VLP source located at the west of the eruptive crater. In this model, the gas is accumulated at the top of the chamber and laterally moves to below the crater with a distance of Δx. (b) A different plausible model assuming that conduit directly elongate from the VLP source to the crater. The distance Δx represents the horizontal offset of the VLP source from the crater.

Chapter 6

Discussion

6.1 Analysis of temporary observation data in June 2015

In the beginning of June 2015, we have conducted a temporary seismic observation and deployed five short-period (2 Hz) seismometers at Stromboli volcano. These stations were deployed within 1 km from the craters for about two days to improve the accuracy of source location results. Figure 6.1 shows the distribution of geophysical network in June 2015. Two stations (LFS and OHO) were equipped with Sercel L-22D seismometers. The seismic signals were recorded at a sampling frequency of 200 Hz and an A/D resolution of 24 bits (Hakusan Kougyou Co., LS-8800). Three stations (LSC, PZT and PZZ) were equipped with short-period KVS-300 seismometers (Kinkei System Co.) and the signals were recorded with a sampling frequency of 250 Hz and an A/D resolution of 18 bits (Kinkei System Co., EDR-X7000). In addition, a Trillium compact (Nanometrics Inc., natural period 120 s) broadband seismometer at RFR was deployed from May 2014. The signals were recorded with a sampling rate of 100 Hz and an A/D resolution of 24 bit (Keisoku-giken, HSK-9550). This temporary seismic network was integrated with the signals of the tilt sensor (Applied Geomechanics, Model 701-2) deployed at CPL, which were recorded with a sampling rate of 100 Hz and an A/D resolution of 24 bit (Keisoku-giken, HSK-9550), and three permanent broadband seismometers of the University of Florence (SCI, STR and PZZ). The record at a permanent station at ROC is not used in this chapter because of errors in time correction. We analyze the data recorded from 7 June at 17:00 to 9 June at 12:00 in 2015 (UTC).

Figure 6.2 shows the example of seismic and acoustic signals at PZZ. Bandpass filtered seismogram at 0.05-0.2 Hz (VLP), high-pass filtered seismogram above 1 Hz and infrasound at 0.1-5 Hz are shown. The seismo-acoustic activity could be divided into two characteristics. One is that VLP seismic signals are accompanied with seismic signals above 1 Hz but very low or no acoustic signals. Another is that seismic signals above 1 Hz are accompanied with acoustic signals but very low or no VLP seismic signals. During our experiment, explosive activity was quite low and a small amount of red hot incandescent lava fragments ejected outside the crater rims were sometimes observed. This visual observation is consistent with a deep magma level in the conduits as inferred by the polarization analysis of the VLP seismicity after the August 2014 effusive flank eruption

(Valade et al., 2016). At station PZZ, we detect 12 events that show very low VLP amplitude and clear seismic (> 1 Hz) amplitude with clear infrasound (Figure 6.3). We measure the initial motion of seismic (> 1 Hz) and acoustic signals. The time differences are measured to be 1.27-1.40 s. We assume a sound speed in the air of 340 m/s, a sound speed in the conduit of 708 m/s, a P-wave velocity of 3500 m/s, and the distance from NE crater to the station of 480 m, which is almost same as the distance from SW crater. We estimate the explosion source depth by using the same method and model as shown in Chapter 5. The result shows that the depths are estimated to be 8.3-104.7 m. This result shows the almost same magma level as estimated from the analysis of data in September 2016 (72.9 ± 42.8 m). The estimated magma level and our visual observation suggest that these depths are required for infrasound to be observed on the ground at Stromboli volcano.

We next conduct moment tensor inversion by using the data in June 2015. Due to the natural frequency of the short-period seismometers of 2 Hz but in order to analyze low frequency waves that are not affected by heterogeneous structure, we apply a Butterworth filter of 0.2-0.5 Hz (higher frequency part of the VLP band) to seismic signals. Before applying the filter, the response of a broadband seismometer with a natural frequency of 0.033 Hz is convoluted to the seismograms at short-period sensors. We select the events by using a threshold of the amplitude at UD component of PZT of 0.5 μm/s. The number of events is 181. The waveform at each station is stacked to improve the signal-to-noise ratio. Figure 6.4 (a) shows the distribution of the waveform residuals at 600 m a.s.l. calculated by equation (3.10) for the stacked waveforms. The error distribution shows the source grids just below the Sciara del Fuoco have lower errors, but the source grids just below C or NE crater also show lower errors. Figure 6.4 (b) compares the error distribution at 600 m a.s.l. calculated by using the data at 0.2-0.5 Hz in September 2016. Note that the errors are stacked by using all data of errors in the 103 events. A source grid with a lower error can be also seen in the north-west part of the point source region. The comparisons of the error distribution and the coverage of seismic stations show that the optimal location in the 2015 result is shifted to 320 m northwest of the 2016 result. The region of hot color showing lower errors in Figure 6.4 (a) is larger than the one in Figure 6.4 (b), which is consistent with the synthetic test results in Section 3.3.3. Figure 6.4 (c) illustrates an example of source mechanism solution in the lower error region in Figure 6.4 (a). The result shows the dominance of the diagonal moment tensor components, with the ratios of amplitude in eigenvectors of 0.89:1.11:3.0. The differences in the source location and mechanism between the results in 2015 and 2016 may not be due to a temporal change but the coverage of seismic stations.

We apply our relative hypocenter determination method to precisely determine the source location around a master event. The master event location is set to be the source grid where the waveform residual is minimum in September 2016 because the centroid is more constrained than the one determined by using the data in June 2015 (Figure 6.4). We set the time window width of deconvolution waveforms for calculating CCFs as 2.5 s by examining the trade-off between the time window width and the station pairs. This time window may correspond to the one around the maximum amplitude in the seismograms. Figure 6.5 (a) illustrates the relative source distribution of 0.2-0.5 Hz seismicity. The result shows that the relative source locations are distributed with the range of about 120 m in horizontal and about 60 m in depth in the main cluster. During the observation period, 9 events at NE crater and 5 events at SW crater in the 181 events could be detected by the thermal cameras and the infrasonic sensors of University of Florence (Valade et al., 2016). Figure 6.5 (b) compares the source locations with the surface phenomena. A slight difference in lateral locations that correlate with the eruptive craters is detected. This implies the possibility of different pressure sources that trigger the explosions at two different conduits elongating beneath SW and NE craters.

To examine the deconvolution waveforms in detail, we select 30 events that is considered to be related to the explosions at SW and NE craters. The northeast and southeast events are selected from the earthquakes locating at the northeastern and southeastern parts, respectively, in the concentrated 181 earthquakes (Figure 6.6). The systematic change in the deconvolution waveforms may be important to reflect differences in locations and source processes in the shallow system at Stromboli volcano. The stacked deconvolution waveforms are remarkably different at several seconds before/after the main peaks. In order to evaluate how much the difference contributes to the source distribution, we change the time window width for calculating CCFs from 2.5 s to 3.0 s, 5.0 s, and 10.0 s. We also change the threshold of the correlation coefficient from 0.90 to 0.80 to obtain lag times from many station pairs. Figures 6.7 (a), (b) and (c) show the source distribution of 30 events in SW group and 30 events in NE group which are separated based on the results in Figure 6.5 (a) and Figure 6.6 (a) for the time window width of 3.0 s, 5.0 s, and 10.0 s, respectively. The results show that the sources are clearly separated into two clusters but the larger time window widths lead to large source location errors (14.4-105.6 m in EW, 19.4-102.0 m in NS, and 23.2-118.6 m in UD directions for the time window width of 10.0 s). The comparison of the source distributions between a short time window and a long time window suggests that the centroids within a limited time are almost constant but the ones for a longer time reflect the difference in the

source processes between below SW crater and NE crater. Since the long time window includes the seismic signals excited both before and after the onset of an explosion, it may be difficult to discuss the temporal change in the sources in detail.

6.2 Dynamics of small repetitive eruptions at Stromboli volcano

6.2.1 Explosion source and VLP source

We have determined the explosion source and VLP source by using the data at the very-near-field network. Here, we compare these source locations with a conduit model as inferred from the data of effusive eruptions in 2007 and 2014 (Ripepe et al., 2015; Valade et al., 2016). The authors model the drainage process using a cylinder magma reservoir confined between the effusive vents and the crater terrace from analyses of the effusive volume, volcanic deformation and satellite observations. The magma volume resident in the reservoir is expressed by the total erupted volume of magma and the effusion rate that is controlled by gravitational drainage and steady magma supply rate from depth. In this case, the magma volume resident in the reservoir can be converted to the magma level in the reservoir by assuming the radius of the reservoir with magma vesicularity. For the 2007 effusive eruption, the effusive vent is 400 m a.s.l.. Assuming the radius of the reservoir of 95 ± 5 m and the vesicularity range of 0.14-0.45 (Landi et al., 2009), Ripepe et al. (2015) estimated the magma level above the effusive vent of 286-363 m, which is equivalent to the depth of 7-84 m from the crater. For the 2014 effusive eruption, the effusive vent is 670 m a.s.l.. Valade et al. (2016) estimated the magma level above the effusive vent of 47 ± 10 m, which is equivalent to the depth of 43-63 m. The explosion source depth estimated in this study (72.9 ± 42.8 m, assuming $\alpha =$ 3500 m/s and $c' =$ 708 m/s) is almost same depth as the boundary between the reservoir and the conduits. Also, the VLP (0.05-0.2 Hz and 0.2-0.5 Hz) source, whose elevation is 580-660 m a.s.l. (the depth of 110-190 m) is located at a shallower part of the magma reservoir.

6.2.2 Propagation velocity of magma/gas motions

In Chapter 5, we estimated the propagation velocities of magma/gas from the VLP source to the explosion source for individual events, which is considered as a slug ascent speed in the previous studies. Our result shows that the propagation velocity is estimated to be still much higher than the theoretical value of a slug ascent (Batchelor, 1967). This suggests that we need to reconstruct the eruption model. Recently, a new model explaining fast bubble ascent was presented from an

analogue investigation of bubble-driven deformation in an elastic conduit (Manta et al., 2019). They show that the combination of an elastic conduit with a large volume of gas may develop of a new type of slug that has a larger head and taper towards the tail (defined as “super slug”), which causes a much higher propagation velocity and large inner pressure compared with ordinary slugs. When a large slug ascends, the conduit expands due to large pressure at the top of the slug, which makes a super slug accelerate. This new model may describe the characteristics of the observation values, but quantitative comparison between the laboratory setting and in-situ rock condition is necessary to conclude that such a super slug exists.

Propagation of pressure waves in the magma-filled conduit (Tameguri et al., 2002) is another interpretive model to explain the fast propagation velocity. At Sakurajima volcano, the migration velocity estimated from the time difference between the initial seismic expansion and the air shock generation is 1.4-1.9 km/s (Tameguri et al., 2002). This is much larger than our estimated propagation velocity (30.6 ± 13.4 m/s, assuming $\alpha = 3500$ m/s and $c' = 708$ m/s). However, pressure wave velocities vary depending on the amount of bubbles or solid phase, and temperature of magma inside the conduit. We need to consider these material conditions of magma to interpret the propagation velocity.

6.2.3 Migration of VLP source

This study as well as the previous studies examine the initial motion of VLP signals by focusing on the remarkable onsets that could be seen around 3-5 s before the eruption onsets to measure the propagation velocity. However, we found several events that have a little large amplitude phase 5-15 s before the onset of the large VLP phase at 0.05-0.2 Hz. The amplitude of this phase is larger than seismic noise. Figure 6.8 shows causal-filtered waveforms that have a preceding small phase. Note that the lapse time of the maximum amplitude of acoustic signal is set to be 60 s. We detect 21 events that have this preceding phase from 45 events on 26 September. The timing of this phase is about 10-20 s before the onset of explosions, which is consistent with the timing of a drastic acceleration of deformation detected by tilt sensors (Genco and Ripepe, 2010). Figure 6.9 (b) plots the particle motions of noise part and the preceding phase which are shown in Figure 6.9 (a). The particle motions of the preceding phase point to the region close to the VLP source determined by moment tensor inversion. The particle motions of seismic noise show different directions from those of the preceding phase. This suggests that a volumetric change (for example, due to magma/gas intrusion) occurs several tens of seconds before an explosion. Figure 6.10 (b) plots the particle

motions of the main VLP phase which is shown in Figure 6.10 (a). The particle motions also point to the region close to the VLP source. However, the inflation part in the main phase at ST3 points a little eastward compared with the inflation part in the preceding phase and the contraction part in the main phase. This suggests that the VLP seismic source location changes with time.

To examine the spatio-temporal changes in VLP seismic source before and after explosions, the semblance analysis (Kawakatsu et al., 2000) is performed for different time sections of the VLP seismogram. Figure 6.11 (a) illustrates the time division of the waveform. The lapse time of the maximum amplitude of acoustic signal is set to be 60 s, which almost represents the occurrence time of eruption. We divide the waveforms into four time sections, Preceding phase, Main phase-1 (from the onset of VLP phase to the onset of phase above 1 Hz: about 55-60 s), Main phase-2 (60-70 s), and Main phase-3 (70-80 s). We analyze the 103 VLP events for Main phase-1, Main phase-2, and Main phase-3. For Preceding phase, we analyze 21 events occurring on 26 September. Figures 6.11 (b) and (c) show the results of the semblance analysis for Preceding phase and Main phase-1. The results show that the source locations move eastward toward the crater that generate an explosion. The mean semblance values (S_3) are estimated to be 0.70 and 0.74, respectively. The eastward migration may indicate a preparation process of explosion: magma/gas migration or propagation of pressure waves as a preparation. Assuming the migration distance of 100 m and the migration time of 5-15 s, we estimate the propagation velocity of 6.7-20 m/s. These values are still higher than the theoretical slug ascent velocity (Batchelor, 1967). However, this migration is horizontal so that it is difficult to directly compare the estimated propagation velocity with the theoretical one predicted from a slug model in a vertical conduit. Figures 6.12 (a) and (b) illustrate the results of the semblance analysis for Main phase-2 and Main phase-3. The results illustrate that the source locations move westward and back to those of Preceding phase during the explosions. The mean semblance values (S_3) are estimated to be 0.75 and 0.78, respectively. The migration following the explosions (from Main phase-1 to 2) is similar to the downward migration of the VLP source observed at Erebus volcano (Rowe et al., 1998). This downward migration was interpreted as a nondestructive lossy resonance or nonlinear fluid-flow excitation within the shallow magmatic system. However, the Fourier spectrum of a velocity seismogram in Figure 2.2 (d) illustrates no prominent overtone modes at low-frequency bands. Therefore, the migration in this study may not be explained by a resonance process. Alternatively, the migration process may indicate the propagation of a fluid flow or a pressure wave which are caused by a reaction force of an explosion. In particular, the semblance result for Main phase-2 illustrates that the source locations are separated

into two clusters. Compared with the results of the moment tensor inversion, 53 out of the 63 events indicated by the blue circle in Figure 6.12 (b) are determined to be location (i) estimated from the moment tensor inversion. 26 out of the 40 events indicated by the gray circle in Figure 6.12 (b) are determined to be location (ii) by the moment tensor inversion. The comparison indicates that the difference between location (i) and (ii) is caused by the difference in gas dynamics during or after the explosions. The difference in absolute locations between the semblance and moment tensor inversion analyses may be due to that the semblance analysis does not assume the source mechanism arbitrariness.

6.2.4 Dynamic process of small explosions at Stromboli volcano

We describe the Strombolian eruption process for tens of seconds before and after an onset of eruption by considering the obtained seismic and acoustic data results. Figure 6.13 summarizes the source locations of eruption earthquakes with time on the geometry of the magma reservoir that is based on the cylinder magma reservoir model (Ripepe et al., 2015). The source locations are the centroids of the VLP and LP earthquakes, which represent the center of pressure source.

About 10-20 s before the onset of an explosion, a pressure source exciting small VLP seismic waves (Preceding phase) is located at about 200-250 m west of the crater area. This may be an initiation of magma/gas movement. About 5 s before the onset of eruption, the pressure source moves eastward to the crater, exciting large VLP seismic waves (Main phase-1) and LP (0.5-1.0 Hz) seismic waves. Then, an explosion occurs, exciting higher frequency seismic (> 1 Hz) and acoustic waves at the top of magma level in the reservoir. During the eruption, the pressure source (VLP) migrates westward, and moves back to almost the same source location of the preceding phase. These pressure source locations are detected as the centroids of seismic sources. Considering these pressure sources are located within the shallow magma reservoir, we infer that these migrations are caused by pressure disturbances associated with fluid flow and/or pressure waves in magma which are probably caused by migration of the gas accumulated in the top of magma reservoir, a reaction force and withdrawal of magma by the explosion, and/or a recovery process of magma in the shallow magma reservoir.

6.3 Future perspectives

In this study, we analyzed the seismic and acoustic signals associated with small explosions at

Stromboli volcano. We mainly used the high quality data with high signal to noise ratios recorded at the very-near-field stations. Temporary observations with dense geophysical sensors enable us to accurately estimate the source location of eruption earthquakes or magma/gas motions in the conduit. However, we analyzed the data of only three days in 2015 and five days in 2016 so that it is difficult to discuss the temporal change in the seismic source. Analyzing the data at very-near-field network in long observation periods is necessary to clarify the relation between the magma level and the activity strength. For example, previous studies (Ripepe et al., 2015; Valade et al., 2016) reported that the relative changes of VLP source tracked by calculating the orientation of the ground displacement particle motion vector are associated with the changes in the topographic elevation of the craters during and after the flank effusive eruptions in 2007 and 2014. Accurate hypocenter determination may be helpful to track the absolute magma level. Observations in long terms or other periods may record not only normal Strombolian eruptions but also effusive eruptions or large eruptions such as “major explosions” and paroxysms (Harris and Ripepe, 2007). Analyses of these data may enable us to reveal the eruption transition process or the prediction of these unusual eruptions.

By analyzing the data at the very-near-field network, we showed that small error/difference in the measured values may significantly affect the analysis results. Careful analyses of the observation data are extremely important. In addition, the accuracy of the assumed parameters (seismic velocity structure and a sound speed inside the conduit) is quite important. For example, previous studies on moment tensor inversion of LP earthquakes (e.g. Bean et al., 2008; Trovato et al. 2016) demonstrated that overly simplified velocity structure can have a detrimental effect on the inversions. When the effects of near-surface structures are not taken into account, the solutions with incorrectly oriented source geometries, spurious single forces or incorrect source time functions may be obtained. The examination of the effects of near-surface structures for moment tensor inversion of VLP signals should be conducted in the future. The shallow structure from depths of several tens of meters from the surface to 4 km b.s.l. at Stromboli volcano has been investigated by small-aperture array measurements of the tremor (Chouet et al., 1998) and an active seismic experiment using air gun shots (Patanè et al., 2017). However, it may be necessary to further improve the resolution of the results for the near-surface structures. Active shot experiments at dense seismic observation network and interferometry analyses (e.g., Onizawa et al., 2002) may contribute to understand the near-surface structures. Also, ambient noise cross-correlation functions can estimate the velocity and scattering/intrinsic absorption parameters of Rayleigh waves (Hirose

et al., 2019). This analysis may be useful to image small-scale heterogeneous structures in the shallow part of volcano. These analyses of near-surface structures may enable us to improve the results of hypocenter determination or moment tensor inversion of eruption earthquakes at Stromboli volcano.

In Chapter 6, we succeeded in determining the source location of eruption earthquakes which correlates with the location of the crater where the surface phenomena are detected. At volcanoes with multiple craters like Stromboli volcano, it is important to accurately determine the source location for understanding the transition of the eruptive crater and the structure of the conduits. For example, there are two craters at Sakurajima volcano in Japan, the Minamidake summit crater, and the Showa crater located at the eastern flank of the Minamidake. Since 1955, Frequent Vulcanian eruptions have occurred mainly at Minamidake crater. Then, the frequent Vulcanian eruptions have occurred mainly at the Showa crater in 2006-2017, whereas the main activity of the Vulcanian eruptions moved back to the Minamidake crater in 2018 (Iguchi et al., 2019). By analyzing the seismic data associated with the eruptions at both of the craters and applying our relative source location method, we may be able to understand these transition processes, the structure of bifurcation of the conduits. This will enable us to understand the dynamics of Vulcanian eruptions.

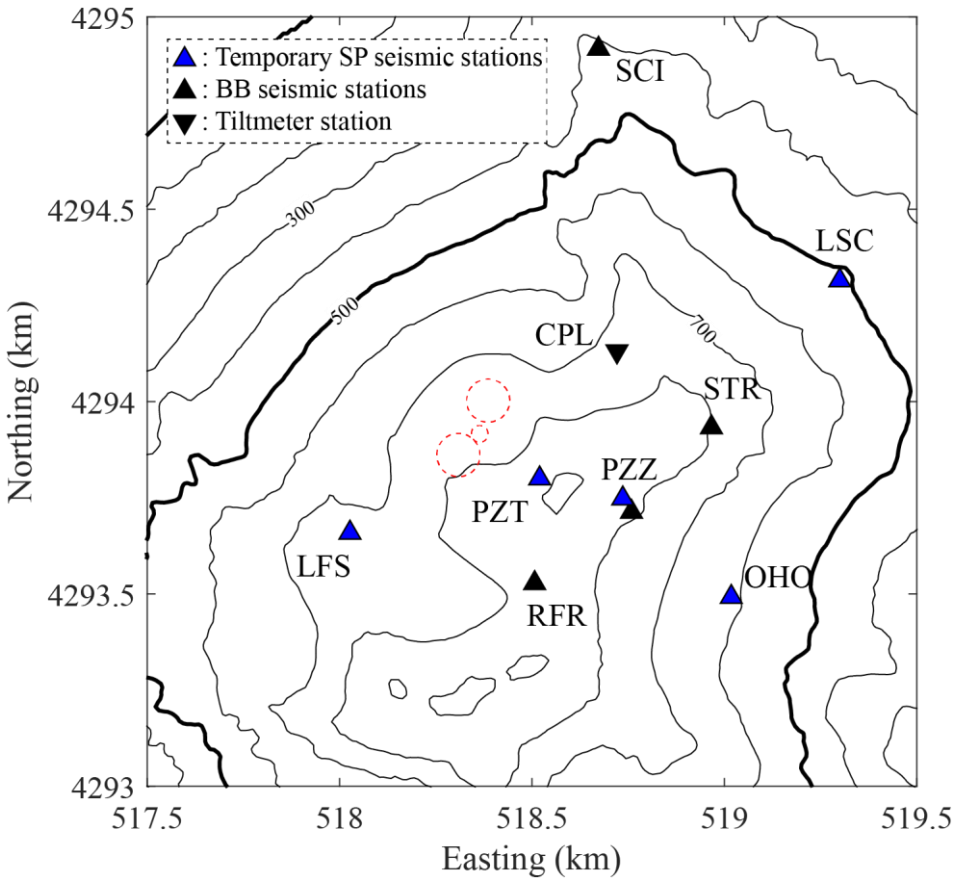

Figure 6.1 Spatial distribution of seismometers and a tilt sensor in June 2015. The symbols in this figure are listed in the upper left part of this panel. At the broadband seismic station PZZ, an infrasonic sensor is also deployed and we analyze these data.

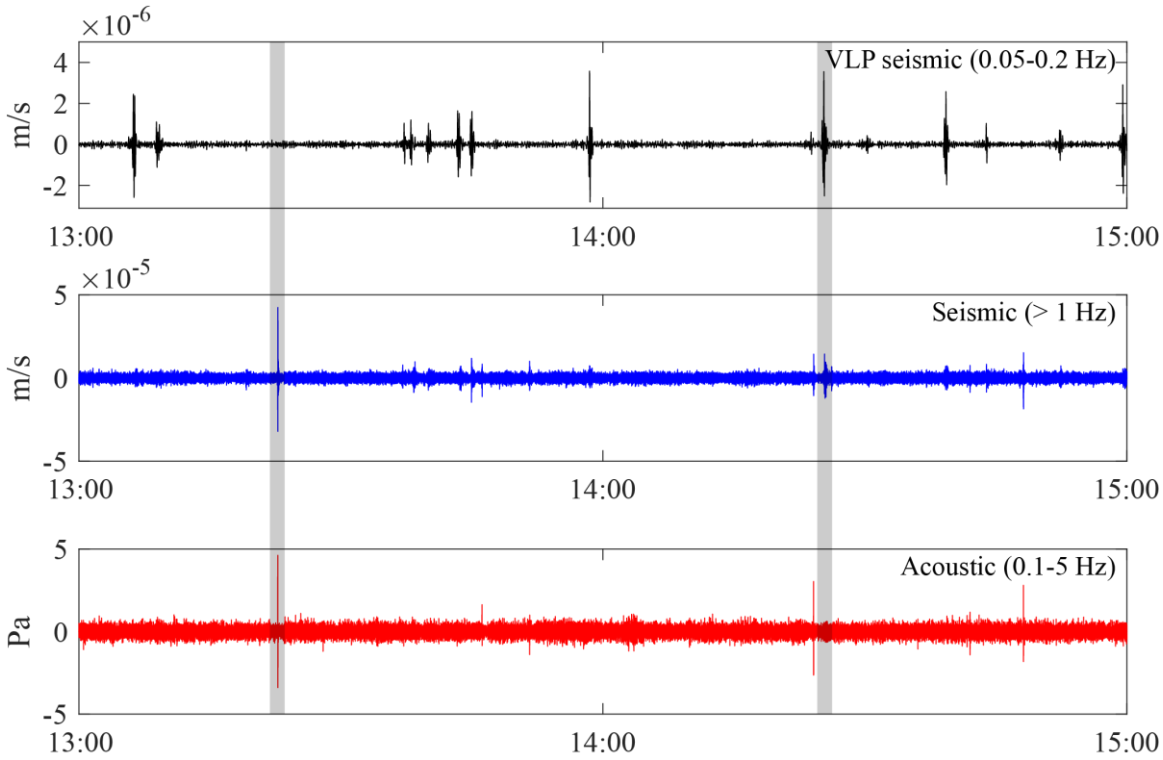

Figure 6.2 Velocity seismogram at 0.05-0.2 Hz (VLP) and above 1 Hz at UD component of PZZ, and infrasound at PZZ from 13:00 to 15:00 on 8 June. The deep shaded range indicates an example of the activity with unclear VLP signal and clear seismic (> 1 Hz) and acoustic (0.1-5 Hz) signals. The light shaded range indicates an example of the activity with clear seismic signals (VLP band and above 1 Hz) and unclear acoustic signals.

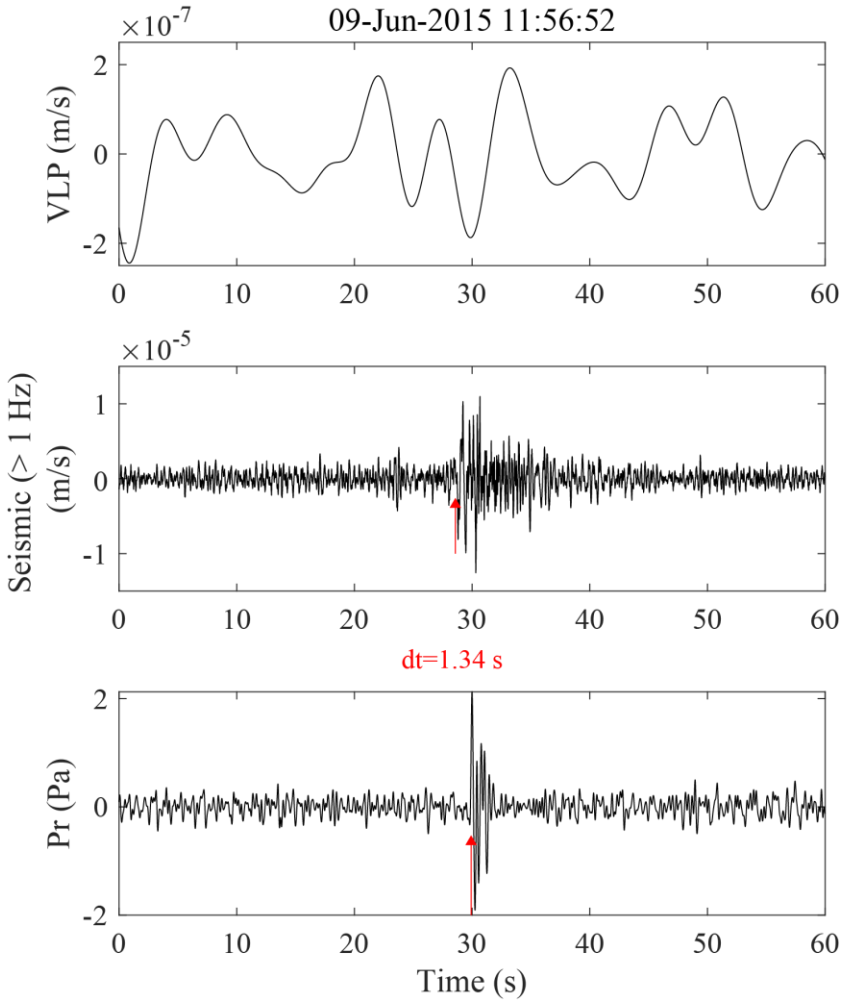

Figure 6.3 An example of seismic and acoustic signals indicating the activity with unclear VLP signal and clear seismic (> 1 Hz) and acoustic signals. The red arrows indicate the onset of seismic (> 1 Hz) and acoustic signals. The time difference of the two onsets is 1.34 s.

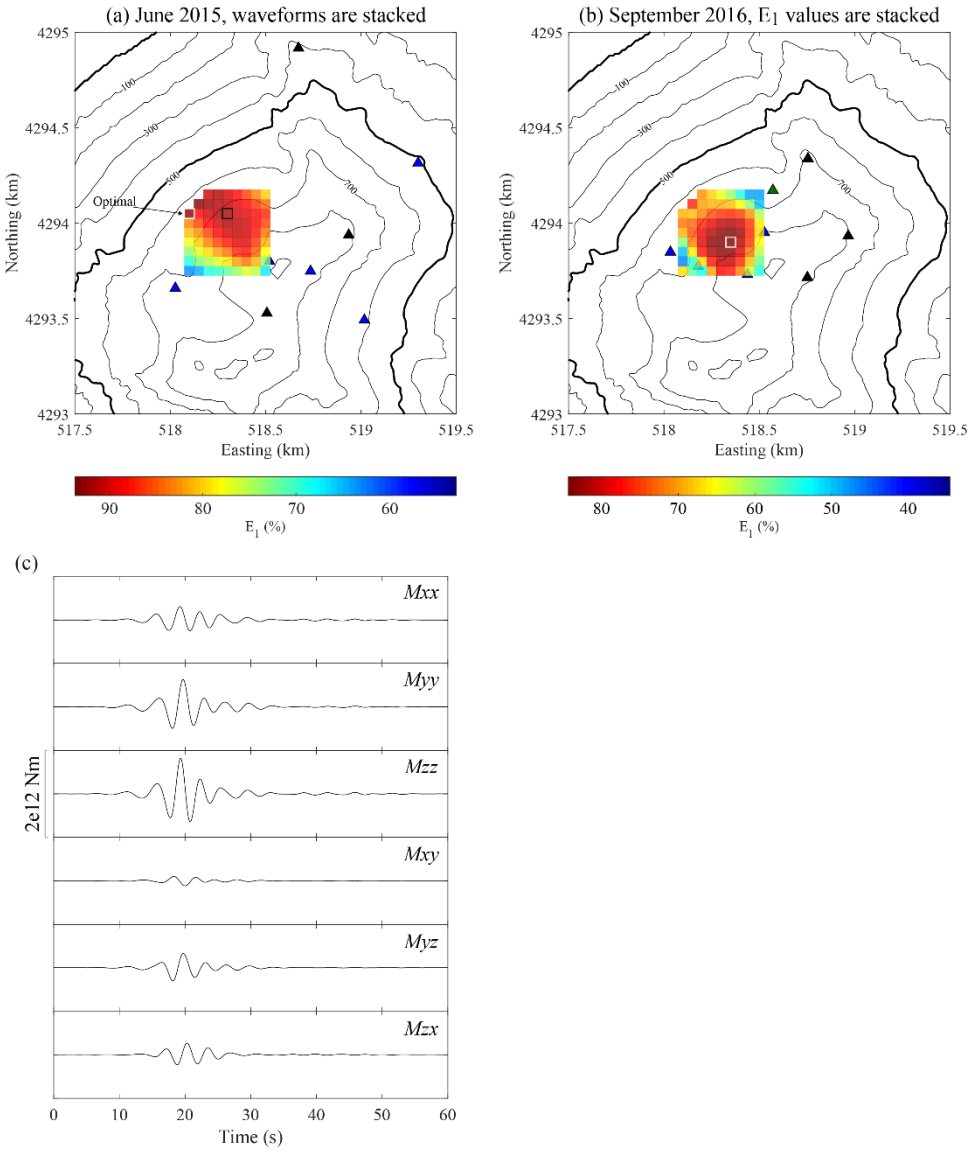

Figure 6.4 (a) Distribution of the error values of waveforms (E_1) estimated by the moment tensor inversion of seismic signals at 0.2-0.5 Hz frequency band in June 2015. The figure shows the inversion result of stacking data. The white square shows the location where the residual of waveforms is minimum. The black triangles show broadband seismic stations and the blue triangles illustrate short-period seismic stations. (b) Similar to Figure 6.4 (a) by using the data in September 2016. The error values are averaged by stacking the error values of all events. The black triangles show broadband seismic stations and the blue and green triangles illustrate temporary broadband seismic stations. (c) Moment tensor solution at the source grid shown in a black square in Figure 6.4 (a).

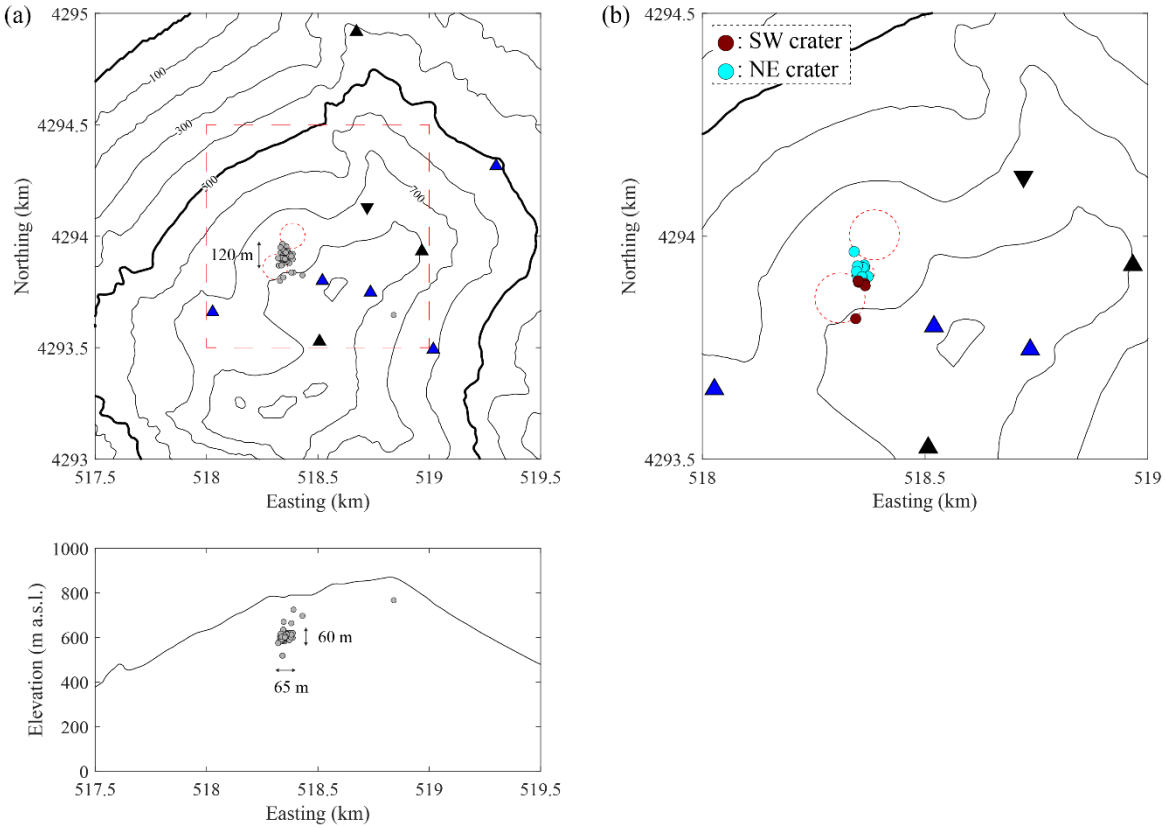

Figure 6.5 (a) Relative source distribution of the seismic signals at 0.2-0.5 Hz frequency band in June 2015, shown in gray circles. The black upward triangles show broadband seismic stations. The blue triangles illustrate short-period seismic stations. The black downward triangle shows a tilt sensor station. The red dashed circles are the locations of the craters. (b) Zoom up of the region shown in a red dashed square in Figure 6.5 (a). This figure compares the source locations with the locations of surface phenomena such as infrasound or infrared. The brown circles show the eruption events at SW crater, and the light blue circles show the eruption events at NE crater.

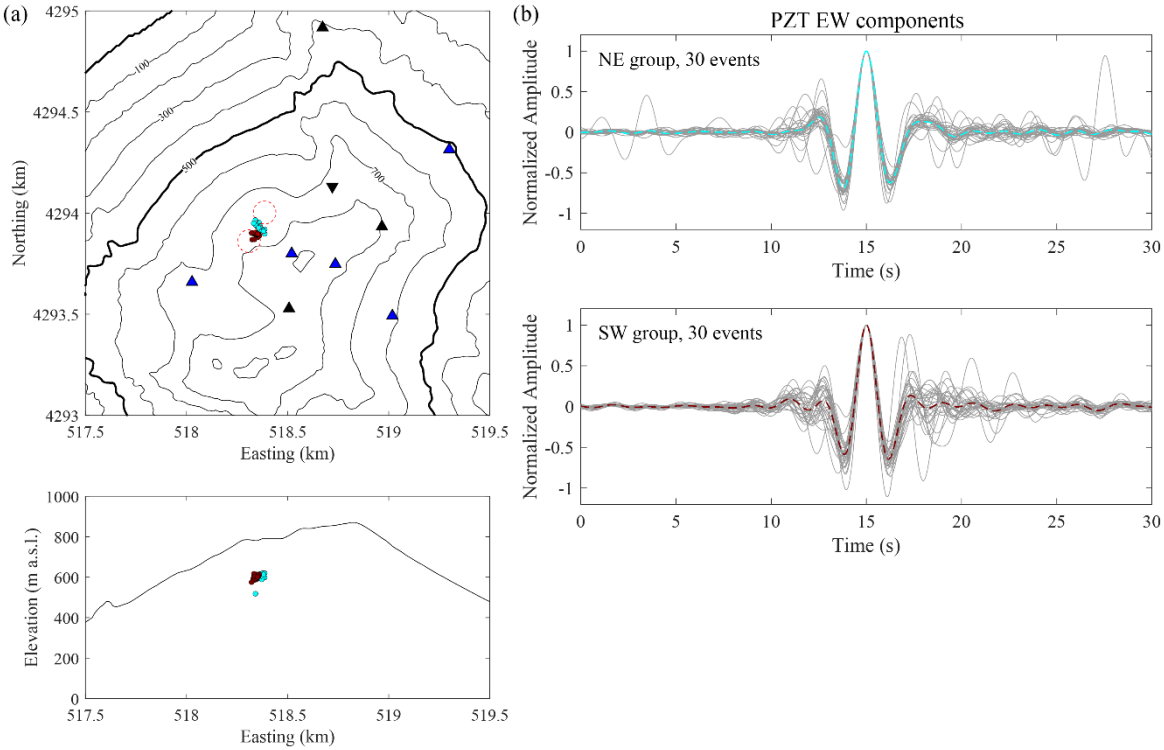

Figure 6.6 (a) Grouping of NE cluster and SW cluster by using the source location result in Figure 6.5 (a). The brown circles show the seismic events in SW group, and the light blue circles show the seismic events in NE group. Each group includes 30 events. The black upward triangles show broadband seismic stations. The blue triangles illustrate short-period seismic stations. The black downward triangle shows a tilt sensor station. The red dashed circles are the locations of the craters. (b) Comparison of stacking of deconvolution waveforms between NE group and SW group. The light blue and brown dashed lines illustrate the mean of the stacking. These deconvolution waveforms are normalized by their maximum amplitudes.

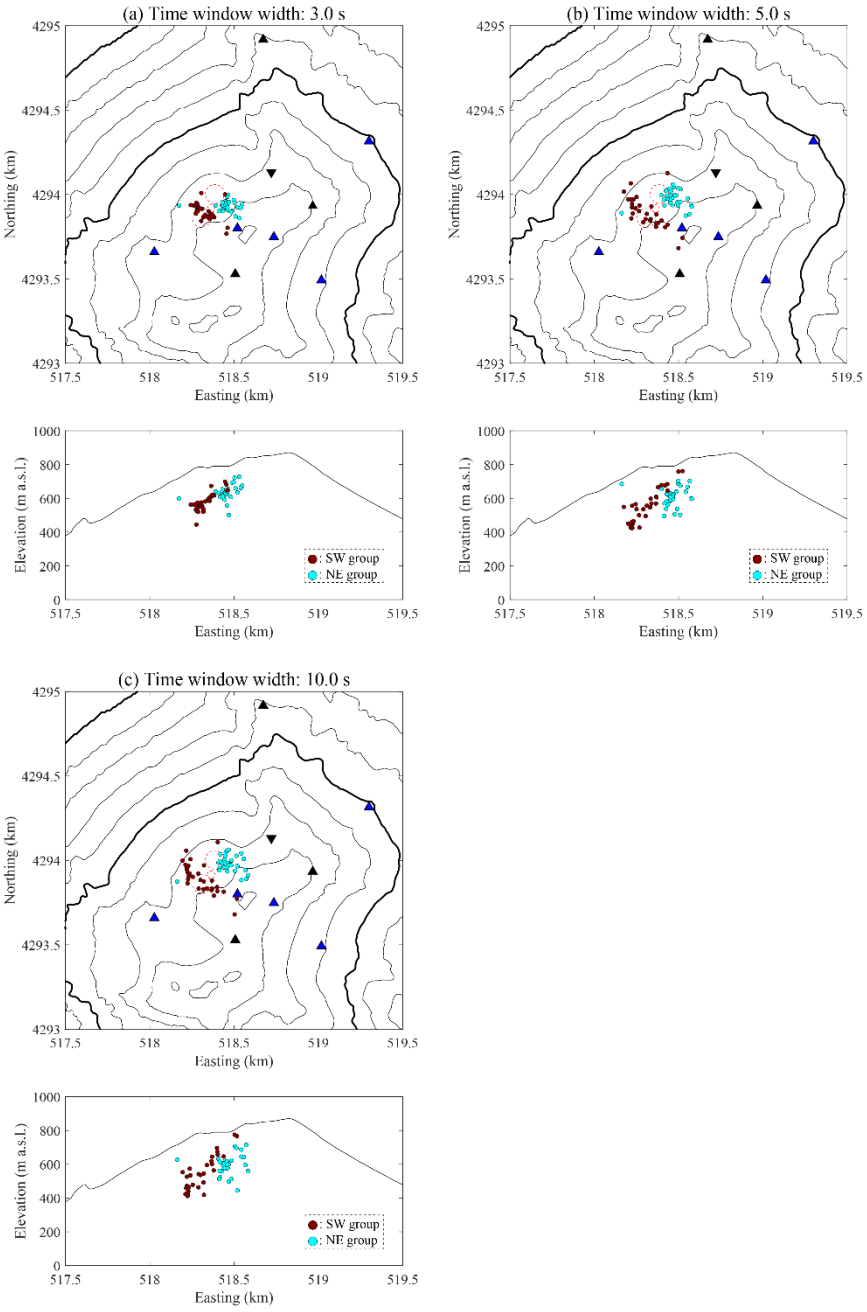

Figure 6.7 (a) Comparison of source distribution of 30 events in SW group and 30 events in NE group in Figure 6.6 (a) for the time window width of deconvolution waveforms for calculating CCFs of 3.0 s. The brown circles show the seismic events in SW group, and the light blue circles show the seismic events in SW group. The black upward triangles show broadband seismic stations. The blue triangles illustrate short-period seismic stations. The black downward triangle shows a tilt sensor station. The red dashed circles are the locations of the craters. (b), (c) Similar to Figure 6.7 (a) for the time window width of 5.0 s and 10.0 s, respectively.

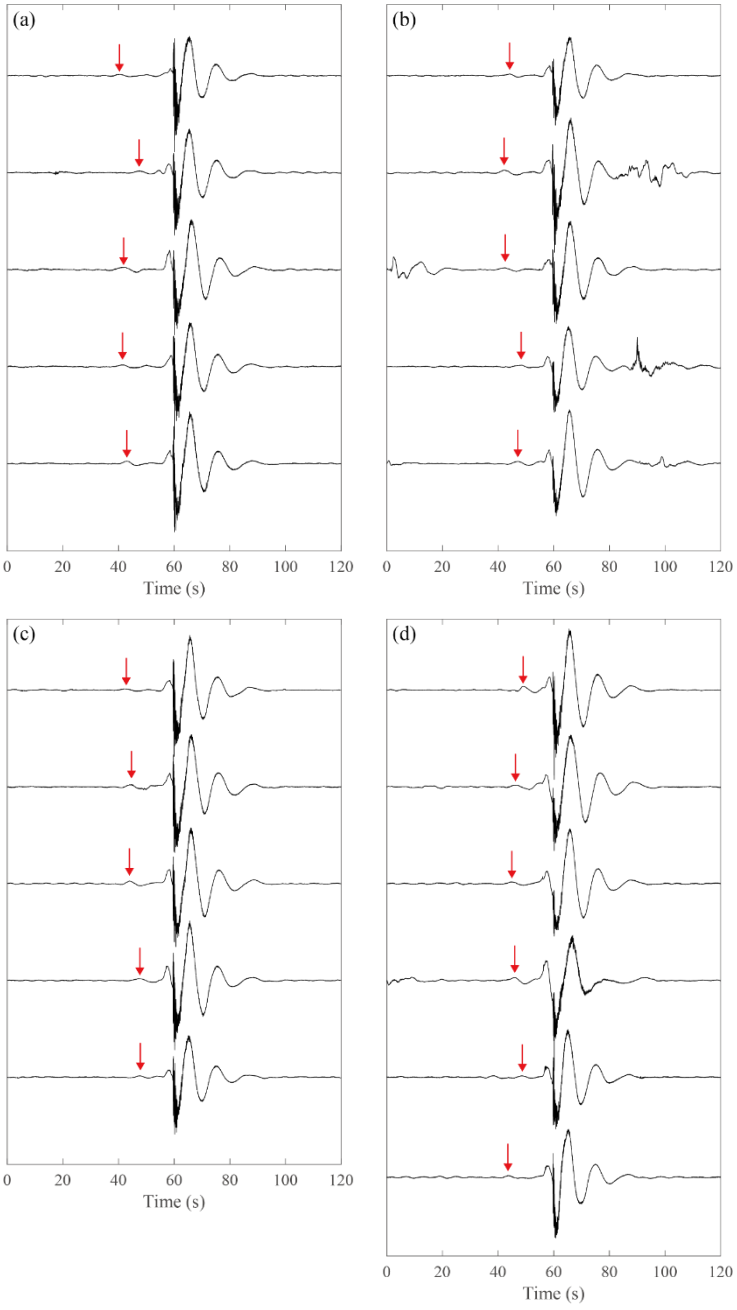

Figure 6.8 The causal-filtered seismic waveforms at 0.05-0.2 Hz at ST1. These events have a small phase before the main phase of VLP signals. Red arrows indicate the peaks of the preceding phase which are manually detected. Note that the maximum amplitude of acoustic signal is set at 60 s.

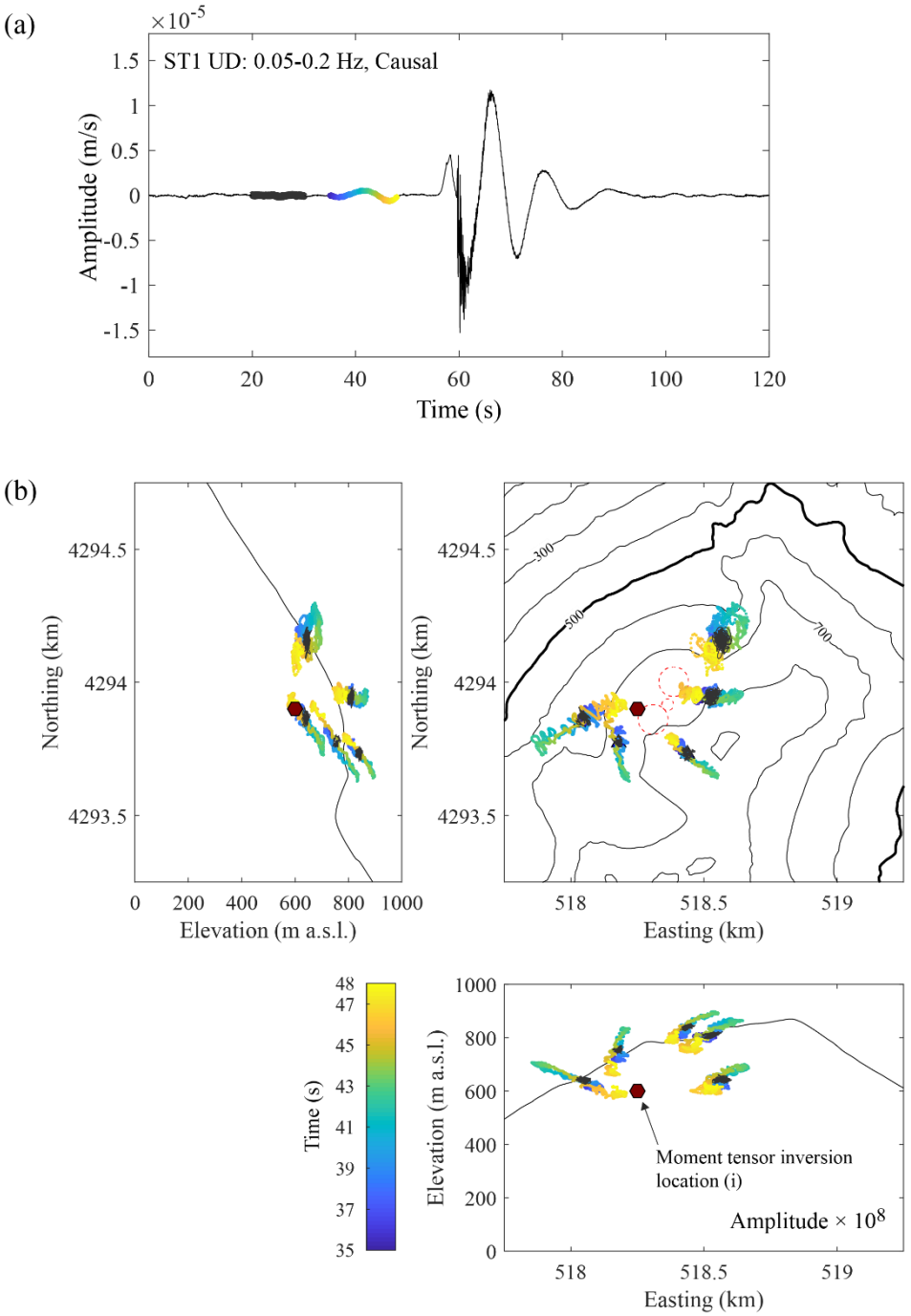

Figure 6.9 (a) VLP seismogram at UD component of ST1. The thick black line shows the noise part and the colored line shows the preceding phase. These are used to plot the particle motions. (b) Particle motions of the noise part (black) and the preceding phase. The color indicates the elapsed time. The amplitudes are amplified at the scale listed in the lower right.

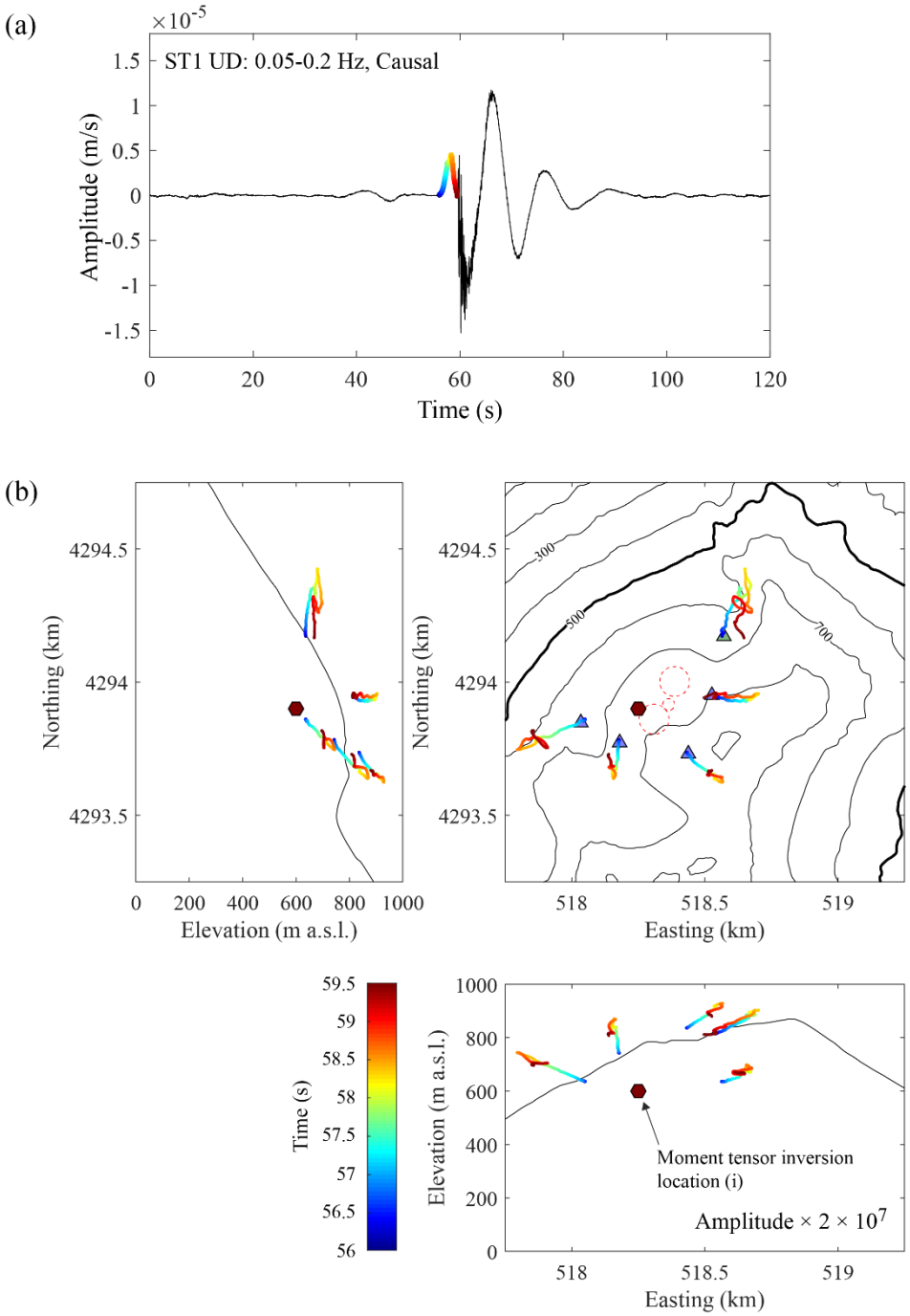

Figure 6.10 (a) VLP seismogram at UD component of ST1. The colored line shows the preceding phase to plot the particle motions. (b) Particle motions of the main VLP phase. The color indicates the elapsed time. The amplitudes are amplified at the scale listed in the lower right.

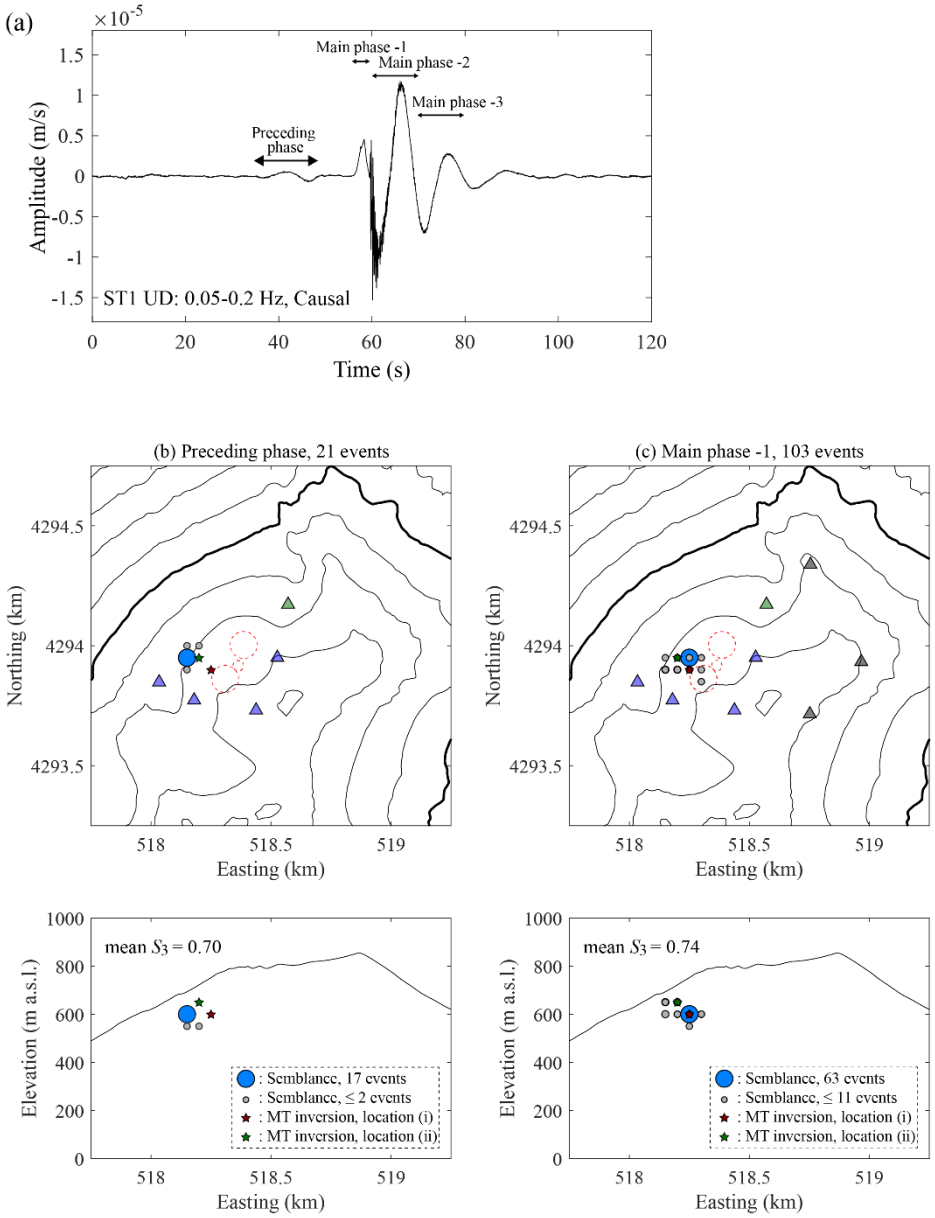

Figure 6.11 (a) VLP seismogram at UD component of ST1 and four time sections. (b) Source distribution of VLP seismic events determined by the semblance analysis for Preceding phase. The methods and number of events are listed in EW cross section. (c) Similar to Figure 6.11 (b) for Main phase-1.

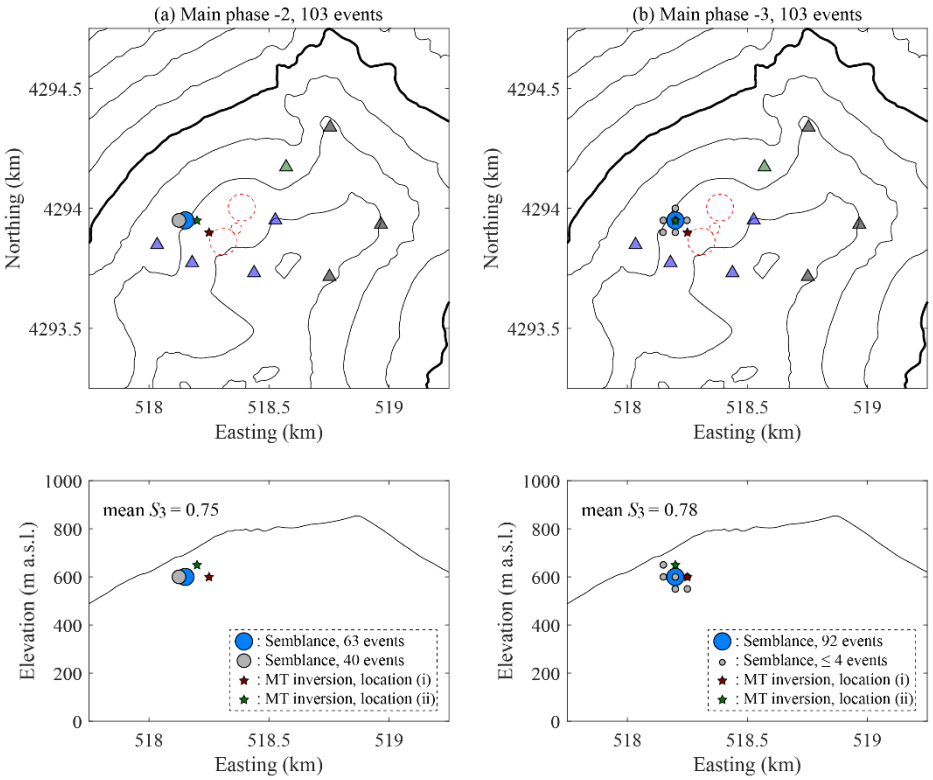

Figure 6.12 (a) Source distribution of VLP seismic events determined by the semblance analysis for Main phase-2. The methods and number of events are listed in EW cross section. (b) Similar to Figure 6.12 (a) for Main phase-3.

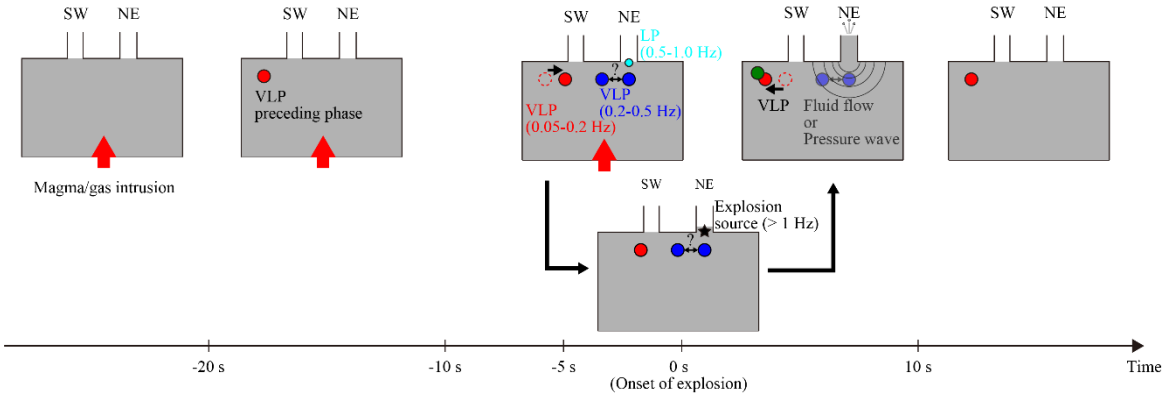

Figure 6.13 Interpretive sketch of the temporal evolution of the source locations and the source migration in the case of an explosion at NE crater.

Chapter 7

Conclusions

We have analyzed the seismic and acoustic signals associated with small repetitive eruptions at Stromboli volcano. We estimated the source location of eruption earthquakes and motions of magma/gas in the conduit, which are the most basic and important information to develop the model of Strombolian eruption. Analyzing the seismic and acoustic data recorded at only 100-300 m away from the active craters from 24 to 28 September 2016 enabled us to accurately determine these key parameters.

Firstly, we have conducted seismic moment tensor inversion including tilt responses using temporary very-near-field network data at Stromboli volcano. The source locations of VLP (0.05-0.2 Hz) signals associated with small explosions are mainly located at the edge of the crater rim, which are about 200 m away from the eruptive (NE) crater at 600 m or 650 m a.s.l. (depths of 170 m or 120 m). The waveforms of the events in these two source clusters show slightly different amplitude distributions, which are detected only at the very-near-field network. These differences are seen after the onset of acoustic waves. Thus, these two clusters may indicate the difference in the source mechanisms during/after explosions. The seismic sources at 0.2-0.5 Hz (higher frequency part of the VLP band) and 0.5-1.0 Hz (LP band) are located closer to NE crater than the sources for 0.05-0.2 Hz. There are no large generation time differences in the earthquakes at different frequency bands so that these earthquakes are simultaneously excited from different centroids. The source mechanisms of the VLP and LP signals show the dominance of the vertical dipole component of the moment tensor. This suggests volumetric changes at the source regions. The model resolution matrices calculated from the Green's functions show that details of the volumetric changes are not well resolved from the very-near-field observation data. Synthetic tests of network performance show that the distant seismic network does not necessarily contribute to the improvement of the mechanism solutions. Furthermore, the very-near-field network contributes to exactly determine the source locations compared with the distant seismic network with a large number of seismic stations. Synthetic tests of finite source modelling support the reliability of the source locations determined from our very-near-field network data and inaccuracy of the source mechanisms.

Secondly, relative hypocenter determination of VLP (0.05-0.2 Hz) earthquakes was conducted by applying a method which combines the master event method with a deconvolution technique.

The relative VLP source locations around the master event located by the moment tensor inversion in Chapter 3 range about 50 m in horizontal and about 80 m in vertical directions. The source locations concentrated within a distance of 50-80 m have different characteristics from the two source clusters determined by the moment tensor inversion. This implies that the two source clusters obtained from the moment tensor inversion may be separated because of the grid size limitation (50 m), or because the locations of the VLP source move with time.

Thirdly, we have analyzed the seismic and acoustic signals associated with small explosions to estimate the source depth of the explosions and the propagation velocity of magma/gas from the VLP source to the explosion source in the conduit/chamber. By using the arrival time difference between seismic and acoustic signals measured by using the data at the very-near-field network and applying an automatically picking method, the explosion source depth is estimated to be 72.9 ± 42.8 m. The average explosion source depth is consistent with the boundary between the reservoir and the conduits. This is almost same as the results (8.3-104.7 m) estimated from data in June 2015 when the magma level was deep. These depths may be necessary for infrasound to be observed on the ground at Stromboli volcano. The propagation velocity is estimated to be 30.6 ± 13.4 m/s when the VLP source depth is 170 m. Such high-speed of magma/gas motions is estimated from the data at a different station, different model parameters, and different conduit models. The fast propagation may indicate the necessity to modify a gas ascent model that has been often used to explain Strombolian eruptions.

We discussed the spatio-temporal changes in VLP/LP seismic sources before and during/after the explosions. The VLP (0.2-0.5 Hz) seismic sources are distributed beneath SW or NE craters from the deconvolution waveforms for a longer time window, which suggest different pressure sources that trigger the explosions at two different conduits. For VLP signals, a very small phase is detected 10-20 s before the onset of an explosion. This suggests an initiation of magma/gas movement. The pressure source moves eastward to the crater toward the explosion, and then moves back westward to the initial source. These pressure sources migrate because of pressure disturbances caused by migration of the gas accumulated in the shallow part of magma reservoir and a reaction force and withdrawal of magma by the explosion. Then, magma is recovered in the magma reservoir.

This study newly and accurately determines the source location of seismicity associated with small repetitive eruptions and conduit parameters, verifying usefulness and importance of very-near-field observations at active volcanoes. The results obtained from high quality measurements indicate the necessity of redevelopment of the Strombolian eruption model. In addition, we found

that the seismic sources of VLP or LP earthquakes are temporally changed before/during explosions. Moreover, we revealed that not only vertical but also lateral magma/gas movements are quite important to understand the dynamics of explosions at Stromboli volcano. Analyses of long-term data obtained from such an intensive observation near the craters at Stromboli volcano or other volcanoes will help us deepen understanding volcanic activities.

References

Aki, K., and Richards, P.G. (1980), *Quantitative Seismology*, Freeman, New York.

Aoyama, H. (2008), Simplified test on tilt response of CMG40T seismometers, *Bull. Volcanol. Soc. Jpn.*, 53, 35-46.

Aoyama, H., and Oshima, H. (2008), Tilt change recorded by broadband seismometer prior to small phreatic explosion of Meakan-dake volcano, Hokkaido, Japan, *Geophys. Res. Lett.*, 35, L06307, doi:10.1029/2007GL032988.

Arámbula-Mendoza, R., Reyes-Dávila, G., Vargas-Bracamontes, D. M., González-Amezcua, M., Navarro-Ochoa, C., Martínez-Fierros, A., and Ramírez-Vázquez, A. (2018), Seismic monitoring of effusive-explosive activity and large lava dome collapses during 2013–2015 at Volcán de Colima, Mexico, *J. Volcanol. Geotherm. Res.*, 351, 75–88, https://doi.org/10.1016/j.jvolgeores.2017.12.017.

Aster, R., Zandomeneghi, D., Mah, S., McNamara, S., Henderson, D., Knox, H., and Jones, K. (2008), Moment tensor inversion of very long period seismic signals from Strombolian eruptions of Erebus Volcano, *J. Volcanol. Geotherm. Res.*, 177, 635-647.

Auger, E., D'Auria, L., Martini, M., Chouet, B., and Dawson, P. (2006), Realtime monitoring and massive inversion of source parameters of very long period seismic signals: An application to Stromboli Volcano, Italy, *Geophys. Res. Lett.*, 33, L04301, doi:10.1029/2005GL024703.

Batchelor, G. K. (1967), *An introduction to fluid dynamics*, Cambridge University Press.

Bean, C.J., Lokmer, I., and O'Brien, G.S. (2008), Influence of near-surface volcanic structure on long-period seismic signals and on moment tensor inversions: simulated examples from Mount Etna, *J. Geophys. Res.*, 113, doi:10.1029/2007jb005468.

Blackburn, E. A., Wilson, L., and Sparks, R.S.J. (1976), Mechanics and dynamics of Strombolian activity, *J. Geol. Soc.*, 132, 429-440.

Braun, T., and Ripepe, M. (1993), Interaction of seismic and air waves as recorded at Stromboli volcano, *Geophys. Res. Lett.*, 20, 65-68.

Burton, M.R., Caltabiano, I., Mure, E., Salerno, G., and Randazzo, D. (2009), SO2 flux from Stromboli during the 2007 eruption: results from the FLAME network and traverse measurements, *J. Volcanol. Geotherm. Res.*, 182, 214-220.

Cas, R.A.S., and Wright J.V. (1992), *Volcanic Succession Modern and Ancient*, 528 pp., Chapman and Hall, New York.

Chouet, B. (1986), Dynamics of a fluid-driven crack in three dimensions by the finite difference method, *J. Geophys. Res.*, 91, 13,967-13,992.

Chouet, B., Saccorotti, G., Martini, M., Dawson, P., De Luca, G., Milana, G., and Scarpa, R. (1997), Source and path effects in the wavefields of tremor and explosions at Stromboli Volcano, Italy, *J. Geophys. Res.*, 102, 15,129-15,150.

Chouet, B., De Luca, G., Milana, G., Dawson, P., Martini, M., and Scarpa, R. (1998), Shallow velocity structure of Stromboli Volcano, Italy, derived from small-aperture array measurements of Strombolian tremor, *Bull. Seismol. Soc. Am.*, 88, 653-666.

Chouet, B., Dawson, P., Ohminato, T., Martini, M., Saccorotti, G., Giudicepietro, F., De Luca, G., Milana, G., and Scarpa, R. (2003), Source mechanisms of explosions at Stromboli Volcano, Italy, determined from moment-tensor inversions of very-long-period data, *J. Geophys. Res*., 108, 2019., http://dx.doi.org/10.1029/2002JB001919.

Chouet, B., Dawson, P., and Martini, M. (2008), Shallow-conduit dynamics at Stromboli Volcano, Italy, imaged from waveform inversions. in Lane, S.J., and Gilbert, J.S. (Eds.), *Fluid Motions in Volcanic Conduits: A Source of Seismic and Acoustic Signals*, *Geol. Soc., London*, *Spec. Publ.*, 307, 57-84.

Chouet, B.A. and Matoza, R.S. (2013), A multi-decadal view of seismic methods for detecting precursors of magma movement and eruption, *J. Volcanol. Geotherm. Res.*, 252, 108-175, doi: 10.1016/j.jvolgeores.2012.11.013.

Davi, R., O'Brien, G.S., Lokmer, I., Bean, C.J., Lesage, P., and Mora, M.M. (2010), Moment tensor inversion of explosive long period events recorded on Arenal volcano, Costa Rica, constrained by synthetic tests, *J. Volc. Geotherm. Res.,* 194**,** 189-200.

De Barros, L., Lokmer, I., and Bean, C.J. (2013), Origin of spurious single forces in the source mechanism of volcanic seismicity, *J. Volcanol. Geotherm. Res.*, 262, 1-6.

Delle Donne, D., Ripepe, M., Lacanna, G., Tamburello, G., Bitetto, M., and Aiuppa, A. (2016), Gas mass derived by infrasound and UV cameras: Implications for mass flow rate, *J. Volcanol. Geotherm. Res.*, 325, 169-178.

Ferrucci, F. (1995), Seismic monitoring at active volcanoes, In McGuire, B. et al. (eds.), *Monitoring Active Volcanoes*, UCL Press, London, 60-90.

Firstov, P.P., Kravchenko, N.M. (1996), Estimation of the amount of explosive gas released in volcanic eruptions using air waves, *Volcanol. Seismol.*, 17, 547-560.

Gaudin, D., Taddeucci, J., Scarlato, P., Harris, A.J.L., Bombrun, M., Del Bello, E., and Ricci, T.

(2017), Characteristics of puffing activity revealed byground-based, thermal infrared imaging: The example of Stromboli volcano (Italy), *Bull. Volcanol.*, 79, 24, doi:10.1007/s00445-017-1108-x.

Genco, R., and Ripepe, M. (2010), Inflation-deflation cycles revealed by tilt and seismic records at Stromboli volcano, *Geophys. Res. Lett.*, 37, L12302.

Giudicepietro, F. et al. (2009), Changes in the VLP seismic source during the 2007 Stromboli eruption, *J. Volcanol. Geotherm. Res.*, 182, 162-171.

Graizer, V. (2006), Tilts in strong ground motion, *Bull. seism. Soc. Am.,* 96, 2090-2102.

Gurioli, L., Colo, L., Bollasina, A., Harris, A.J., Whittington, A., and Ripepe, M. (2014), Dynamics of Strombolian explosions: inferences from field and laboratory studies of erupted bombs from Stromboli volcano. *J. Geophys. Res.*, 119, 319-345, https://doi.org/10.1002/2013JB010355.

Haney, M.M., Chouet, B.A., Dawson, P.B., Power, J.A. (2012), Source characterization for an explosion during the 2009 eruption of Redoubt Volcano from very-long-period seismic waves, *J. Volcanol. Geotherm. Res*., http://dx.doi.org/10.1016/j.jvolgeores.2012.04.018.

Harris, A.J.L., and Ripepe M. (2007), Synergy of multiple geophysical approaches to unravel explosive eruption conduit and source dynamics -A case study from Stromboli, *Chem. Erde*, 67, 1–35.

Hasib, M. (2019), Spectral ratio analyses of seismic and acoustic waves excited by Vulcanian eruptions, *PhD thesis*, Tohoku University, Japan.

Hirose, T., Nakahara, H., and Nishimura, T. (2019). A passive estimation method of scattering and intrinsic absorption parameters from envelopes of seismic ambient noise cross-correlation functions, *Geophys. Res. Lett.*, 46, 3634-3642. https://doi.org/10.1029/2018GL080553.

Iguchi, M. (1994), A vertical expansion source model for the mechanisms of earthquakes originating in the magma conduit of an andesitic Volcano, Sakurajima, Japan, *Bull. Volcano. Soc. Jpn.*, 39, 49-67.

Iguchi, M., Yakiwara, H., Tameguri, T., Hendrasto, M., and Hirabayashi, J.I. (2008), Mechanism of explosive eruption revealed by geophysical observations at the Sakurajima, Suwanosejima and Semeru volcanoes, *J. Volcanol. Geotherm. Res.*, 178, 1-9. http://dx.doi.org/10.1016/j.jvolgeores .2007.10.010.

Iguchi, M., Tameguri, T., Hirabayashi, J., and Nakamichi, H. (2019), Forecasting Volcanic Eruption of Sakurajima Volcano Based on Magma Intrusion Rate, *Bull. Volcano. Soc. Jpn.*, 64, 33-51.

Ishihara, K. (1985), Dynamical analysis of volcanic explosion, *J. Geodyn.*, 3, 327-349.

Ishihara, K. (1990), Pressure sources and induced ground deformation associated with explosive eruptions at an andesitic volcano, Sakurajima Volcano, Japan. In Ryan, M. P. eds, *Magma Transport and Storage*, John Wiley & Sons, 335-356.

Ishii, K, Yokoo, A., Kagiyama, T., Ohkura, T., Yoshikawa, S., and Inoue, H. (2019) Gas flow dynamics in the conduit of Strombolian explosions inferred from seismo-acoustic observations at Aso volcano, Japan, *Earth Planets Sp.* https://doi.org/10.1186/s40623-019-0992-z.

James, M.R., Lane, S.J., and Chouet, B. (2006), Gas slug ascent through changes in conduit diameter: laboratory insights into a volcano-seismic source process in low-viscosity magmas, *J. Geophys. Res.*, 111, B05201, http://dx.doi.org/10.1029/2005JB003718.

James, M.R., Lane, S.J., and Corder, S.B. (2008), Modelling the rapid near-surface expansionof gas slugs in low-viscosity magmas, in Fluid Motions, in *Volcanic Conduits: A Source of Seismic and Acoustic Signals* edited by Lane, S. J. and Gilbert, J.S., *Geol. Soc. Spec. Publ.*, 307, 147-167.

James, M.R., Lane, S.J., Wilson, L., and Corder, S.B. (2009), Degassing at low magma-viscosity volcanoes: Quantifying the transition between passive bubble-burst and Strombolian eruption, *J. Volcanol. Geotherm. Res.*, 180, 81-88.

Jaupart, C. and Vergniolle, S. (1988), Laboratory models of Hawaiian and Strombolian eruptions, *Nature*, 331, 58-60.

Johnson, J., Aster, R., Ruiz, M., Malone, S., McChesney, P., Lees, J., and Kyle, P. (2003), Interpretation and utility of infrasonic records from erupting volcanoes, *J. Volcanol. Geotherm. Res.*, 121, 15-63.

Johnson, J. and Aster, R. (2005), Relative partitioning of acoustic and seismic energy during Strombolian eruptions. *J. Volcanol. Geotherm. Res.*, 148, 334-354.

Jolly, A.D., Kennedy, B., Edwards, M., Jousset, P., and Scheu, B. (2016), Infrasound tremor from bubble burst eruptions in the viscous shallow crater lake of White Island, New Zealand, and its implications for interpreting volcanic source processes, *J. Volcanol. Geotherm. Res.*, 327, 585-603. https://doi.org/10.1016/j.jvolgeores.2016.08.010.

Kamo, K. (1978). Some phenomena before the summit eruptions at Sakurajima Volcano. *J. Volc. Soc. Japan*, 23-53, 64 (in Japanese).

Kanamori, H., Given, J., and Lay, T. (1984), Analysis of seismic body waves excited by the Mount St. Helens eruption of May 18, *J. Geophys. Res*., 89, 1,856-1,866.

Kawaguchi, R., and Nishimura, T. (2015), Numerical investigation of temporal changes in volcanic deformation caused by a gas slug ascentin the conduit, *J. Volcanol. Geotherm. Res.*, 302, 1-10,

doi:10.1016/j.jvolgeores.2015.06.002.

Kawakatsu, H., Kaneshima, S., Matsubayashi, H., Ohminato, T., Sudo, Y., Tsutsui, T., Uhira, K., Yamasato, H., Ito, H., and Legrand, D. (2000), Aso94: Aso seismic observation with broadband instruments, *J. Volcanol. Geotherm. Res.*, 101, 129-154, doi:10.1016/S0377-0273(00)00166-9.

Kieffer, S. (1977), Sound speed in liquid-gas mixtures: Water-air and water-steam, *J. Geophys. Res.*, 82, 2895-2904, doi:10.1029/JB082i020p02895.

Kim, K., Lees, J. M., and Ruiz, M.C. (2014), Source mechanism of Vulcanian eruption at Tungurahua Volcano, Ecuador, derived from seismic moment tensor inversions, *J. Geophys. Res.*, 119, 1145–1164, doi:10.1002/2013JB010590.

Kumagai, H., Nakano, M., Maeda, T., Yepes, H., Palacios, P., Ruiz, M., Arrais, S., Vaca, M., Molina, I., and Yamashina, T. (2010), Broadband seis-mic monitoring of active volcanoes using deterministic and stochastic approaches, *J. Geophys. Res.* , 115, B08303, doi:10.1029/2009JB006889.

Kumagai, H., Palacios, P., Ruiz, M., Yepes, H., and Kozono, T. (2011), Ascending seismic source during an explosive eruption at Tungurahua volcano, Ecuador, *Geophys. Res. Lett.*, 38, L01306, doi:10.1029/2010GL045944.

Landi, P. et al. (2009), Magma dynamics during the 2007 Stromboli eruption (Aeolian Islands, Italy): mineralogical, geochemical and isotopic data, *J. Volcanol. Geotherm. Res.*, 182, 255–268.

Lanza, F., and Waite, G.P. (2018). A nonlinear approach to assess network performance for moment-tensor studies of long-period signals in volcanic settings, *Geophys. J. Int.*, 215, 1352-1367, doi:10.1093/gji/ggy338.

Levander, A.R. (1988), Fourth-order finite-difference P-SV seismograms, *Geophysics*, 53, 1425-1436, doi:10.1190/1.1442422.

Llewellin, E.W., Del Bello, E., Taddeucci, J., Scarlato, P., and Lane, S.J. (2011), The thickness of the falling film of liquid around a Taylor bubble, *Proc. R. Soc.*, 468, 1041-1064.

Lyons, J.J., and Waite, G.P. (2011), Dynamics of explosive volcanism at Fuego volcano imaged with very long period seismicity, *J. Geophys. Res*., 116, B09303. http://dx.doi.org/10.1029/2011JB008521.

Maeda, N. (1985), A method for reading and checking phase times in auto-processing system of seismic wave data, *Zisin=Jishin*, 38, 365-379.

Maeda, T., Takemura, S., and Furumura, T. (2017), An open-source integrated parallel simulation code for modeling seismic wave propagation in 3D heterogeneous viscoelastic media, *Earth, Planets and Space.,*69-102.

Maeda, Y., Takeo, M., and Ohminato, T. (2011), A waveform inversion including tilt: method and simple tests, *Geophys. J. Int.*, 184, 907-918.

Manta, F., Emadzadeh, A., and Taisne, B. (2019). New insight into a volcanic system: analogue investigation of bubble-driven deformation in an elastic conduit. *J. Geophys. Res.*, 124, https://doi. org/10.1029/2019JB017665.

Marchetti, E., and Ripepe, M. (2005), Stability of the seismic source during effusive and explosive activity at Stromboli Volcano, *Geophys. Res. Lett.*, 32, L03307.

Martini, M., et al. (2007), Seismological monitoring of the February 2007 effusive eruption of the Stromboli volcano, *Ann. Geophys.*, 50, 775-788.

Menke, W. (1984), Geophysical Data Analysis: Discrete Inverse Theory, Academic Press, New York.

Metrich, N., Bertagnini, A., Landi, P., and Rosi, M. (2001), Crystallization driven by decompression and water loss at Stromboli Volcano (Aeolian Islands, Italy), *J. Petrol.*, 42, 1471-1490.

Neri, M., and Lanzafame, G. (2009), Structural features of the 2007 Stromboli eruption, *J. Volcanol. Geotherm. Res.*, 182, 137-144.

Nishimura, T., and Hamaguchi, H. (1993), Scaling law of volcanic explosion earthquake, *Geophys. Res. Lett*., 20, 2479-2482.

Ohminato, T., Chouet, B.A., Dawson, P.B., and Kedar, S. (1998), Waveform inversion of very-long-period impulsive signals associated with magmatic injection beneath Kilauea Volcano, Hawaii, *J. Geophys. Res.*, 103, 23,839-23,862.

Ohminato, T., Takeo, M., Kumagai, H., Yamashina, T., Oikawa, J., Koyama, E., Tsuji, H., and Urabe, T. (2006), Vulcanian eruptions with dominant single force components observed during the Asama 2004 volcanic activity in Japan, *Earth Planets Sp.*, 58, 583-593.

Onizawa S., Mikada H., Watanabe H., Sakashita S. (2002), A method for simultaneous velocity and density inversion and its application to exploration of subsurface structure beneath Izu-Oshima volcano, Japan, *Earth Planets Sp.*, 54, 803-817, 10.1186/BF03352074.

Parfitt, E. A. and Wilson, L. (1995), Explosive volcanic eruptions - IX. The transition between Hawaiian-style lava fountaining and Strombolian explosive activity, *Geophys. J. Int.*, 121, 226-232.

Patanè, D., Barberi G., De Gori, P., Cocina, O., Zuccarello, L., Garcia-Yeguas, A., Castellano, M., D'Alessandro, A., and Sgroi, T. (2017), The shallow magma chamber of Stromboli Volcano (Italy), *Geophys. Res. Lett.*, 44, 6589-6596, doi:10.1002/2017GL073008.

Patrick, M.R., Harris, A.J.L., Ripepe, M., Dehn, J., Rothery, D., and Calvari, S. (2007), Strombolian

explosive styles and source conditions: insights from thermal (FLIR) video, *Bull. Volcanol*., 69, 769-784.

Richardson, J. P., Waite, G. P., & Palma, J. L. (2014), Varying seismic-acoustic properties of the fluctuating lava lake at Villarrica volcano, Chile, *J. Geophys. Res.,* 119, 5560–5573. https://doi.org/10.1002/2014JB011002.

Ripepe, M. (1996), Evidence for gas influence on volcanic seismic signals recorded at Stromboli, *J. Volcanol. Geotherm. Res.*, 70, 221-233.

Ripepe, M., Rossi, M., and Saccorotti, G. (1993), Image processing of explosive activity at Stromboli, *J. Volcanol. Geotherm. Res.*, 54, 335-351.

Ripepe, M., Ciliberto, S., and Della Schiava, M. (2001), Time constraints for modeling source dynamics of volcanic explosions at Stromboli, *J. Geophys. Res*., 106, 8713-8727.

Ripepe, M., Marchetti, E., Poggi, P., Harris, A.J.L., Fiaschi, A., and Ulivieri, G. (2004), Seismic, acoustic, and thermal network monitors the 2003 eruption of Stromboli Volcano. *Eos*, 85, 329-336.

Ripepe, M., Delle Donne, D.,Harris, A., Marchetti, E., and Ulivieri, G. (2008), Dynamics of Strombolian activity, in The Stromboli Volcano: An Integrated Study of the 2002–2003 Eruption, *Geophys. Monogr. Ser.*, vol. 182, edited by S. Calvari et al., pp. 39-48, AGU, Washington, D. C.

Ripepe, M., Delle Donne, D., Genco, R., Maggio, G., Pistolesi, M., Marchetti, E., Lacanna, G., Ulivieri, G., and Poggi, P. (2015), Volcano seismicity and ground deformation unveil the gravity-driven magma discharge dynamics of a volcanic eruption, *Nat. Commun.*, 6:6998, doi:10.1038/ncomms7998.

Rowe, C.A., Aster, R.C., Kyle, P.R., Schlue, J.R., Dibble, R.R. (1998), Broadband recording of Strombolian explosions and associated very-long-period seismic signals on Mount Erebus volcano, Ross Island, Antarctica, *Geophys. Res. Lett.*, 25, 2297-2300.

Seyfried, R., and Freundt, A. (2000), Experiments on conduit flow and eruption behavior of basaltic volcanic eruptions, *J. Geophys. Res.*, 105, 23,727-23,740.

Snieder, R., and Safak, E. (2006), Extracting the building response using seismic interferometry: Theory and application to the Millikan library in Pasadena, California, *Bull. Seism. Soc. Am.*, 96, 586-598.

Stein, S., and Wysession, M. (2003), Introduction to Seismology, Earthquakes, & Earth Structure, *Blackwell Sci.*, 498.

Stoddard, P.R., and Woods, M.T. (1990), Master event relocation of Gorda Block earthquakes:

Implications for deformation, *Geophys. Res. Lett.*, 17(7), 961-964, doi:10.1029/GL017i007p00961.

Sugimura, S., Nishimura, T., Aoyama, H., Yamada, T., Fujita, E., Kawaguchi, R., and Miwa, T. (2015), Relative hypocenter determination of eruption earthquakes using deconvolution: Application to Stromboli volcano, *Japan Geoscience Union Meeting 2015*.

Taisne, B., Brenguier, F., Shapiro, N.M., and V. Ferrazzini (2011), Imaging the dynamics of magma propagation using radiated seismic intensity, *Geophys. Res. Lett*., 38, L04304, doi:10.1029/2010GL046068.

Takei, Y., and Kumazawa, M. (1994), Why have the single force and torque been excluded from seismic source models?, *Geophys. J. Int.*, 118, 20-30.

Tameguri, T., Iguchi, M., and Ishihara, K. (2002), Mechanism of explosive eruption from moment tensor analysis of explosion earthquakes at Sakurajima Volcano, Japan., *Bull. Volcanol. Soc. Jpn*., 49, 197-215.

Trovato, C., Lokmer, I., De Martin, F., and Aochi, H. (2016), Long period (LP) events on Mt Etna volcano (Italy): the influence of velocity structures on moment tensor inversion, *Geophys. J. Int.*, 207, 785-810, doi: 10.1093/gji/ggw285.

Turcotte, D. L. and Schubert, G. (2001), *Geodynamics Second Edition*, 456, Cambridge University Press, Cambridge.

Valade et al. (2016), Tracking dynamics of magma migration in open-conduit systems, *Bull. Volcanol.*, 78, 78.

Vergniolle, S. (1998), Modeling two-phase flow in a volcano, in *13th Australasian Fluid Mechanics Conference*.

Vergniolle, S. and Jaupart, C. (1986), Separated two-phase flow and basaltic eruptions, *J. Geophys. Res.*, 91, 12842-12860.

Vergniolle, S. and Jaupart, C. (1990), Dynamics of degassing at Kilauea volcano, Hawaii, *J. Geophys. Res.*, 95, 2793-2809.

Vergniolle, S., and Brandeis, G. (1996), Strombolian explosions: 1. A large bubble breaking at the surface of a lava column as a source of sound, *J. Geophys. Res.*, 101, 20433-20447, https://doi.org/10.1029/96jb01178.

Vergniolle, S., Boichu, M., and Caplan-Auerbach, J. (2004), Acoustic measurements of the 1999 basaltic eruption of Shishaldin Volcano, Alaska 1. origin of Strombolian activity, *J. Volcanol. Geotherm. Res.*, 137, 109-134.

Waite, G.P., Chouet, B.A., and Dawson, P.B. (2008), Eruption dynamics at Mount St. Helens imaged from broadband seismic waveforms: interaction of the shallow magmatic and hydrothermal systems, *J. Geophys. Res*., 113, B02305. http://dx.doi.org/10.1029/2007JB005259.

Yamada T, Aoyama, H., Nishimura, T., Yakiwara, H., Nakamichi, H., Oikawa, J., Iguchi, M., Hendrasto, M., and Suparmang, Y. (2016), Initial phases of explosion earthquakes accompanying Vulcanian eruptions at Lokon-Empung volcano, Indonesia, *J. Volcanol. Geotherm. Res.*, 327, 310-321, https://doi.org/10.1016/j.jvolgeores.2016.08.011

Zobin, V., (2012), 2nd edition. Introduction to Volcanic Seismology, Elsevier.

Zobin, V. M., Reyes, G.A., Guevara, E. and Bretón, M. (2009), Scaling relationship for Vulcanian explosions derived from broadband seismic signals. *J. Geophys. Res.*, 114, B03203, doi: 10.1029/2008JB005983

Zobin, V. M., Arámbula, R., Bretón, M., Reyes, G., Plascencia, I., Navarro, C., Téllez, A., Campos, A., González, M., León, Z., Martínez, A., and Ramírez, C. (2015), Dynamics of the January 2013–June 2014 explosive-effusive episode in the eruption of Volcán de Colima, México: insights from seismic and video monitoring, *Bull. Volcanol.*, 77, 31.

Zollo, A., De Matteis, R., Capuano, P., Ferulano, F., and Iannaccone, G. (1995), Constraints on the shallow crustal model of the Northern Apennines (Italy) from the analysis of microearthquake seismic records, *Geophys. J. Int.*, 120, 646-662.